

Geometrically constrained statistical systems on regular and random lattices: From folding to meanders

P. Di Francesco¹, E. Guitten²

Service de Physique Theorique, CEA / D SM / SP hT

Unité de recherche associée au CNRS

CEA / Saclay

91191 Gif sur Yvette Cedex, France

We review a number of recent advances in the study of two-dimensional statistical models with strong geometrical constraints. These include folding problems of regular and random lattices as well as the famous meander problem of enumerating the topologically inequivalent configurations of a meandering road crossing a straight river through a given number of bridges. All these problems turn out to have reformulations in terms of fully packed loop models allowing for a unified Coulomb gas description of their statistical properties. A number of exact results and physically motivated conjectures are presented in detail, including the remarkable meander configuration exponent $= (29 + \sqrt{145})/12$.

05/05

¹ philippe@spht.saclay.cea.fr

² guitten@spht.saclay.cea.fr

INTRODUCTION	3
PART A : FOLDING OF REGULAR LATTICES	
1. Phantom folding problems	5
1.1. Folding: some trivial examples	6
1.2. Compactly foldable 2D lattices	12
2. Folding of the triangular lattice	13
2.1. Generalities	13
2.2. Folding of the triangular lattice in $d = 2$: an 11-vertex model	15
2.3. Discrete folding of the triangular lattice in $d = 3$: a 96-vertex model	20
PART B : LOOP MODELS ON REGULAR LATTICES	
3. Loop gas and height model reformulations of the triangular lattice folding	28
3.1. Fully packed loop gas formulations of the 2d folding	28
3.2. Fully packed loop gas formulations of the 3d folding	30
3.3. Height models	31
4. Exact solutions via Bethe Ansatz: the example of the FPL (1) model	33
4.1. FPL (1) and rhombus tiling of the plane	34
4.2. Transfer matrix and eigenvalue equations	35
4.3. Bethe Ansatz	37
4.4. Continuum limit: largest eigenvalue	38
4.5. Thermodynamic entropy and central charge	39
5. Effective field theory description via Coulomb gas	40
5.1. Two-component Coulomb gas for FPL (2)	40
5.2. General FPL (n) and O (n) cases	44
PART C : LOOP MODELS ON RANDOM LATTICES	
6. Folding of random lattices	47
6.1. Foldability of triangulations	47
6.2. Enumeration of foldable triangulations	49
7. Statistical models coupled to 2D Quantum Gravity	55
8. One-avor fully packed loops	57
8.1. Fully packed loops on random trivalent graphs	57
8.2. Fully packed loops on random trivalent bipartite graphs	60
PART D : MEANDERS	
9. 1D self-avoiding folding: Meanders	66
9.1. The meander problem	66

9.2. Meanders as a 1D self-avoiding folding problem	67
9.3. A brief history of meanders	68
10. Solvable cases	69
10.1. Generalization: multi-circuit meanders	69
10.2. Combinatorial solutions at $q = 1, 1$ and -1 : exact enumeration via arch statistics	71
10.3. Multi-river, multi-circuit meanders: asymptotic enumeration via matrix models	73
10.4. Meander determinant	75
11. Two-avor fully packed loops: exponents of the meander problem	78
11.1. Generalized meanders as random lattice loop models	78
11.2. The FPL^2 model on the square lattice	79
11.3. Coupling $FPL^2(n_1; n_2)$ to gravity: Effective field theory of meanders	83
11.4. More meander exponents	85
11.5. Multi-circuit meander exponents	87
12. Numerical checks	88
12.1. Arch growth algorithm	88
12.2. Transfer matrix algorithm	91
12.3. Numerical results	92
13. Meanders as folding of random quadrangulations	96
CONCLUSION	103

INTRODUCTION

The physics of folding encompasses a wide variety of topics ranging from biology to pure mathematics. Folding problems arise for instance in the study of protein conformations [1] and in the physical modelling of biological or artificial membranes [2]. In a different context, the physics of paper folding also displays interesting phenomena, in connection with the mechanical and statistical properties of thin elastic plates or membranes [3]. At a more abstract level, the very description of the folding degrees of freedom of a surface gives rise to very interesting statistical models and quite involved combinatorial problems.

In this wide subject, we choose to concentrate on this last type of questions by focusing on statistical models of discrete lattice folding and emphasizing the crucial role played by geometrical constraints on the statistics of large folded objects. More precisely, we will consider discrete models of "solid" or "fluid" membranes in the form of folding problems for respectively fixed and random lattices. An example of fixed lattice is a piece of the two-dimensional triangular lattice, viewed as a regular collection of rigid equilateral triangles whose edges may serve as hinges between neighboring triangles. An example of random lattice is a triangulation made of the same triangles arranged into a possibly irregular and fluctuating surface tessellation, allowing for curvature defects (more or less than 6 triangles around a node) or topological defects (tessellations of a surface with handles).

Our first task will be to characterize the folding degrees of freedom in these models. This happens to be an extremely difficult problem in the presence of self-avoidance. For this reason, we shall first consider the much simpler "phantom" folding problem in which the membrane is allowed to interpenetrate itself. A first description uses local normal vectors as effective spin variables subject to various geometrical constraints. Although local, these constraints induce a non-local behavior with propagating creases, resulting in a rich phase diagram even for regular lattices.

A second and more powerful description uses loop configurations on the lattice and allows to view folding as a particular instance of the more general problem of the "fully packed" loop gas, that is a set of non-intersecting loops visiting all nodes of the lattice. This approach, combined with field-theoretical techniques, allows for a number of predictions on the statistics of large folded lattices. For regular lattices, these predictions rely either on exact solutions via Bethe Ansatz (integrable case) or on effective field-theoretical descriptions via Coulomb gas.

In the case of random lattices, the loop gas interpretation leads in particular to precise predictions for various configurational exponents characterizing the asymptotics of the number of allowed folding or loop configurations. These predictions make extensive use of interpretations of the folding configurations in terms of discrete two-dimensional quantum gravity, namely statistical models defined on dynamical tessellations of surfaces. At large scales, these models are described by conformal field theories coupled to two-dimensional quantum gravity, and the configuration exponents are obtained from a proper identification of the central charge of the conformal field theory at hand. Alternatively, the discrete models of folding may be represented via diagrammatic expansions of matrix integrals, allowing for a number of direct computations.

Returning to the crucial question of self-avoidance, we will concentrate on the one-dimensional self-avoiding folding problem, also known as the "stamp folding problem". This problem happens to be equivalent to a famous combinatorial problem, the meander problem which may be stated as follows: "enumerate all topologically inequivalent configurations of a non-intersecting circuit crossing a straight river through a given number of bridges". Remarkably, in its meander formulation, the one-dimensional self-avoiding folding problem is described by a two-dimensional gas of fully packed loops on a random lattice, hence belongs to the class of two-dimensional phantom foldings of random lattices. A remarkable outcome of our study is the predicted value for the meander configuration exponent

$$= (29 + \frac{p}{145}) = 12 \quad (1)$$

which governs the large n asymptotics of the number of meanders with $2n$ bridges / $R^{2n} = n$.

This review is based mainly on a series of articles by the authors [4-17]. Other reviews may be found in [18-20].

PART A : FOLDING OF REGULAR LATTICES

This part is devoted to the study of regular lattice folding in the absence of self-avoidance (phantom folding). Such foldings were considered for instance as discrete models for polymers (1D) or for "tethered" membranes (2D), equipped with an underlying regular elastic skeleton, such as crystalline or polymerized membranes [21–24]. Our task is to first identify the folding degrees of freedom and to finally derive explicit statistical properties of large folded objects in the presence of bending rigidity.

1. Phantom folding problems

In all generality, we may define the phantom folding of a D -dimensional lattice in a d -dimensional target space with $d \geq D$ as follows. Viewing the lattice as a simplicial complex with nodes, links, faces, ... D -cells, a folding is a map from the lattice to \mathbb{R}^d such that its restriction to each D -cell is an isometry, i.e. preserves the distance between any pair of points within the cell. The shapes of the D -cells are therefore preserved in a folding, but the relative position of two adjacent D -cells of the lattice may change as long as they remain adjacent to ensure a unique position of their common $(D-1)$ -cell. In other words, the $(D-1)$ -cell serves as a "hinge" between them. Such a folding is phantom in the sense that we allow cells to interpenetrate one-another, as well as distinct points of the lattice to occupy the same target position. A phantom folding is therefore defined by the corresponding folded configuration, without reference to an actual folding process which would continuously deform the original lattice. All the foldings considered in parts A–C below will be phantom. Moreover, we will restrict ourselves to the cases $D = 1$, d arbitrary or $D = 2$ and $d = 2$ or 3 . We are mainly interested in the statistical properties of folded configurations of large portions of lattices for various ensembles corresponding to possibly restricted target spaces within \mathbb{R}^d . For instance, we may consider continuous foldings in which folding "angles" between adjacent D -cells vary continuously with specific distributions, or discrete foldings in which these angles only take finitely many values. For a good choice of these discrete angles, this simply corresponds to discretizing the target space into a d -dimensional lattice.

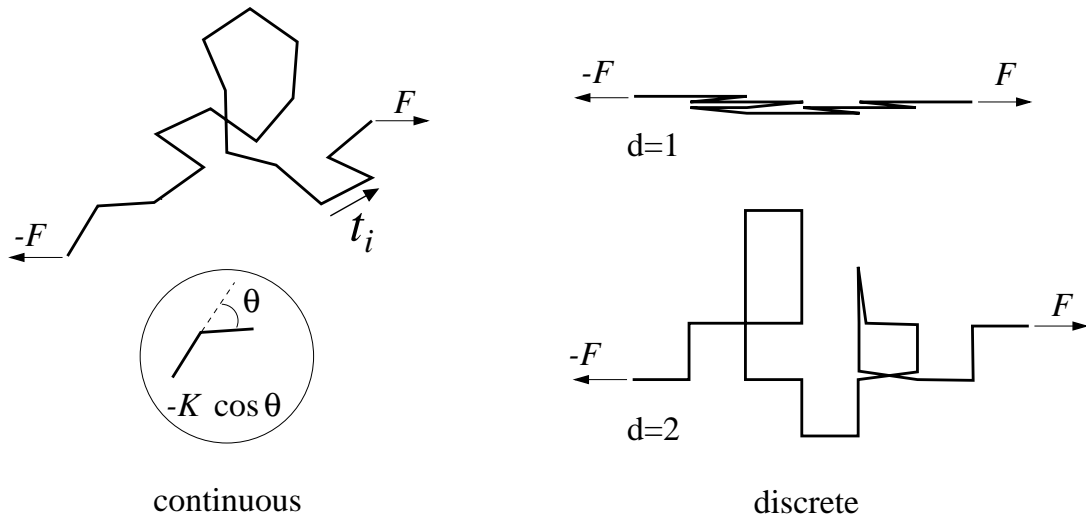


Fig.1: Folding of a segment of 1D lattice in either continuous or discrete target space. The associated bending energy takes the form $-K \cos \theta$ for each pair of consecutive links with relative angle θ . An external force F may also be exerted at the ends.

1.1. Folding: some trivial examples

In this Section, we review two particularly simple folding problems, namely that of a 1D lattice in any dimension, and that of the 2D square lattice in $d = 2$.

1D folding

As a preliminary exercise, let us study the case $D = 1$ of the phantom folding of a segment of length, say L of the lattice of relative integers \mathbb{Z} . Viewing this segment of lattice as made of a chain of $L + 1$ nodes connected by L oriented links of unit length, a folding in \mathbb{R}^d is entirely characterized, up to a global translation, by the sequence $ft_i g_{1 \leq i \leq L}$ of "tangent" vectors, all of unit length, which are the images of the links after folding, themselves connected into a possibly overlapping chain. We decide to attach to each folded configuration a weight

$$w(ft_i g) = \exp(-E(ft_i g)) \quad (1.1)$$

where the energy of the configuration reads

$$E(ft_i g) = -K \sum_{i=1}^{L-1} t_i \cdot t_{i+1} - F \sum_{i=1}^L t_i \quad (1.2)$$

corresponding to a "bending" energy with bending rigidity K and an external force F between the extremities of the chain. We may consider several statistical ensembles for the t_i 's. Natural choices are (see Fig.1):

- (a) A continuum equidistributed set of unit vectors t_i in \mathbb{R}^d .
- (b) A discrete equidistributed set with $t_i \in \{e_1; e_2; \dots; e_d\}$ where e_i is the canonical basis of \mathbb{R}^d . This choice alternatively amounts to requiring that the nodes of the chain have their folded images on that of a d -dimensional hypercubic lattice.

Let us start with $d = 1$, in which case only the discrete ensemble (b) above makes sense. The model with tangent vectors $t_i = \pm 1$ and weights (1.1) (1.2) is nothing but the 1D Ising model with spin coupling K and magnetic field F . The partition function on a segment of length L and with free boundary conditions reads:

$$Z_L(K; F) = \cosh F + \frac{e^{-K} + e^K \sinh^2(F)}{(e^K \cosh(F) + 1)^{L-1}} + \cosh F \frac{e^{-K} + e^K \sinh^2(F)}{(e^K \cosh(F) - 1)^{L-1}} \quad (1.3)$$

with $\langle t_i \rangle = \frac{1}{Z_L} \frac{\partial}{\partial F} \log Z_L(K; F)$. We may define the order parameter M as the average orientation of the links through $M = (1/L) \sum_{i=1}^L t_i$, which is nothing but the magnetization in the Ising language, with expectation value $M = \langle t_i \rangle = (1/L) \partial_F \log Z_L(K; F)$. For large L and small F , we easily get

$$M \approx e^{2K} F \quad (1.4)$$

In particular, we recover the well known (1D Ising) result that there is no spontaneous orientation, i.e. $M = 0$ for $F \rightarrow 0$ for all finite values of K , expressing that the chain is always "crumpled" in the absence of external force. Still a "attening" transition occurs at $K = +1$ at which $M = \text{sign}(F) = \pm 1$ for $F \rightarrow 0$, corresponding to a fully extended chain.

This result is qualitatively the same for all target dimensions d . For instance, if the target space is the d -dimensional hypercubic lattice (case (b) above), we get an average orientation M in the direction of the force F with expectation value:

$$M = \frac{d}{d(d+1)} \frac{1 + e^K}{1 + e^{-K}} F \quad (1.5)$$

for small F , which displays the same attening transition at $K = +1$.

Similarly, in the continuous case (a) above, we get

$$M = \frac{1 + g(K)}{d(1 - g(K))} F \quad (1:6)$$

where $g(K) = \partial_K \text{Log}(\int^R d^d t \exp(K t \cdot e))$ for any fixed unit vector e . For instance, when $d = 3$, we have $g(K) = \coth(K) \cdot 1 = K$. As $g(K)$ tends to 1 only at $K = +1$, we find again a softening transition at $K = +1$.

Folding of the square lattice in $d = 2$

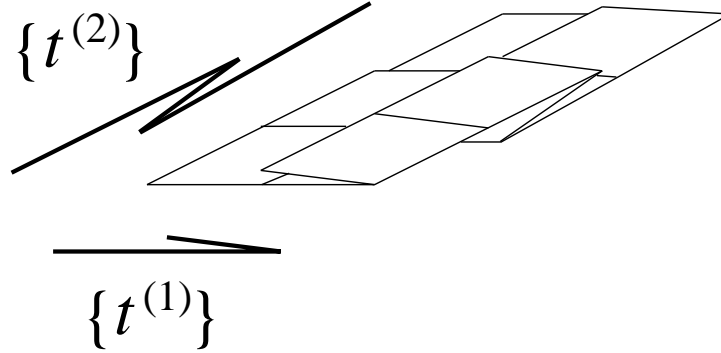


Fig 2: The 2d phantom folding of a piece of square lattice factorizes into the two 1D foldings of its south and west boundaries.

Another particularly simple example is that of phantom folding of a rectangular piece, say of size $L_1 \times L_2$ of the 2D square lattice into a plane target. The image of each square cell is a unit square in the plane, entirely specified by the data of the two unit and orthogonal "tangent" vectors $t^{(1)}$ and $t^{(2)}$, images of the south and west boundary links of the cell, pointing from their common origin (SW node). It is easily seen that preserving the shape and connectivity of the square cells implies that, up to a global rotation, $t^{(1)}$ may take only the two values, say e_1 while $t^{(2)} = e_2$, and that moreover the value of $t^{(1)}$ (resp. $t^{(2)}$) is the same for all south (horizontal) oriented links in a column (resp. all west-vertical-oriented links in a row). In other words, the folding constraints impose that the creases must propagate along straight lines all the way across the lattice. Each folded state is therefore entirely determined by the south (resp. west) 1D tangent vectors along the southern (resp. western) border of the $L_1 \times L_2$ rectangle, namely by two independent sets of Ising spins $ft_i^{(1)} g_{1 \leq i \leq L_1}$ and $ft_j^{(2)} g_{1 \leq j \leq L_2}$ (see Fig 2). In particular, the total number of folded states is $2^{L_1 + L_2}$, leading to a thermodynamic entropy per square

of $s = \lim_{L_1, L_2 \rightarrow \infty} \frac{1}{L_1 L_2} \log(2^{L_1 + L_2}) = 0$. The above factorization also allows to write the bending energy of the entire rectangle in terms of the spins as

$$E_b = \sum_{i=1}^{L_1-1} K_{L_2} t_i^{(1)} t_{i+1}^{(1)} + \sum_{j=1}^{L_2-1} K_{L_1} t_j^{(2)} t_{j+1}^{(2)} \quad (1:7)$$

As in the 1D case, we may also introduce a symmetry breaking field F coupled to the "orientation" of the folded state. For all 2D folding problems and for $d = 2$ or 3 , it is convenient to couple F to the projected area on a given plane of the target space³. For $d = 2$, this amounts to adding an energy

$$E_p = F \sum_{i=1}^{X^1} \sum_{j=1}^{X^2} t_i^{(1)} t_j^{(2)} = F S_1 S_2 \quad (1:8)$$

where $S_a = \sum_{i=1}^{L_a} t_i^{(a)}$ is the total (algebraic) projected length in the direction a . The partition function may be written as

$$Z_{L_1, L_2}(K; F) = \sum_{\substack{S_1 = \sum_{i=1}^{L_1} t_i^{(1)} \\ S_1 = L_1 \bmod 2}} \sum_{\substack{S_2 = \sum_{j=1}^{L_2} t_j^{(2)} \\ S_2 = L_2 \bmod 2}} e^{F S_1 S_2} \hat{Z}_{L_1}(K_{L_2}; S_1) \hat{Z}_{L_2}(K_{L_1}; S_2) \quad (1:9)$$

where $\hat{Z}_L(K; S)$ is the coefficient of $e^{F S}$ in $Z_L(K; F)$ as given by Eq.(1.3), corresponding to the contribution of total projected length S to the 1D partition function. In the thermodynamic limit, it is convenient to introduce the free energy per square at fixed projected lengths $S_a = \rho_a L_a$

$$f(\rho_1; \rho_2) = \lim_{L_1, L_2 \rightarrow \infty} \frac{1}{L_1 L_2} \log [e^{F L_1 L_2 \rho_1 \rho_2} \hat{Z}_{L_1}(K_{L_2}; \rho_1 L_1) \hat{Z}_{L_2}(K_{L_1}; \rho_2 L_2)] \quad (1:10)$$

as well as the total free energy per square

$$f = \lim_{L_1, L_2 \rightarrow \infty} \frac{1}{L_1 L_2} \log [Z_{L_1, L_2}(K; F)] = \min_{\rho_1, \rho_2 \in [0, 1]} f(\rho_1; \rho_2) \quad (1:11)$$

For large L_1 and L_2 , the effective couplings K_{L_1} and K_{L_2} in (1.9) tend to infinity. For positive K , $\hat{Z}_{L_1}(K_{L_2}; S_1 = \rho_1 L_1)$ is then dominated by two (symmetric) configurations

³ Note that for a 1D chain, the coupling to the "projected length" on a given line is equivalent to a force exerted at the ends of the chain in the direction of this line.

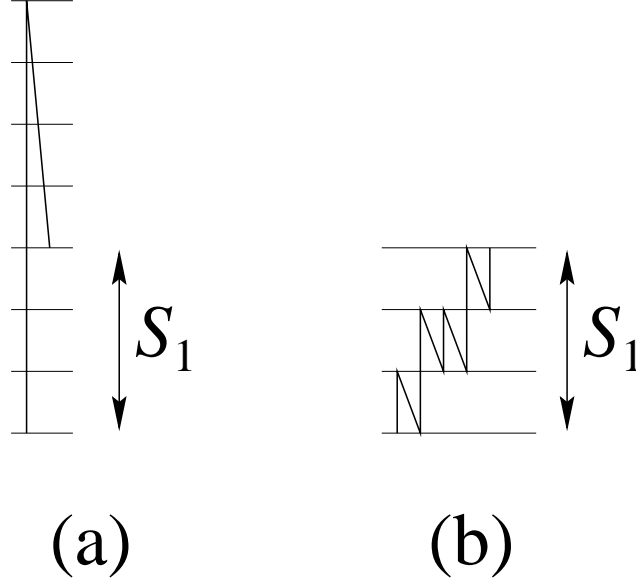


Fig.3: A typical configuration (a) minimizing or (b) maximizing the number of folds at fixed projected length S_1 . In case (a), the number of folds is at most one while in case (b), it is given by $L_1 - \lfloor S_1 \rfloor - S_1; 0$.

with at most one fold in the direction 1 (see Fig.3), hence, in the thermodynamic limit, we have

$$f(\alpha_1; \alpha_2) = -2K - F \alpha_1 \alpha_2 \quad (1.12)$$

The minimum of this free energy is attained at $\alpha_1 = \alpha_2 = \text{sign}(F)$ expressing the completeness of the lattice in the thermodynamic limit for any F . The corresponding total free energy reads

$$f = -2K - F \alpha_1 \alpha_2 \quad (1.13)$$

For negative K , $\hat{Z}_{L_1}(K, L_2; S_1)$ is dominated by the configurations which maximize the number of folds in the direction 1 (see Fig.3), hence with exactly $L_1 - \lfloor S_1 \rfloor - S_1; 0$ such folds, contributing by an energy $K(L_1 - 2\lfloor S_1 \rfloor)$ and by an entropy 0 in the thermodynamic limit (the number of these configurations is clearly bounded by 2^{L_1}). This leads to a free energy

$$f(\alpha_1; \alpha_2) = 2K(L_1 - \lfloor S_1 \rfloor - \alpha_1 \alpha_2) - F \alpha_1 \alpha_2 \quad (1.14)$$

The minimum of this free energy is now attained at $\alpha_1 = \alpha_2 = 0$ for $F \alpha_1 \alpha_2 < 4K$, and at $\alpha_1 = \alpha_2 = \text{sign}(F)$ otherwise, leading to

$$f = \min(-2K - F \alpha_1 \alpha_2, 2K) \quad (1.15)$$

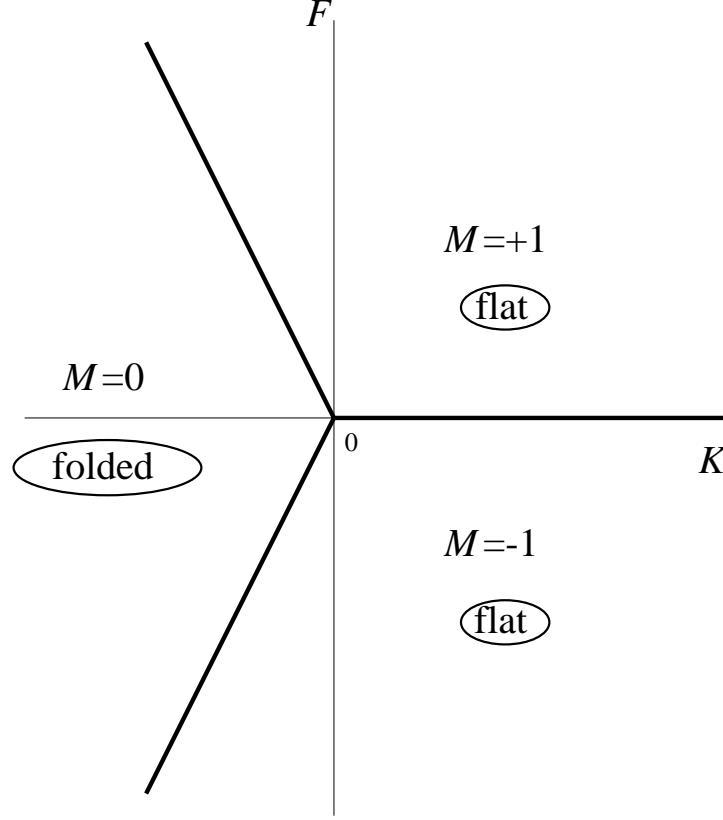
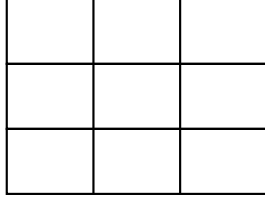


Fig.4: Phase diagram of the phantom folding of the square lattice in 2d, in the plane $(K; F)$ of bending rigidity K and symmetry breaking field F . First order transition lines (thick lines) separate three regions with constant average projected area per square $M = 0, +1$, or -1 . In each of these phases, the lattice is frozen in a unique state, either completely flat ($M = \pm 1$) or completely folded ($M = 0$).

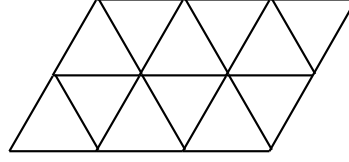
For $K < 0$ and in the thermodynamic limit, the lattice is therefore totally flat for $F > 4K$, and folded for $F < 4K$. More precisely, the folded phase is dominated by a single configuration with maximal number of folds in both directions, i.e. corresponds to the pure state of the completely folded lattice. The transition across the lines $F = 4K$ is first order, as well as that across $F = 0$ for $K > 0$ (see Fig.4). Note that, as opposed to the 1D case, the flattening transition now occurs at $K = 0$.

Although it may seem at first rather pathological, the square lattice planar folding captures a number of essential features of regular lattice folding:

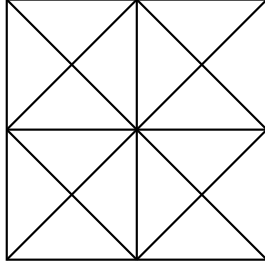
- the non-local nature of the creases which propagate throughout the lattice;
- the consequent absence of local excitations of the pure flat state;
- the existence of a first order transition separating a completely flat phase made of this single flat state from a crumpled phase.



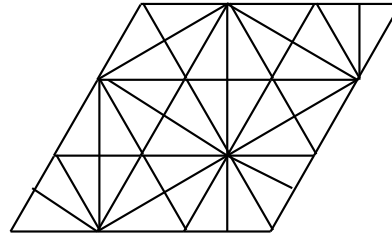
Rectangular



Triangular



Square-Diagonal



Double-Triangular

Fig. 5: The classification of two-dimensional compactly foldable lattices.

1.2. Compactly foldable 2D lattices

The details of folding are strongly lattice dependent. A good criterion for choosing the lattices to be folded is that they give rise to sufficiently many folded configurations. This is usually a prerequisite for allowing interesting (geometrical) phase transitions. For 2D lattices, a basic requirement is to demand that the lattice might be completely folded onto one of its faces. Such a lattice will be called compactly foldable. This restricts very strongly the possible lattices: indeed, the corresponding lattice must have only one type of face, together with its finitely many possible rotations and reflections. This gives rise to a classification of the two-dimensional compactly foldable lattices: they fall into the four cases depicted in Fig. 5, namely rectangular, triangular, square-diagonal and double-triangular.

The proof of this classification goes as follows [18]. Let us concentrate on a node of the lattice. Each adjacent edge may serve as a hinge in the folding of its two adjacent faces, hence bisects the wedge made by its two neighboring edges around the node. Moreover, as the normal vectors alternate between neighboring faces in the completely folded state, the number of faces adjacent to every node is even, as is the number of edges adjacent to any node. Each node v is therefore the center of a regular star of say $2m_v$ edges forming angles

of $\pi_v, m_v = 2$, hence those angles are either right or acute. The faces are therefore polygons with at most four edges, and they can have four only if they are rectangles. This is the case where all $m_v = 2$, the rectangular lattice. Otherwise, all faces must be triangular, with right or acute angles. Such a face has angles $\pi_1; \pi_2; \pi_3$, with $m_i = 2$, and $\sum \pi_i = 2\pi$. There are only three solutions up to permutation for $(\pi_1; \pi_2; \pi_3)$ namely

$$\begin{aligned} (3;3;3) & ! \quad \text{Triangular} \\ (2;4;4) & ! \quad \text{Square Diagonal} \\ (2;3;6) & ! \quad \text{Double Triangular} \end{aligned} \tag{1.16}$$

This completes the proof.

It is clear that the folding of the rectangular lattice is equivalent to that of the square lattice, in particular its 2d folding is trivial as discussed in the previous Section, with a vanishing thermodynamic entropy of folding. As it turns out, the three other cases share the property of having a non-zero thermodynamic entropy of folding per face [4,25]. In the following Sections, we will concentrate on the case of the triangular lattice, which we will fold both in $d = 2$ and 3.

2. Folding of the triangular lattice

2.1. Generalities

In this Section, we address the question of the folding of the triangular lattice. This is the simplest non trivial example of regular lattice folding and it captures all the generic properties of compactly foldable lattices. Another advantage of this model is that it bears links to some exactly solvable integrable model. Very generally, a folded configuration of the triangle lattice will consist in keeping the triangles equilateral of unit side, while the edges serve as hinges between neighboring triangles which may a priori form arbitrary angles.

In the following, we will study two particular examples of folding:

- (a) The planar folding, i.e the case $d = 2$.
- (b) The folding on the Face Centered Cubic (FCC) lattice corresponding to $d = 3$ and suitably defined folding angles.

The foldings of the triangular lattice may be characterized equivalently by link variables, corresponding to tangent vectors, or face variables, corresponding to normal vectors.

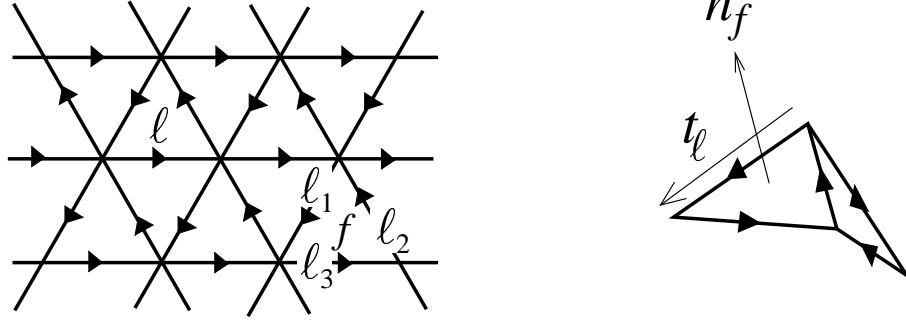


Fig.6: Orientation of the links of the triangular lattice. The link (t_l) and face (n_f) variables.

Link variables

We first start by orienting all the links of the triangular lattice in a coherent way so that all triangles pointing up are oriented counterclockwise and all triangles pointing down are oriented clockwise (see Fig.6). To each oriented link l , we associate its image t_l in the folded configuration. To ensure that any elementary triangle has for its image an equilateral triangle of side 1 in \mathbb{R}^d , it is sufficient to require that all t_l 's are unit vectors, and that moreover

$$t_{l_1} + t_{l_2} + t_{l_3} = 0 \quad (2.1)$$

for the three oriented links l_1 , l_2 and l_3 around each triangle.

Face variables

We can also describe a folding by face variables by considering the normal vector to any triangle f . For $d = 3$, it reads

$$n_f = \frac{2}{3} t_{l_1} \wedge t_{l_2} \quad (2.2)$$

where l_1 and l_2 are two consecutive oriented links around f and with $\epsilon = +1$ (resp. -1) for triangles pointing up (resp. down) on the lattice.

It is natural to think of this normal vector as a spin variable. The introduction of a bending energy amounts to a spin-like coupling K between normals of neighboring faces. As we shall see in the following, such energy is responsible for various conformational transitions.

As for link variables, the face variables are not independent on each triangle. The six normal vectors for the six triangles around a node are correlated via a vertex-constraint. A more precise formulation of this constraint will be given in the case (a) of the planar folding, where it leads to an "11-vertex model", and in the case (b) of the folding on the FCC lattice, where it leads to a "96-vertex model".

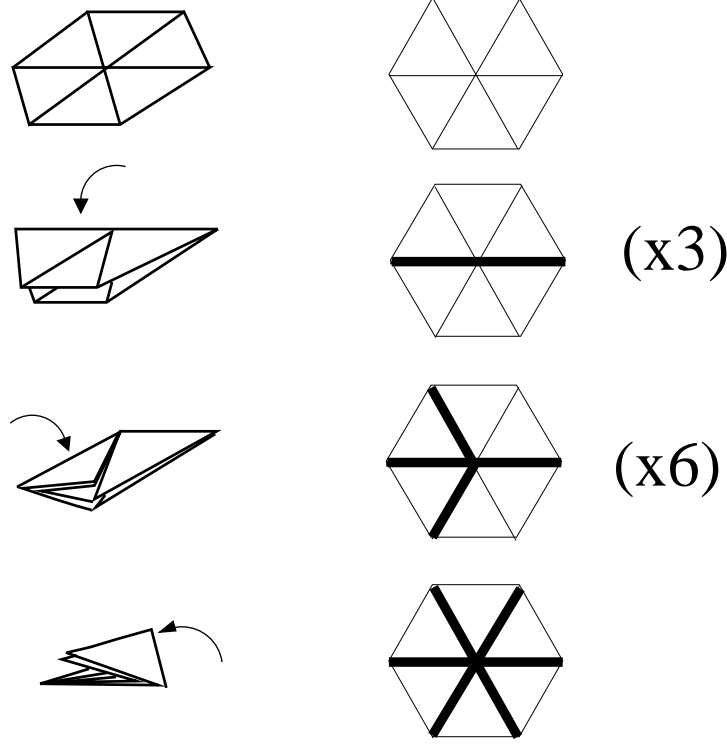


Fig.7: The 11 possible folding environments of an elementary hexagon, corresponding (from top to bottom) to : no fold, 1 fold (3 configurations), 2 folds (6 configurations) or 3 folds. The pictorial representation on the left is only intended as a guide for the reader and only the final (phantom) folded state is relevant. The folds are indicated on the right by thick lines.

2.2. Folding of the triangular lattice in $d = 2$: an 11-vertex model

The simplest case of folding, first introduced by Kantor and Jaric [26], corresponds to the planar folding, i.e. the folding in the plane \mathbb{R}^2 . In this case, the angle between two neighboring triangles⁴ is either 0 (no fold), or 180 (complete fold). Folding an elementary hexagon leads to the 11 possible environments represented in Fig.7. We recall that our definition of phantom folding is limited to the image of the lattice and does not distinguish between the different ways of reaching the same configuration. One can easily convince oneself that all folding constraints reduce to those of Fig.7 around each elementary hexagon. This will become clear below in the language of tangent vectors. The problem of planar folding is therefore entirely characterized by the local rules of Fig.7 on elementary hexagons. As such, planar folding is an 11-vertex model.

⁴ We will take here as definition of the angle between two triangles that between their normal vectors.

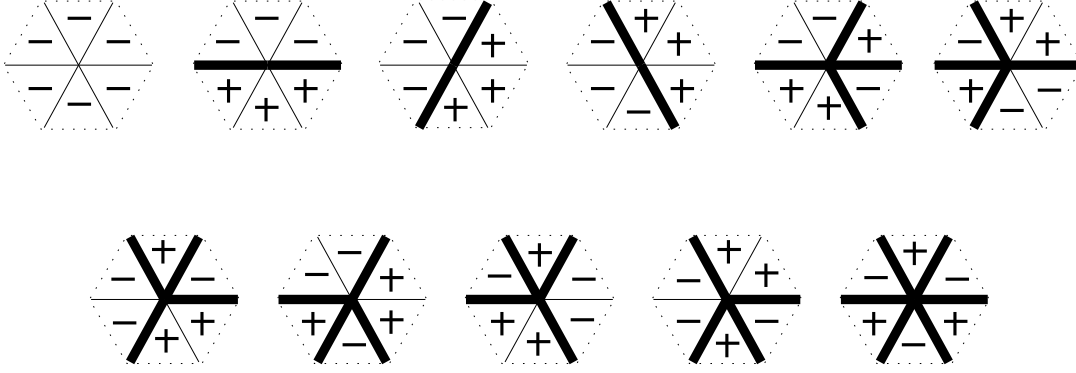


Fig.8: The 11 possible spin environments (up to a global reversing of the spins) around a node. In all cases, the number of +1 (resp. -1) spins is a multiple of 3.

Face variables: constrained Ising spins

The normal vector to each triangle may be described by an Ising spin which may take only two values $s_i = +1$ or $s_i = -1$ according to whether the triangle has been flipped or not in the folding. The folds are nothing but the domain walls for the spin variable. The 11 environments of Fig.7 correspond to the 11 possible environments in terms of spins (up to a global reversal of the spins) indicated in Fig.8. A simple characterization of the allowed spin configurations [4] is that the number of spins $s_i = +1$ must be equal to 0, 3 or 6, i.e. must be a multiple of 3, or equivalently:

$$\sum_{i=1}^6 s_i = 0 \pmod{3} \quad (2:3)$$

for the six spins around each node. One easily checks that the number of such configurations is $\binom{6}{0} + \binom{6}{3} + \binom{6}{6} = 22 = 2 \times 11$ as it should.

Link-variables: the three-color model

A natural question concerns the computation of the folding entropy which characterizes the exponential growth of the number Z_N of possible foldings as a function of the number N of triangles (for a finite sub-lattice of the triangular lattice). One defines the folding entropy s by⁵:

$$s = \lim_{N \rightarrow \infty} \frac{1}{N} \log Z_N = \log q : \quad (2:4)$$

⁵ In this definition, one expects that the actual shape of the sub-lattice should not matter as long as the two dimensions scale in the same way and provided we take free boundary conditions.

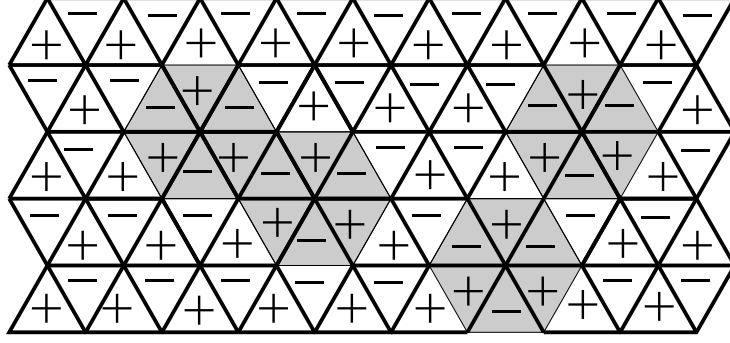


Fig.9: Starting from the completely folded configuration, we may reverse the 6 spins of some elementary hexagons (here in grey) and still get an allowed configuration provided the hexagons do not overlap (hard hexagons).

One can interpret q as the number of degrees of freedom per triangle, with clearly, for constrained Ising spins, $1 \leq q \leq 2$. The existence of a non-vanishing entropy s (i.e. $q > 1$) is not a priori obvious as, like in the square lattice case, there exists no configuration for which the folds are localized. A simple way of seeing this is to cut each configuration of Fig.8 vertically in the middle and to notice that whenever a fold is present on the left half of the hexagon, then a fold is also present on the right side. The folds therefore propagate all the way from and to infinity from the left to the right. In other words, despite the locality of the rules of Fig.7, the flat configuration (without fold) has no local excitation. Numerically, Kantor and Jaric have shown [26] that $q = 1.21$ and that there is therefore a non-vanishing folding entropy, as opposed to the square lattice case. This result may be understood by starting instead from the completely folded state, with a perfect antiferromagnetic order for the spins. We may then reverse globally all the spins of one single elementary hexagon and the configuration remains admissible (see Fig.9). This operation may be repeated for arbitrarily many hexagons as long as they do not overlap. There exist therefore local excitations of the completely folded configuration, leading to a non-vanishing entropy.

The entropy may be computed exactly in the link-variable picture [4]. Starting from a given triangle, the vectors t_i , $i = 1, 2, 3$ around this triangle are three unit vectors in \mathbb{R}^2 with vanishing sum, therefore of the form $t_1 = A$, $t_2 = B - RA$ and $t_3 = C - R^2A = R^{-1}A$ where A is a unit vector and R the rotation of angle 120° (or -120°). One can then easily convince oneself that the vectors t_i for all the links of the lattice may only take these same three values A, B or C , with moreover the constraint that the three "colors" A, B

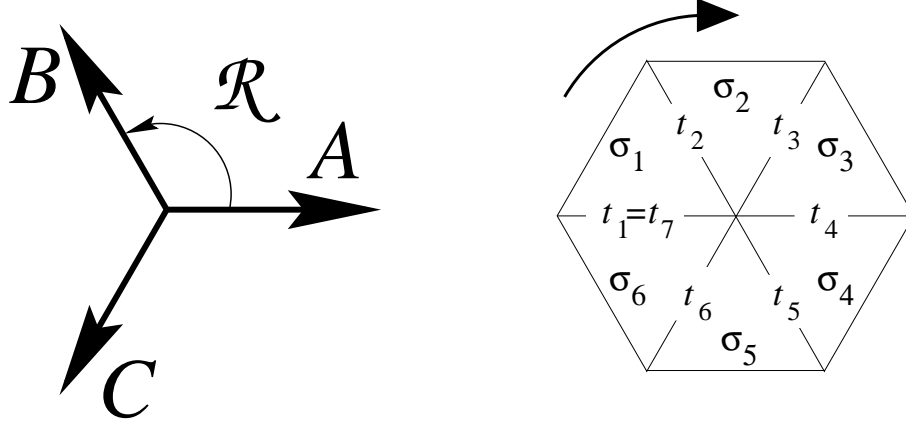


Fig.10: The three allowed values (colors) for t_i are A , $B = R A$ and $C = R^{-1} A$. The relation between link variables t_i and the face variables $\sigma_i = \pm 1$ around a node reads $t_{i+1} = R^{-\sigma_i} t_i$. The link variable is well defined if $t_7 = t_1$, that is if (2.3) is satisfied.

and C must be present once and only once around each triangle [4]. A planar folding of the triangular lattice is therefore equivalent to a tricoloring of the links of the lattice with three colors which must be distinct around each triangle. The color simply represents the orientation of the link in the folded configuration, among three allowed values.

In this language, the spin of a face tells us about the cyclic order of the colors around this face with $\sigma_i = +1$ (resp. $\sigma_i = -1$) if the colors are in the order A, B, C (resp. A, C, B) in counterclockwise direction. In particular (see Fig.10), the variables t_i , $i = 1; \dots; 6$ of the links around a node are related to the spins σ_i by $t_{i+1} = R^{-\sigma_i} t_i$. As $R^3 = 1$, the link variable is well defined after one turn around the node if and only if the relation (2.3) is satisfied. In this language, all folding constraints ensuring that the link variable is well defined along any closed loop clearly reduce to Eq.(2.3) around each elementary hexagon.

In the dual language, a planar folding therefore corresponds to the coloring of the links of the hexagonal lattice with three colors, such that no two adjacent links be of the same color. The entropy of this three-color problem was obtained by Baxter [27], and can therefore be reinterpreted as the planar folding entropy per triangle of the triangular lattice, with the result:

$$q = \lim_{n \rightarrow \infty} \frac{1}{n} \ln \frac{(3n-1)!}{3^n (3n-2)!} = \frac{\ln \frac{(1=3)}{(2=3)}}{2} = \frac{\ln \frac{3}{2}}{2} \quad (1=3)^{3=2} \quad (2.5)$$

Its numerical value $q = 1.208717\dots$ ($s = \text{Log} q = 0.189560\dots$) is in very good agreement with the estimate of Ref.[26].

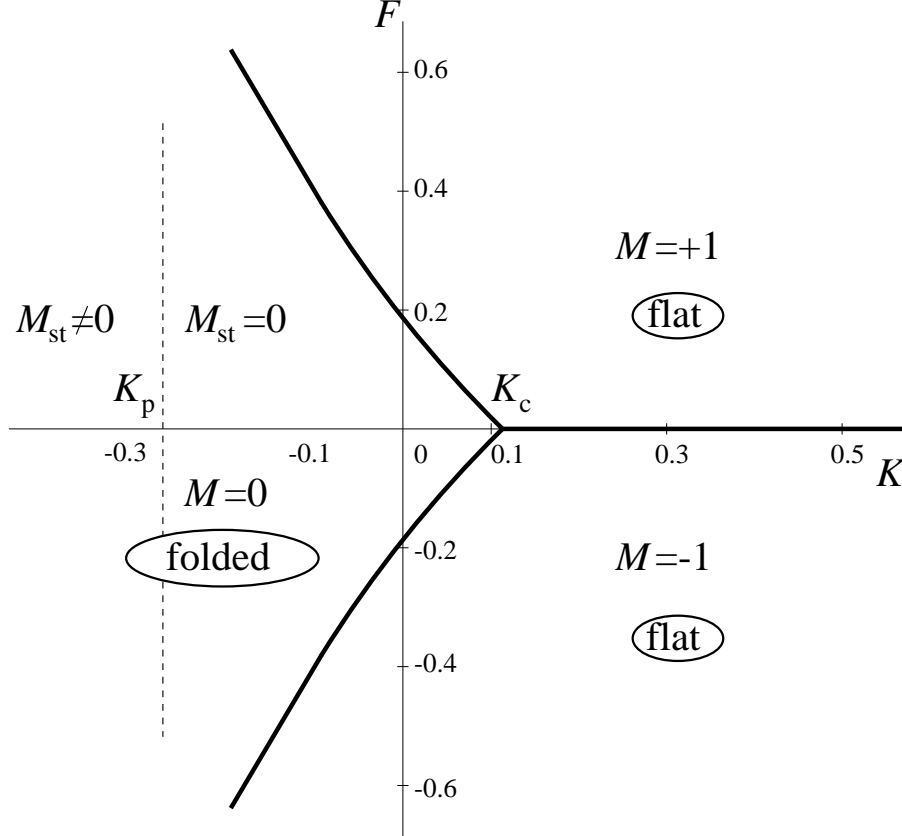


Fig.11: Phase diagram for the planar folding in the presence of a bending energy term $E_b = K \cos(\theta)$ and a symmetry breaking field F . A first order transition at $K_c = 0.1$ separates the crumpled phase where the average projected area $M = 0$ from a flat phase where $M = 1$ (or -1). This latter phase is frozen in the pure state of the completely flat surface. Within the crumpled phase, a continuous piling-up transition now occurs at $K_p = 0.28$ [7,8,28] between a disordered phase with $M_{st} = 0$ and an ordered phase with $M_{st} \neq 0$.

We may finally consider the phase diagram obtained in the presence of a bending energy $E_b = K \cos(\theta)$ per link with folding angle $\theta = 0$ (no fold) or 180° (complete fold). Like in the square lattice case, we also introduce a symmetry breaking field F conjugate to the projected area ($E_p = F$ per face) and which plays the role of a lateral tension applied to the surface. The resulting phase diagram, depicted in Fig.11, was obtained by a transfer matrix approach [5] and later corroborated by a variational study [28].

Comparing this result to that of the square lattice (Fig.4), we note a qualitative resemblance, with three first order transition lines separating regions with $M = 0; \pm 1$. There are however two important differences. Firstly, the phase $M = 0$ is no longer frozen in a single state due to the existence of elementary excitations of the fully folded state.

More precisely, let us introduce the "piling-up" (staggered) order parameter $M_{st} = h(M_M - M_O)/2$ where M_M (resp. M_O) is the average projected area of the triangles pointing up (resp. down) in the original triangular lattice. A continuous piling-up transition now occurs at a negative value $K_p \approx -0.28$ above which the crumpled phase is disordered ($M_{st} = 0$) and below which the lattice tends to be piled-up onto a single triangle ($M_{st} \neq 0$). Note that the transition lines between the crumpled and flat phases are no longer straight lines. Secondly, the triple point where the three transition lines meet is at a positive value $K_c \approx 0.1$. This shows the existence of a first order flattening or crumpling transition between a crumpled phase for $K < K_c$ and a completely flat phase for $K > K_c$ corresponding again to a pure state without any fold, with $M = 1$ (or -1). The existence of such a crumpling transition was also predicted in continuous models of tethered membranes [21-24]. The first order nature of the present transition seems however to be due to the discrete (spin-like) nature of the (normal vector) degrees of freedom. For $K = 0$, comparing the energy per triangle F in the flat state (no entropy) and the entropy $\text{Log} q$ in the folded state (no energy since $M = 0$), we deduce that the transition lines cross the vertical axis at values $F = \text{Log} q \approx 0.189$. The existence of a strictly positive value of the crumpling transition rigidity is therefore directly linked to the existence of a non-zero entropy of folding. In some sense, the critical point $K = 0$ of the square lattice folding has been split into two transition points $K_p < 0 < K_c$ (details may be found in Refs. [7,8,28]).

2.3. Discrete folding of the triangular lattice in $d = 3$: a 96-vertex model

A second simple example of folding of the triangular lattice consists in picking the Face Centered Cubic (FCC) lattice for target space [6]. The latter may be seen as a discretization of \mathbb{R}^3 for which the faces of all the elementary 2-cells are equilateral triangles. More precisely, the FCC lattice may be viewed as a regular piling-up of elementary octahedra, completed by tetrahedra, as indicated in Fig.12.

The folding of the triangular lattice on the FCC lattice authorizes four folding angles: 0° (no fold) 180° (complete fold) 109.28° (acute fold, i.e. on the same tetrahedron) and 70.32° (obtuse fold, i.e. on the same octahedron). The link variables t_i then take their values in a set of 12 allowed values $(e_i - e_j)/\sqrt{2}$ with $1 \leq i < j \leq 3$. These 12 vectors are in one-to-one correspondence with the oriented edges of an elementary octahedron of side 1 (see Fig.13). A simple way to label them is to first color them in three colors A, B, C such that all four vectors in a given plane of the octahedron of Fig.13 be of the same color. We then complete the color by a complementary variable defined as follows: for each vector of

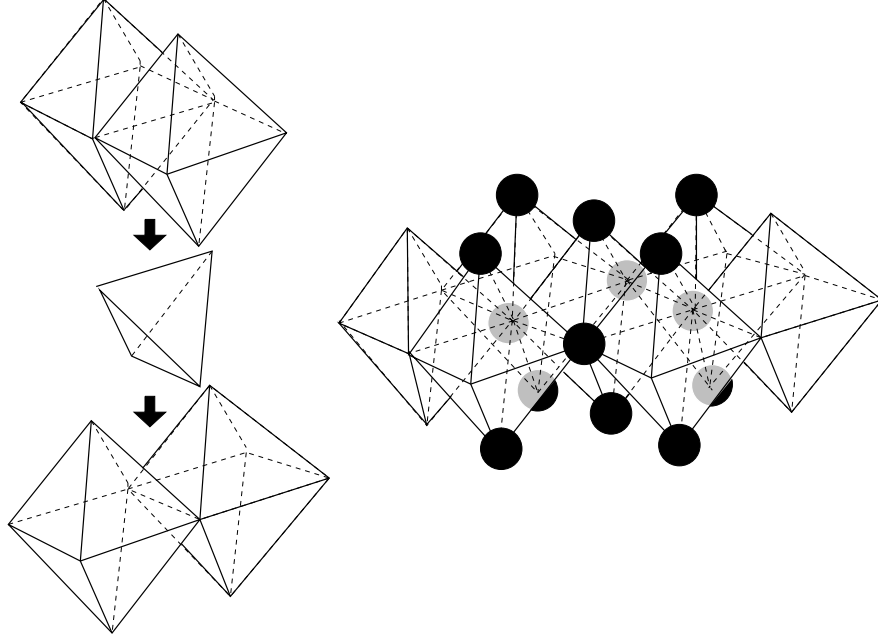


Fig.12: The FCC lattice viewed as a piling-up of octahedra completed by tetrahedra.

color A or B, we define a variable $C = \pm 1$ indicating on which side of the plane of color C on the elementary octahedron this vector lies (see Fig.13). Similarly, we define a variable $B = \pm 1$ for the vectors colored A or C and a variable $A = \pm 1$ for those colored B or C. Each of the 12 unit vectors is entirely specified by its color and the value of the two complementary variables.

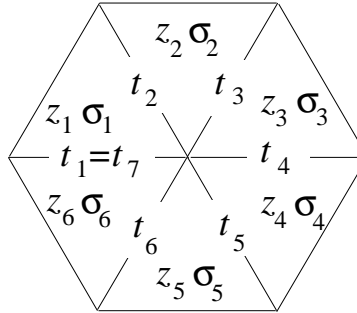


Fig.14: The 6 link variables and the 6 pairs of spins around a node.

The three vectors t_i , $i = 1; 2; 3$ around a given face must have a vanishing sum: they must be chosen among the 8 triplets of unit vectors with vanishing sum (in correspondence with the 8 faces of the octahedron of Fig.13), which, with the $3!$ permutations of the three vectors, leads to 48 possibilities. For each triplet, the three vectors have different colors, and have the same values of A, B and C, i.e. are of the form $(A; B; C); (A; C; B); (B; C; A)$.

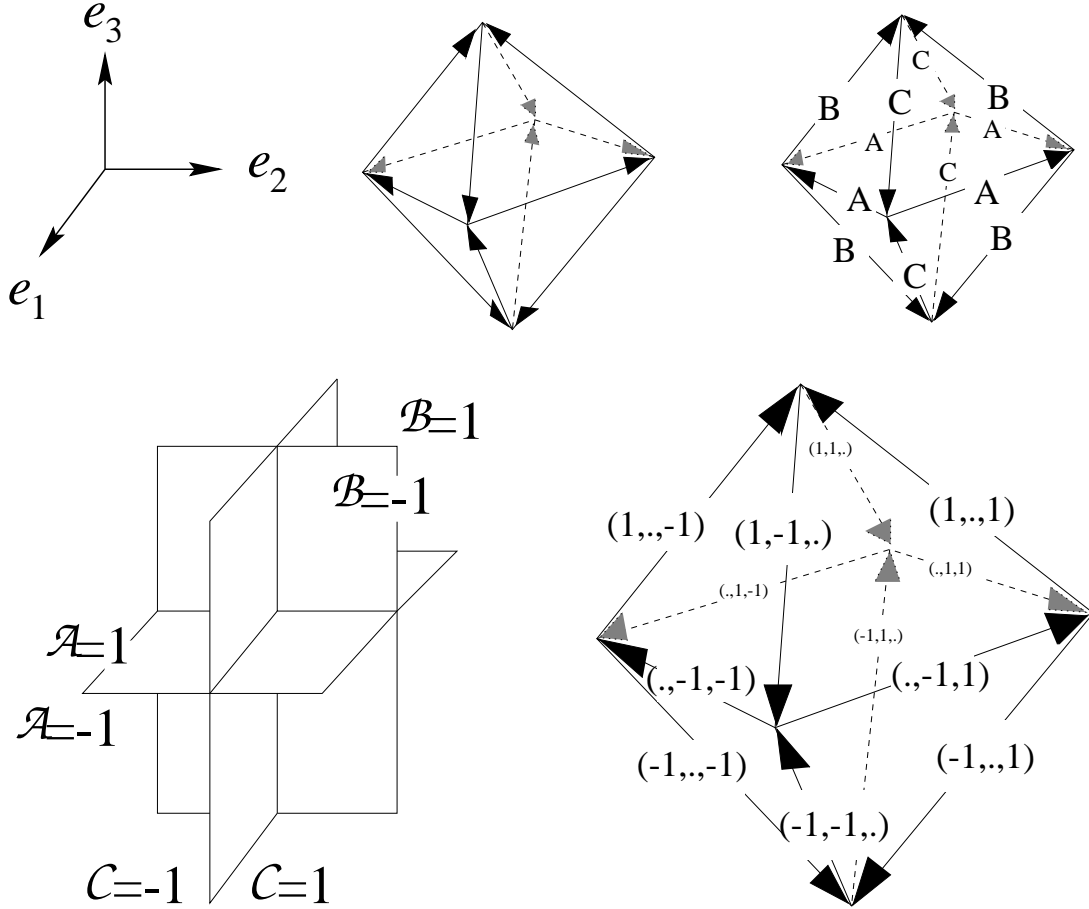


Fig.13: The 12 oriented edges of an elementary octahedron of side 1 provide a set of 12 unit vectors for the allowed link variables of the FCC folding of the triangular lattice. We attach colors A, B, C to these vectors as indicated. We have three color planes, each containing four vectors. We further attach variables A, B and C to each edge. Each vector is coded by a triplet of the form (A; B; C), (A; B; C) or (A; B; C), where the position of the missing variable (coded by a dot) corresponds to the color of the vector at hand. Note that the three vectors around each face share the same A, B, C variables.

We may then follow the 6 link variables t_1 around a node in clockwise direction (see Fig.14). Starting from t_1 which takes one of the 12 allowed values, the vector t_2 may take only $48=12 \times 4$ possible values coded by two face spin variables $s = \pm 1$ and $z = \pm 1$. The variable s indicates the change of color from t_1 to t_2 , with $s = +1$ if the color "increases" in cyclic order ABC and $s = -1$ otherwise. The variable z is simply the product ABC corresponding to the face $ft_1; t_2; t_1 \rightarrow t_2$ on the octahedron of Fig.13.

Going back to the original folding problem, we may now characterize entirely the relative folding state of any two neighboring triangles by the relative values of $(s_1; z_1)$ vs

$(z_1; z_2)$ on these two faces. We have the following correspondence

$z_2=z_1$	$z_2=1$	type of fold
1	1	no fold
1	1	complete fold
1	1	acute fold
1	1	obtuse fold

After a complete turn around a node, the constraint that we recover the same tangent vector translates into the following two constraints on the spins. The first constraint

$$\sum_{i=1}^6 z_i = 0 \pmod{3} \quad (2.6)$$

is the same as the constraint (2.3) for planar folding, and ensures that we recover the same color of the tangent vector. The second constraint deals with the z variables⁶ and reads

$$\sum_{i=1}^3 z_i z_{i+1} = 1; \quad x = 1; 2; 3 \quad (2.7)$$

P_i such that:
j = x mod 3

The left hand side simply counts the number of sign changes of the z variable across the links of color A, B or C (one color for each value of x), which are nothing but the sign changes of the complementary variable A, B and C respectively. Eq. (2.7) ensures that we recover the same value of the complementary variables after a complete turn.

In terms of constrained spins, it is easy to count all the environments allowed by the constraints (2.6) and (2.7) around a vertex. There are 96 such environments, which are represented in Fig.15. As such, the FCC folding of the triangular lattice is a 96-vertex model.

It is interesting to note that this model has the following three sub-models (see Fig.15):

1. A 11-vertex model corresponding to the planar folding obtained by keeping only either unfolded or completely folded links. This amounts to requiring that $z = 1$ for all the triangles, in which case (2.7) is automatically satisfied and one recovers the constraint (2.3).

⁶ Note that the relation for $x = 3$ is a consequence of those at $x = 1; 2$.

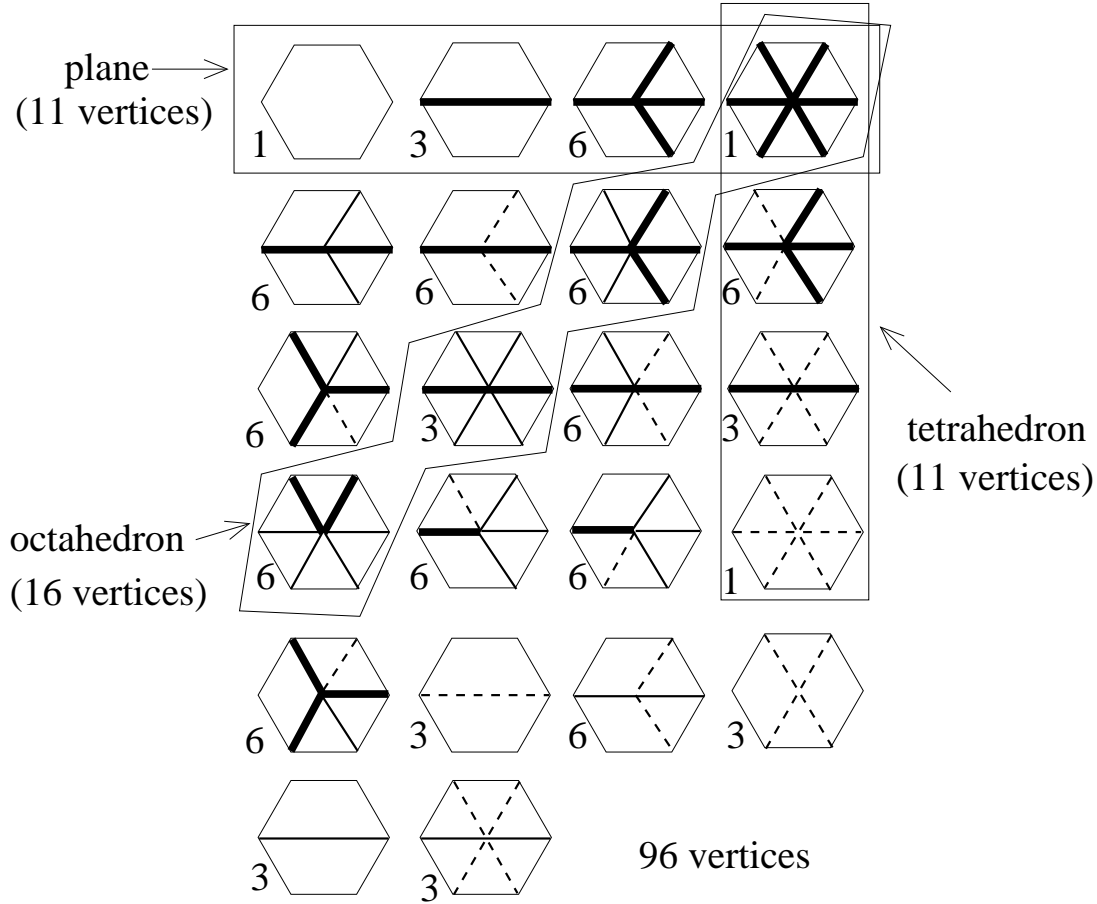


Fig.15: The 96 folding configurations of an elementary hexagon. The complete folds are indicated by thick lines, the obtuse folds by thin lines and the acute folds by dashed lines. For each environment, we have indicated its multiplicity corresponding to rotations of the hexagon. We also indicated the vertices which have to be retained for the three sub-models corresponding to the planar folding (11 vertex), the folding on a single tetrahedron (11 vertex) and that on a single octahedron (16 vertex).

2. An 11-vertex corresponding to the folding on a single target tetrahedron, obtained by keeping only acute or complete folds. This amounts to requiring that $z = \pm 1$ where $z = 1$ on triangles pointing up and $z = -1$ on triangles pointing down. Once again, the relation (2.7) is automatically satisfied.
3. A 16-vertex model corresponding to the folding on a single target octahedron, obtained by keeping only obtuse or complete folds. This amounts to having a perfect anti-ferromagnetic order $z_i = (-1)^i$, with z_i as defined above, in which case the relation (2.7) becomes $\prod_{i=1}^6 z_i z_{i+1} = 1$.

Note that the constraints (2.6) and (2.7) are invariant under the change $(z) \rightarrow (-z)$. One thus gets a duality relation which consists in exchanging globally all the unfolded

edges with those carrying an acute fold, as apparent in Fig.15. The sub-model 3 above is self-dual while the two sub-models 1 and 2 are dual of one another. In particular, the entropy of folding on a single tetrahedron is the same as that for the planar folding, and given by Eq.(2.5).

The entropy of folding on the FCC lattice is not known so far. Numerical estimates [6] show that $q = 1.43(1)$. We may easily show that $q > \frac{p}{2} = 1.414$ by estimating the entropy of the sub-model 3 of folding on a single octahedron. Indeed, the constraint $\prod_{i=1}^6 z_i z_{i+1} = 1$ amounts to requiring that z is the product $v_1 v_2 v_3$ on the three nodes v_1, v_2 and v_3 adjacent to the face at hand of a node variable v equal to ± 1 and independent on each node of the lattice. The model 3 has therefore an entropy of 2 per node, i.e. $\frac{p}{2}$ per triangle.

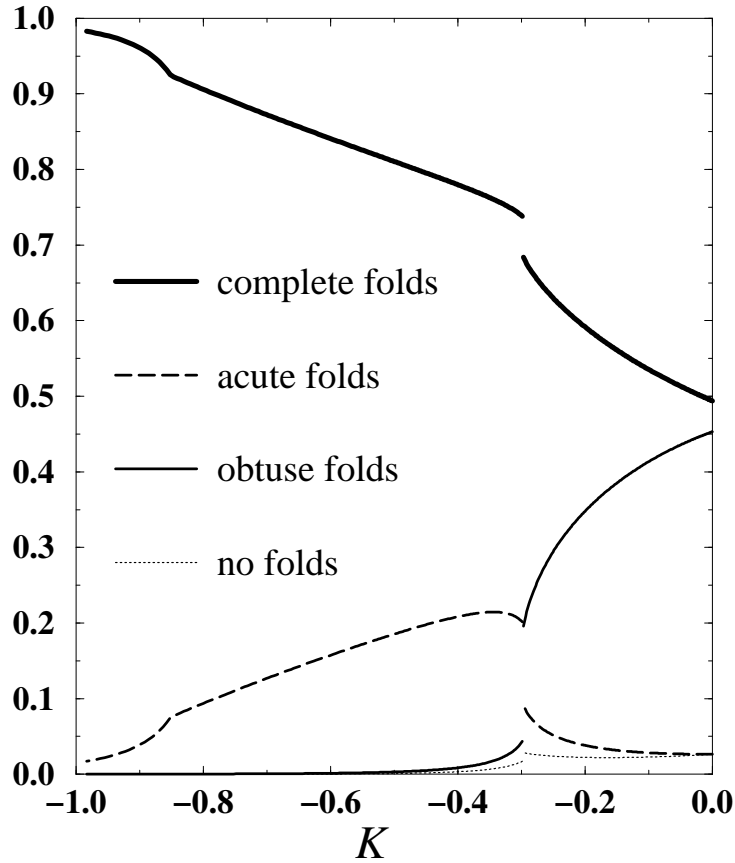


Fig.16: The proportion of the different types of folds as a function of the rigidity modulus K (energy $E_b = K \cos(\theta)$) in the range $K < 0$.

We may finally consider the phase diagram obtained by introducing a bending energy, again in the form of a link energy $E_b = K \cos(\theta)$ where θ is the folding angle (none,

complete, acute or obtuse). This phase diagram was obtained in Ref.[8] by use of a variational method (see also Ref.[29]). As for planar folding, one finds in the regime $K < 0$ a first order flattening/crumpling transition between a crumpled phase for small values of K and a completely flat phase for large values of K . The situation for $K > 0$ (i.e. for which folds are favored) is richer: the figure 16 displays the proportion of the different types of folds as a function of K . One clearly distinguishes two successive folding transitions. A first, discontinuous transition at $K \approx 0.3$ separates a regime where the folding occurs preferentially on octahedra from a regime where it occurs preferentially on tetrahedra. A second, continuous transition at $K \approx 0.85$ separates this last regime from a regime where the folding is essentially maximal with dominance of complete folds.

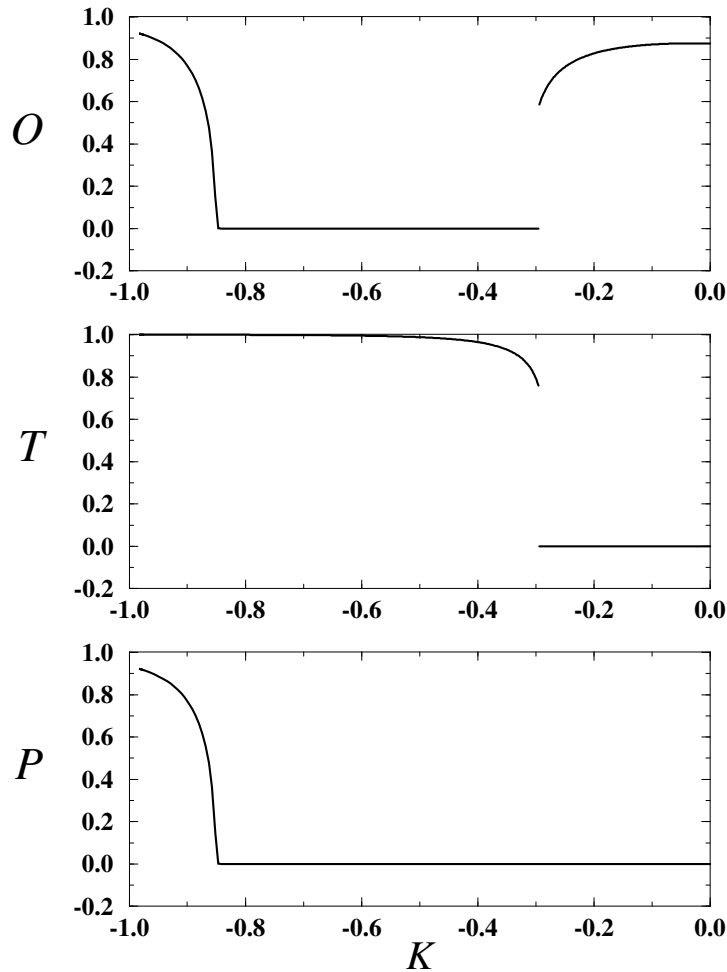


Fig.17: The three order parameters O , T and P as defined in the text as a function of the rigidity modulus K (energy $E_b = -K \cos(\theta)$) in the range $K < 0$.

These transitions may also be viewed on the three order parameters O , T and P defined as

$$\begin{aligned} O &= \langle h_i \rangle \\ T &= \langle h_z \rangle \\ P &= \langle h_{zi} \rangle \end{aligned} \tag{2.8}$$

and represented in Fig.17. The interpretation of these order parameters is that a non-vanishing value of O (respectively of T) shows a tendency of the lattice to fold preferentially around octahedra (respectively around tetrahedra). Similarly, a non-vanishing value of P shows a tendency of the lattice to preferentially remain within planes of the FCC lattice.

This completes our study of phantom folding of 2D regular lattices. Here we have concentrated on the folding of the triangular lattice in $d = 2$ and 3 dimensions. We expect the same type of conformational transitions to take place for higher target dimensions d , with a first order crumpling transition to a completely flat state at a positive value of the bending rigidity K , a continuous (Ising type) piling-up transition at a negative value of K toward a limiting completely folded state, and a new structure of intermediate transitions of wrapping around intermediate-dimensional regular solids. Finally, we expect a similar scenario to happen for all the compactly foldable lattices of Fig.5 (including the rectangular lattice case as a degenerate limit with zero entropy). This scenario is confirmed in the case of the square-diagonal lattice in Ref.[25].

PART B : LOOP MODELS ON REGULAR LATTICES

In this part, we show that folding problems are particular instances of a larger class of problems, so-called fully packed loop models [30], with possible reformulations as height models for which the loops play the role of contour plots. We focus here again on regular lattices and illustrate the techniques of solution in the case of fully packed loops on the hexagonal lattice. These include Bethe Ansatz calculations [31] and effective Coulomb gas descriptions [32].

3. Loop gas and height model reformulations of the triangular lattice folding

Very generally, all lattice folding problems can be reformulated as fully packed loop gases on the dual lattice. We will illustrate this property in the two cases of the $d = 2$ (planar) and $d = 3$ (FCC) foldings described in the previous Section.

3.1. Fully packed loop gas formulations of the 2d folding

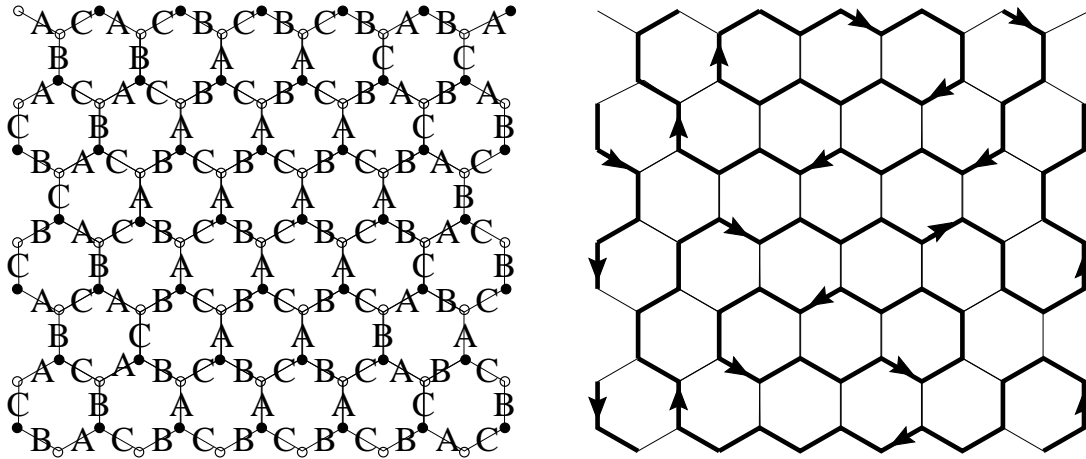


Fig.18: Example of tricoloring of the links of the hexagonal lattice and the associated configuration of oriented fully packed loops.

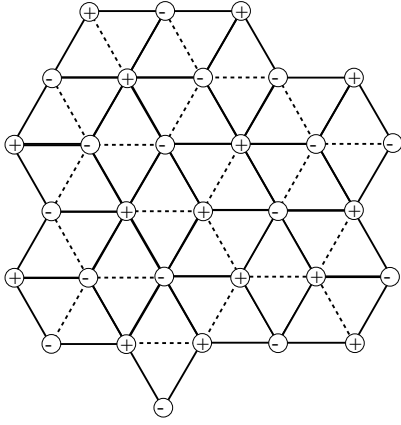
Let us first consider the planar folding of the triangular lattice. As seen in Section 2.2, it is equivalent to the tricoloring of the links of the hexagonal lattice with three colors A, B and C, required to be distinct on the three links adjacent to any node of the lattice. Note that the hexagonal lattice is bipartite, i.e. it may be decomposed into two sub-lattices of black, resp. white nodes, such that the neighbors of a black node are white and conversely.

The black or white color of a node is equivalent to the "\pointing up" or "\pointing down" nature of the dual triangle. Ignoring the links of color A, the links of color B or C form loops on the hexagonal lattice along which the colors B and C alternate (see Fig.18). By orienting all the links of color B from the adjacent black node to the adjacent white node, and the links of color C from the adjacent white node to the adjacent black node, we orient each loop in a coherent way. Changing the orientation of a loop simply amounts to interchanging the colors B and C along this loop. The gas of oriented loops thus obtained is self-avoiding and fully packed, in the sense that each node of the lattice is visited by a loop.

Conversely, given any set of fully packed oriented loops, it is possible to reproduce the associated colors for all the links, and therefore to rebuild the associated folding configuration. This shows that the planar folding of the triangular lattice is equivalent to a gas of fully packed oriented loops on the hexagonal lattice.

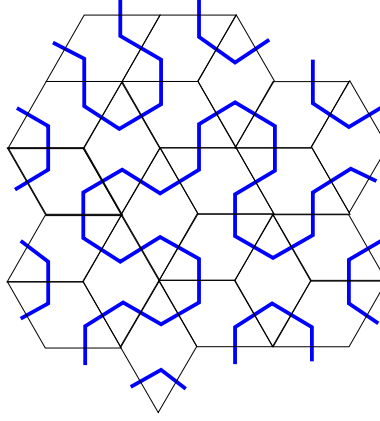
The orientation of the loops may be rephrased into a weight $n = 2$ per unoriented loop. More generally, we may consider the so-called FPL(n) model of a gas of fully packed, self-avoiding and unoriented loops on the hexagonal lattice with a weight n per loop [30]. This is to be compared with the loop gas formulation of the so-called $O(n)$ model on the hexagonal lattice which also amounts to consider self-avoiding loops with a weight n per loop but without the requirement that every node of the lattice be visited by a loop [32].

Note that the $O(n)$ model is originally defined as a spin model with $O(n)$ symmetry. Similarly, the FPL(2) model alternatively describes the groundstates of the antiferromagnetic XY model (spins with $O(2)$ symmetry) on the Kagome lattice [33]. Indeed, the nodes of the Kagome lattice are in one-to-one correspondence with the edges of the triangular lattice. The tangent vectors of the folding configuration yield spins on the nodes of the Kagome lattice. The constraint (2.1) of vanishing sum around a triangle is nothing but the condition for the minimization of the antiferromagnetic energy $t_1 - t_2 + t_2 - t_3 + t_3 - t_1$ (together with $\sum_{i=1}^3 t_i = 1$) around each elementary triangle of the Kagome lattice. In the same spirit, the FPL(1) model describes the antiferromagnetic groundstates of the Ising model on the triangular lattice, as illustrated in Fig.19-(a,b). The loops on the (dual) hexagonal lattice are easily identified with the links dual to the $+j$ (i.e. energetically favored) links on the triangular lattice. The fully packed requirement amounts to maximizing the number of these favored links (exactly 2 per triangle).



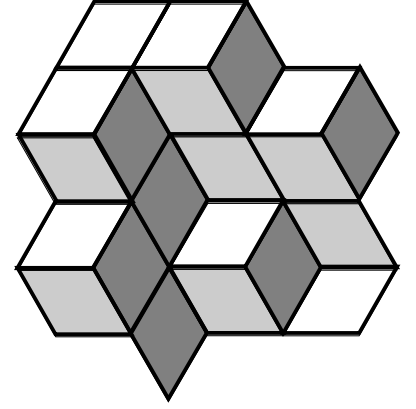
Antiferromagnetic groundstate

(a)



Fully packed loops

(b)



SOS interface

(c)

Fig.19: Equivalence between (a) antiferromagnetic groundstates of the Ising model on the triangular lattice, (b) FPL (loop) configurations on the dual hexagonal lattice, and (c) Solid-On-Solid (SOS) interfaces for piling-ups of cubes viewed in perspective. In (a), there is exactly one frustrated link (with equal adjacent spins) per triangle (dashed lines). The frustrated links are dual to the unoccupied edges in (b) while the links dual to the $+$ links form a gas of fully packed loops on the hexagonal lattice. Erasing the frustrated links yields a rhombus tiling of the plane, also interpreted as a piling-up of cubes viewed in perspective (c).

3.2. Fully packed loop gas formulations of the 3d folding

In the case of the folding of the triangular lattice on the FCC lattice, we have seen that the link variables again induce a tricoloring of the links of the triangular lattice, and thus, by duality, of the links of the hexagonal lattice. This coloring by three colors A, B and C , as we just saw, is equivalent to the gas of the fully packed BC loops. We may consider as well the two other systems of fully packed loops made of the links AC or the links AB . The three systems of loops are strongly correlated as the knowledge of one of them allows us to reconstruct the two others. The colors are not sufficient however to characterize entirely the original 3d folding. To this end, we have introduced the additional link variables $A; B; C = \pm 1$ indicating, in the elementary octahedron, the side of the plane of color A, B, C respectively on which the link variable at hand lies (see Fig.13). If we now consider any BC loop, it is easy to see that the value of A is constant along the loop. Indeed, a change of sign of A requires to cross the plane of color A on the elementary octahedron and therefore to pass through a link of color A , which in turn requires to pass

from one BC loop to another one. Moreover, the value of A is independent on each of the BC loops. The same is true for the variable B on the AC loops and the variable C on the AB loops. As a consequence, we may represent any folding on the FCC lattice by a tricoloring of the hexagonal lattice, completed by a \mathbb{Z}_2 spin variable on each of the BC, AC and AB loops. The enumeration of 3d foldings is therefore performed by counting tricolored configurations with a weight 2 for each of the AB, BC and AC loops.

To conclude, we may write the partition functions for 2d and 3d foldings as partition functions for edge-tricolorings or fully packed loop gases as

$$\begin{aligned}
 Z_{\text{plane}} &= \sum_{\text{Tricolorings}} 1 = \sum_{\text{Fully packed loops}} 2^{\# \text{ loops}} \\
 Z_{\text{FCC}} &= \sum_{\text{Tricolorings}} 2^{\# \text{ AB loops}} 2^{\# \text{ BC loops}} 2^{\# \text{ AC loops}}
 \end{aligned} \tag{31}$$

Other folding problems were considered [25], such as the planar folding of the square-diagonal lattice, or of the triangular-diagonal lattice. All these problems are equivalent to gases of fully packed loops on appropriate lattices.

3.3. Height models

We shall now transform the FPL(2) configurations into those of a height model defined as follows [34]. We start with a gas of oriented fully packed self-avoiding loops. To each face of the hexagonal lattice, we associate a "height" X in \mathbb{R}^d whose variation from one face to another depends on whether the separating edge is occupied or not by a loop. The precise rules for the variation of heights are indicated in Fig.20 and use explicitly the bipartite nature of the hexagonal lattice, with different conventions according to whether the link is oriented from a white or from a black node. These rules use three elementary height differences A, B and C. If we now replace the oriented loops by the corresponding tricoloring of the links as in Fig.18, the height difference is simply given by the color A, B or C of the crossed link.

Inspecting the allowed configurations around a node, we see that we must impose the constraint $A + B + C = 0$ in order to have a well-defined height after one turn around a node (see Fig.20-(a)). This naturally leads to a two-dimensional height X . As we shall see below, the components of X become two scalar fields in a continuous effective description, and the FPL(2) model is indeed a critical model described in the continuum by a conformal field theory (CFT) of central charge 2 corresponding to these two height components [35].

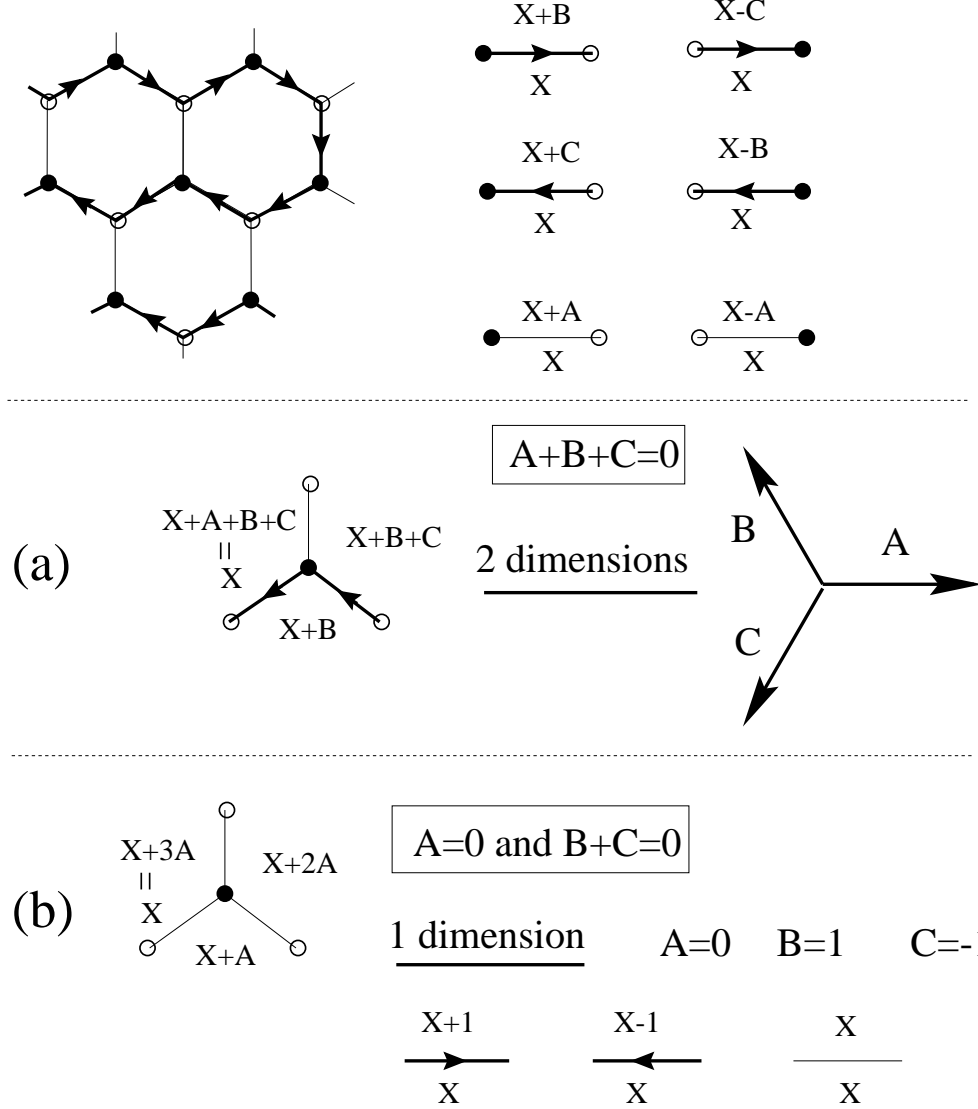


Fig 20: Definition of the height variables X for fully packed loops on the hexagonal lattice. The rule explicitly uses the bicoloring of the nodes of the hexagonal lattice. In the case of fully packed loops, the only possible environment is (a) (up to obvious symmetries), and the consistency of the definition of the heights imposes $A + B + C = 0$. In the case of loops not necessarily fully packed, the presence of unvisited nodes with the environment (b) imposes moreover that $A = 0$, in which case $B = -C$ ($= 1$ for instance) and the rules become insensitive to the bicoloring of the nodes of the hexagonal lattice.

A symmetric solution consists in choosing A to be a unit vector, $B = R A$ and $C = R^2 A$ where R is the rotation of angle 120° in the plane. With this choice, for any given oriented loop configuration, we may identify the height X of a face with the position of its dual node in the associated folded configuration of the triangular lattice in the plane. The above

symmetric solution will be used from now on.

As described above, the $O(2)$ model corresponds to releasing the full-packing constraint by allowing for nodes which are not visited by loops. In this case, we must also include the configuration of Fig 20-(b) corresponding to an unvisited node. The consistency of heights after one turn around the node now imposes the extra constraint $A = 0$, and thus $B + C = 0$. This now leads to a one-dimensional height. The corresponding loop gas is critical for a suitable choice of edge weight. At this critical point [32], the model is described in the continuum by a CFT of central charge 1. Notice that the rules defining the heights in this case are now insensitive to the bipartite nature of the lattice (see Fig 20-(b)).

Surprisingly, the full-packing constraint influences the value of the central charge, and thus the universality class of the model. More precisely, as first recognized in Ref.[30], the net effect of the full-packing constraint has been to increase the central charge by 1. We shall recover a similar property below in the case of random lattices.

For $n = 1$, the FPL(1) model may be described by a one-dimensional height. This is readily seen on Fig.19-(c). Indeed, any configuration of the model may be interpreted as a piling of unit cubes in R^3 viewed in perspective from the direction $(1;1;1)$ and whose free surface is connected and has no overhangs. This surface may be entirely described by a single height $h = X - A$ with X obtained from the rules of Fig 20 for some arbitrary orientation of the loops (indeed this height is insensitive to the choice of orientation as $B - A = C - A$). As we shall see in the next Section, the model is critical with central charge 1, as opposed the case of the $O(1)$ model which has central charge 0 (in its dense phase).

4. Exact solutions via Bethe Ansatz: the example of the FPL(1) model

Exact solutions for the general FPL(n) models with arbitrary n may be obtained by transfer matrix methods together with Bethe Ansatz type assumptions on the eigenvectors. The existence of such solutions is granted by the integrability of the models. The Bethe Ansatz needed in the general solution is of "nested" type, which makes the explicit solutions quite technical [37]. In the case $n = 1$ however, the problem simplifies drastically and reduces to a free fermion model. The latter may be treated via a simple coordinate Bethe Ansatz. For pedagogical purposes, we choose to describe only this case in detail in the following Sections. In particular, we will compute the value $c = 1$ of the central charge for the conformal field theory that describes the large distance behavior of the model. We will return to the general case in Section 5 where we present an effective field theoretical description of FPL(n) via Coulomb gas.

4.1. F P L (1) and rhombus tiling of the plane

In this Section, we address the F P L (1) model, which, as illustrated in Fig.19, may be rephrased as the problem of tiling a domain of the plane by means of any number of the three following rhombic tiles:

$$= \begin{array}{c} \diagup \\ \diagdown \end{array} \quad = \begin{array}{c} \diagdown \\ \diagup \end{array} \quad = \begin{array}{c} \diagup \quad \diagdown \\ \diagdown \quad \diagup \end{array} \quad (4.1)$$

with edges of unit length and angles of 60° and 120° , all weighted by 1. As it turns out, the specific shape of the domain to be tiled is extremely important. One can show for instance that a large rhombus of size $N \times M$ may be tiled in exactly $\frac{N+M}{N}$ distinct manners, resulting in a vanishing thermodynamic tiling entropy $s = \lim_{N, M \rightarrow \infty} \frac{1}{NM} \text{Log} \frac{N+M}{N} = 0$. On the other hand, a large hexagon with size $N \times M \times P$ may be tiled in many more ways, namely [36]

$$\sum_{i=1}^N \sum_{j=1}^M \sum_{k=1}^P \frac{i+j+k}{i+j+k+2} \quad (4.2)$$

which results in a non-vanishing thermodynamic entropy of tiling. It is not our purpose here to study the influence of boundary conditions on the entropy of tiling, but just to compute it in some generic situation, namely that of a large cylinder represented by a rhombus of width L and length $M \rightarrow \infty$, the two longitudinal sides of the rhombus being glued.

In the next Sections, we use the following strategy, quite standard for solving integrable lattice models (the particular example at hand is borrowed from a course delivered by B. Nienhuis at the 1997 Beg-Rohu school "Ecole de physique de la matiere condensée"). We first define the row-to-row transfer matrix T_L of the model, with periodic boundary conditions along a row of L tiles. The partition function of the model on a rhombus of size $L \times M$, say with doubly periodic boundary conditions (torus) reads then

$$Z_{L, M} = \text{Tr}(T_L^M) \quad (4.3)$$

To access the thermodynamic properties of the model, we must take a large L, M limit. Concentrating on a strip of fixed width L , the thermodynamics ($M \rightarrow \infty$) is simply governed by the largest eigenvalue of T_L , with a thermodynamic tiling entropy per tile of

$$s = \lim_{M \rightarrow \infty} \frac{1}{LM} \text{Log} Z_{L, M} \quad (4.4)$$

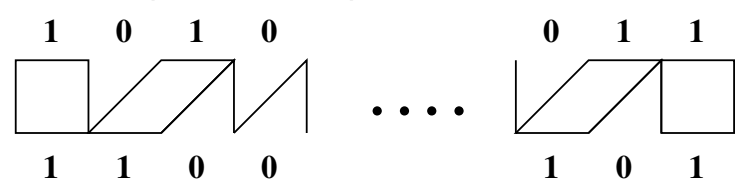
We then use the expected conformal limit of the model to identify the central charge by studying the finite size effects on a cylinder of finite but large width L .

4.2. Transfer matrix and eigenvalue equations

Consider a horizontal row, tiled with a number of tiles \square , \parallel , and with total length L . For simplicity, we deform slightly the three tiles into the following

$$= \text{parallelogram} = \square = \text{trapezoid} \quad (4.5)$$

This amounts to consider the partition function of the rhombus tiling model on a rectangle of size $L \times M$ with its vertical edges identified so as to form a cylinder. The transfer between a tiled horizontal row to the next (say from bottom to top) is then described by assigning an occupation number $n_i = 0; 1$ (resp. n_i^0) to each lower (resp. upper) horizontal edge, resulting in the transfer matrix element $(T_L)_{f n_1^0 n_2^0 \dots n_L^0 g; f n_1 n_2 \dots n_L g}$ from a configuration \mathfrak{n} of occupation numbers of a horizontal row of edges to the next \mathfrak{n}^0 , that typically reads pictorially

$$(T_L)_{f 1; 0; 1; 0; \dots; 0; 1; g; f 1; 1; 0; 0; \dots; 1; 0; 1; g} =$$


$$(4.6)$$

Note that the number k of 1's is conserved from a row to the next, and counts the total number of \square or \parallel tiles in the row.

Starting from a row with only \square tiles, the next row can only consist of \square tiles as well. This forms the "fundamental" invariant sector, with $k = 0$. This unique possibility is summarized by the transfer matrix element

$$(T_L)_{f 0; 0; \dots; 0; g; f 0; 0; \dots; 0; g} =$$


$$(4.7)$$

Note that all the upper and lower horizontal edges are unoccupied. We conclude that the "no-occupied" edge state is an eigenstate of T_L with eigenvalue $\lambda_0 = 1$.

An excitation of this groundstate is obtained by replacing one pair of adjacent halves of \square tiles along the row by either an \square or a \parallel tile. Assume the occupied lower edge of the tile is in position $x \in \mathbb{Z}_L$ (with periodic boundary conditions $L \equiv 0$) along the row, then the upper one is necessarily in position x (\square tile) or $x + 1$ (\parallel tile). Let us denote by $v(x)$

the lower edge configuration vector $f(0;0;\dots;0;1;0;\dots;0)$ with a 1 in position x . We then have

$$T_L v(x) = \begin{array}{c} v(x) \\ \text{Diagram 1: A sawtooth pattern with a square at position } x. \end{array} + \begin{array}{c} v(x+1) \\ \text{Diagram 2: A sawtooth pattern with a square at position } x+1. \end{array} \quad (4:8)$$

We must consider multiple excitations of the groundstate as well. In the k -excitation sector, k of the pairs of adjacent half-tiles must be replaced by \square or \square tiles. This results in the appearance of k occupied lower and upper edges. This conservation of the number of occupied edges from one row to the next is an important feature of the model. It allows to break the action of the transfer matrix T_L into $L+1$ sectors, according to the number of excitations $k \in \{0,1,2,\dots,L\}$. The invariant space corresponding to k excitations has dimension $\binom{L}{k}$. For instance, in the case of $k=2$ excitations, we must replace two of the pairs of adjacent half-tiles by \square 's or \square 's. The corresponding lower occupied edges are in positions say x and y , $0 \leq x < y \leq L-1$. Let us denote by $v(x;y)$ the edge configuration vector with only 0's except for two 1's in positions x and y . Just like in the 1-excitation case, the occupied upper edges must be in positions x or $x+1$ and y or $y+1$, with moreover the constraint that they be distinct. Forgetting about this constraint, we would simply have

$$T_L v(x;y) = v(x;y) + v(x+1;y) + v(x;y+1) + v(x+1;y+1) \quad (4:9)$$

Imposing the constraint on the right hand side requires that, whenever $y = x+1$, the second term should be removed, as well as the third one whenever $y = L-1$ and $x = 0$. There is a much simpler way of automatically ensuring this: we simply enhance the domain of definition to $x \in [0;L]$ and demand that $v(x;x) = 0$ for all x , and that $v(x;L) = v(0;x)$ for all x .

The k -excitation sector is easily constructed. Let $v(x_1;x_2;\dots;x_k)$ be the edge-configuration vector with 1's in positions $x_1 \leq x_2 \leq \dots \leq x_k$, with the convention that it vanishes whenever any two consecutive positions are equal, and that $v(x_1;x_2;\dots;x_{k-1};L) = v(0;x_1;\dots;x_{k-1})$. Let us also introduce the translation operator τ_j that adds 1 to the j -th argument of such a vector, namely

$$\tau_j v(x_1;x_2;\dots;x_{j-1};x_j;x_{j+1};\dots;x_k) = v(x_1;x_2;\dots;x_{j-1};x_j+1;x_{j+1};\dots;x_k) \quad (4:10)$$

Note that the result is the zero vector when $x_{j+1} = x_j$ or $x_j + 1$. The transfer matrix then acts in the k -excitation sector as

$$T_L v(x_1; \dots; x_k) = \prod_{j=1}^k (I + T_j) v(x_1; \dots; x_k) \quad (4.11)$$

where I is the identity and the various translation operators commute with one another. The vanishing constraint on the vectors takes care of all the steric constraints for the and tiles.

We now look for eigenvectors of T_L in the form

$$V^{(k)} = \sum_{0 \leq x_1 < x_2 < \dots < x_k \leq L-1} f(x_1; \dots; x_k) \quad (4.12)$$

in the k -excitation sector. The corresponding eigenvalue equation reads

$$T_L V^{(k)} = \lambda V^{(k)} = \prod_{j=1}^k (I + T_j) V^{(k)} \quad (4.13)$$

This equation must be solved within the invariant $\binom{L}{k}$ -dimensional vector space of the k -th sector, with the boundary conditions

$$\begin{aligned} f(\dots; x; x; \dots) &= 0 \\ f(x_1; x_2; \dots; x_{k-1}; L) &= f(0; x_1; \dots; x_{k-1}) \end{aligned} \quad (4.14)$$

4.3. Bethe Ansatz

In view of the equations (4.13), we may naturally think of trying some simple Ansatz for the candidate eigenvectors, based on the eigenvectors of the translation operator. Indeed, for $k=1$, $f(x) = z^x$ produces an eigenvector for T , for any non-zero z . The k -variable version is $f(x_1; \dots; x_k) = z_1^{x_1} z_2^{x_2} \dots z_k^{x_k}$, for some non-zero complex numbers $z_1; z_2; \dots; z_k$. This Ansatz would work perfectly except that it violates the boundary condition, that f vanishes whenever two consecutive arguments are equal.

The next fundamental remark is that if we still ignore the boundary condition, any permutation $\sigma \in S_k$ of the x 's would yield an equally acceptable candidate $f(x_1; x_2; \dots; x_k) = z_1^{x_{\sigma(1)}} z_2^{x_{\sigma(2)}} \dots z_k^{x_{\sigma(k)}}$, with the same eigenvalue.

The idea of the Bethe Ansatz is then to combine these two ideas and look for a solution of the eigenvalue equation (4.13) that is a linear combination of the f , $\sigma \in S_k$, and that

incorporates the boundary conditions (4.14). In the present problem, the answer is unique and reads

$$f(x_1; x_2; \dots; x_k) = \det(z_i^{x_j})_{1 \leq i, j \leq k} \quad (4.15)$$

Moreover, the periodic boundary conditions (second line of (4.14)) along the strip are satisfied if

$$\begin{aligned} z_i^L &= (-1)^{k-1} \quad \text{for all } i = 1, 2, \dots, k \\ z_r &\neq z_s \quad \text{for all } r, s = 1, 2, \dots, k; \quad r \neq s \end{aligned} \quad (4.16)$$

where the extra condition that the z_i must be distinct ensures that the eigenvectors are non-zero. These are the celebrated Bethe Ansatz equations, in our particularly simple case. Note that we indeed get a basis of the $\frac{L}{k}$ -dimensional invariant space by taking f as in Eq.(4.15) with

$$\begin{aligned} z_j &= e^{2i(n_j - \frac{k-1}{2})=L} \quad j = 1, 2, \dots, k \\ 0 &\leq n_1 < n_2 < \dots < n_k \leq L-1 \end{aligned} \quad (4.17)$$

The corresponding eigenvalues read

$$\lambda_k(n_1; \dots; n_k) = \prod_{j=1}^k (1 + e^{2i(n_j - \frac{k-1}{2})=L}) \quad (4.18)$$

4.4. Continuum limit: largest eigenvalue

The continuum thermodynamic limit of the model corresponds to $L, M \rightarrow \infty$. For L finite and $M \rightarrow \infty$, the thermodynamic limit of the free energy of the model is governed by the largest eigenvalues of T_L . More precisely, we may compute the entropy of tiling per row of a strip of finite length and finite width L by taking the large M limit of (4.3) $S_L = \lim_{M \rightarrow \infty} \frac{1}{M} \text{Log } Z_{L, M}$. Using the explicit form (4.18), the largest eigenvalues are obtained by having the maximum number of terms $(1 + z_j)$ that are larger than one in module.

We have represented in Fig 21 the unit circle and its shifted image under $z \rightarrow 1 + z$. Only a portion of this image lies outside of the unit circle. Let us denote by $z = e^{2i\theta}$ the two intersections between the two circles of Fig 21. We will have a maximum number of terms $(1 + z_j)$ with modulus larger than one for the value of k_0 such that

$$\frac{k_0 - 1}{2L} < \frac{1}{3} \leq \frac{k_0}{2L} \quad (4.19)$$

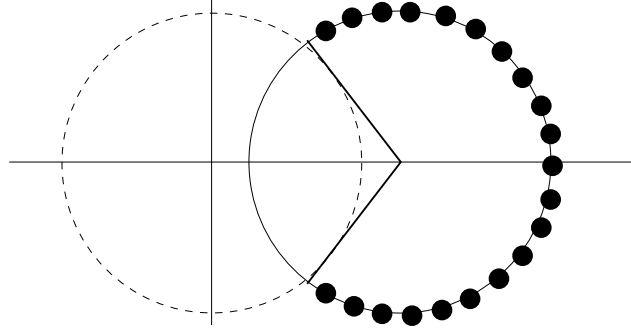


Fig.21: The roots z_j of the Bethe Ansatz equation (4.16) lie in the complex plane on the unit circle (dashed circle). We have also represented the location of their shifted values $(1 + z_j)$ (solid circle). The maximum eigenvalue among the values (4.18) is obtained by retaining only those z_j 's whose shifted value lies outside of the unit circle (black dots) and having as many of these as possible. These correspond to $z_j = e^{i\theta_j}$ with $\theta_j \in [\frac{2\pi}{3}, 2\pi]$.

For simplicity, let us assume that $L = 3n$, in which case (4.19) gives $k_0 = 2n$. The largest eigenvalue reads then

$$\lambda_{2n}(0; 1; \dots; 2n-1) = \prod_{j=0}^{2n-1} (1 + e^{2i\theta_j - \frac{2n-1}{2}\theta_j}) = (3n) \quad (4.20)$$

The corresponding tiling entropy reads

$$S_L = S_{3n} = \frac{1}{3n} \sum_{j=0}^{2n-1} \text{Log}(1 + e^{2i\theta_j - \frac{2n-1}{2}\theta_j}) \quad (4.21)$$

4.5. Thermodynamic entropy and central charge

To get the thermodynamic tiling entropy per tile (4.4), we must also take the large L limit of S_L : $s = \lim_{L \rightarrow \infty} \frac{1}{L} S_L$. We immediately get

$$s = \frac{1}{3} \int_{-1}^1 dx \text{Log}(1 + e^{2ix}) = \frac{1}{\pi} \int_{-\pi}^{\pi} \frac{(1 - \cos x)^{p-1}}{x^2} \sin \frac{2px}{3} \quad (4.22)$$

The central charge may be obtained from the large L corrections to the thermodynamic entropy. From general principles, the large L limit is indeed expected to be described by a conformal field theory if the model is critical and translationally and rotationally invariant as it is presently.

Moreover, the central charge c is extracted by computing the anomaly of free energy of the model on a cylinder of width L , that behaves like

$$f_L = -S_L = -Ls - \frac{c}{6L} \frac{\pi^2}{2} + o\left(\frac{1}{L}\right) \quad (4.23)$$

for large L , with a bulk free energy per tile $f = s$ as above and a central charge c . The non-conventional factor $\frac{p-3}{2}$ is simply due to our deformation of the original rhombus of size $L \times M$ into a rectangle with size $L \times M \frac{p-3}{2}$ in the same units.

The large $L = 3n$ expansion of S_L is easily derived using the following expansion, valid for any sufficiently differentiable function f

$$\begin{aligned}
\sum_{j=1}^{2n-1} f\left(\frac{j}{3n}\right) dx &= \frac{1}{3n} \sum_{j=\frac{2n-1}{2}}^{\frac{2n-1}{2}} f\left(\frac{j}{3n}\right) = \frac{1}{3n} \sum_{j=\frac{2n-1}{2}}^{\frac{2n-1}{2}} \left(f\left(\frac{j}{3n}\right) - f\left(\frac{j}{3n}\right) \right) \\
&= \frac{1}{3n} \sum_{j=\frac{2n-1}{2}}^{\frac{2n-1}{2}} \left(\left(\frac{j}{3n} \right)^0 f^{(0)}\left(\frac{j}{3n}\right) + \frac{1}{2} \left(\frac{j}{3n} \right)^2 f^{(2)}\left(\frac{j}{3n}\right) dx + O\left(\frac{1}{n^3}\right) \right) \\
&= \frac{1}{3(6n)^3} \sum_{j=\frac{2n-1}{2}}^{\frac{2n-1}{2}} f^{(2)}\left(\frac{j}{3n}\right) + O\left(\frac{1}{n^3}\right) \\
&= \frac{1}{6(6n)^2} \sum_{j=1}^{2n-1} f^{(2)}(x) dx + O\left(\frac{1}{n^3}\right) \\
&= \frac{f^{(2)}(1/3) - f^{(2)}(-1/3)}{6(6n)^2}
\end{aligned} \tag{4.24}$$

Applying this to the function

$$f(x) = \text{Log}(1 + e^{2ix}) \tag{4.25}$$

we finally get the expansion of S_L :

$$\frac{1}{L} S_L = s + \frac{p-3}{12L^2} c + O\left(\frac{1}{L^3}\right) \tag{4.26}$$

with

$$c = \frac{1}{2} \frac{p-3}{3} (f^{(2)}(1/3) - f^{(2)}(-1/3)) = 1 \tag{4.27}$$

The above computation therefore confirms the result announced in Section 4.1 that the FPL(1) model is described in the continuum by a CFT with central charge $c = 1$.

5. Effective field theory description via Coulomb gas

5.1. Two-component Coulomb gas for FPL(2)

Let us now see how to construct an effective continuum field theory for the FPL(n) model at large distances. We introduce a continuous description of the heights in the form

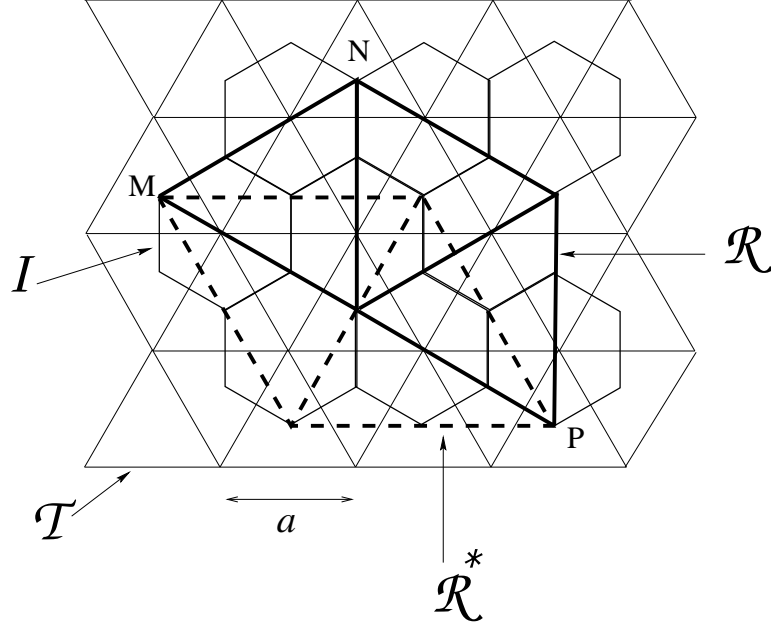


Fig. 22: The triangular lattice T of mesh size a , dual to the hexagonal lattice on which loops are drawn, is the locus of the heights X allowed by the rules of Fig. 20-(a). The ideal lattice I , corresponding to the values of $h = \lfloor X \rfloor$ where the free energy is minimal, is a hexagonal lattice of mesh size $a/\sqrt{3}$. The triangular sub-lattice R of I corresponds to ideal states associated with the same coloring. The mesh size of R is $3a$. Passing from triangle M to triangle N by successive reflections along the edges brings the triangle back in the same orientation. The reciprocal lattice R^* of the lattice R is a triangular lattice of mesh size $2/(3a)$ (here represented for $a = 1/\sqrt{3}$). The smallest non-zero vector of the reciprocal lattice I^* of I is the second smallest vector of R^* , for instance that joining M to P in the figure. Its length is $2/(3a)$.

of a two-dimensional two-component field $h(r) = (h_1(r); h_2(r))$ where $r = (r_1; r_2)$ is the continuous version of the two coordinates of a node on the hexagonal lattice while $h(r)$ is a locally averaged value of the two-dimensional height X around the point r . A precise definition of h is not necessary as only the symmetries of the problem will indeed matter. The approach presented here follows Ref.[34] and is based on two-dimensional Coulomb gas techniques [32].

A first step consists in identifying the so-called "ideal" configurations, i.e. those with a maximal entropy of excitations. We shall indeed assume that the large scale statistics of the problem is dominated by the fluctuations around these ideal states. In the dual language of the planar folding of the triangular lattice, these ideal configurations correspond to maximal foldings, i.e. configurations where the lattice is completely folded onto a single triangle. These compactly folded states are indeed those with the largest number of elementary

excitations obtained by unfolding the six links bordering an elementary hexagon. To each ideal configuration, we may associate the corresponding averaged value of h , equal to the position of the center of mass of the triangle on which the lattice is folded. The corresponding allowed values of h form themselves a hexagonal lattice I of mesh size $a = \frac{P}{3}$ if a is the mesh size of the folded triangular lattice (see Fig.22). We finally write the effective free energy as

$$f = \int d^2r \left[g (\nabla h_1)^2 + (\nabla h_2)^2 + V(h) \right] \quad (5.1)$$

with a Gaussian part describing the height fluctuations and an effective "locking" potential $V(h)$ having the periodicity of the ideal lattice I and enhancing the weight of the ideal states. The "roughness" g will be determined below in a self-consistent way.

In terms of loops, each ideal state corresponds to a regular covering of the hexagonal lattice by means of elementary hexagonal loops of length six, all oriented in the same direction and centered on one of the three sub-lattices of the dual (tripartite) triangular lattice. There are six such tilings corresponding to the six permutations of the three colors ABC . The vertices of the ideal lattice I that correspond to the same covering, i.e. the same coloring, form a sub-lattice R of the ideal lattice I . This so-called "repeat" lattice R is a triangular lattice of mesh size $\frac{P}{3}a$ (see Fig.22). Any local observable of the loop gas must therefore have the periodicity of the lattice R and may thus be written as

$$\langle O(r) \rangle = \sum_{G \in 2R} e^{2i G \cdot h(r)} \quad (5.2)$$

where G runs over the vectors of the reciprocal lattice R^* of R (defined by $G \cdot b = \text{integer}$ for any b in R). The lattice R is a triangular lattice of mesh size $2 = (3a)$ (see Fig.22). On the other hand, the locking potential $V(h) = \sum_{G \in 2R} v_G e^{2i G \cdot h(r)}$ has non-vanishing Fourier components v_G only for $G \in I^*$, the sub-lattice of R^* equal to the reciprocal lattice of the ideal lattice I . The value of g may now be obtained by assuming that $V(h)$ is a marginal perturbation of the Gaussian free field, i.e. with dimension $x = 2$.

Very generally, the dimension of the (electric) "vertex operator" $V_G(r) = e^{2i G \cdot h(r)}$, which describes the large distance behavior of the correlation function $\langle V_G(r) V_{-G}(0) \rangle \sim r^{-2x(G)}$ is equal to [32]

$$x(G) = \frac{G^2}{2g} \quad (5.3)$$

The dimension x of $V(h)$ corresponds to that of the most relevant electric operator (with the smallest $x(G)$) occurring in the Fourier decomposition of $V(h)$, i.e. to the vector G of I with minimal norm (vector MP in Fig.22). The norm of this vector being equal to $2 = \frac{1}{\sqrt{3}}a$, we finally obtain

$$g = \frac{1}{3a^2} \quad (5:4)$$

Once g is fixed, we can obtain exponents describing the large distance behavior of correlations between coloring defects. These take the form of "magnetic operators" defined as follows. A coloring defect around a node of the hexagonal lattice corresponds to a dislocation-type defect in the height X after a complete turn around this node. This height defect reads $X = M = m_1(A - B) + m_2(A - C)$ for two relative integers m_1 and m_2 (the vector M is thus a vector of the lattice R). In order to have a configuration without defect at infinity, we must ensure magnetic neutrality, for instance by introducing another defect with magnetic charge $-M$ at some other node. In this case, the variable X has a jump discontinuity equal to M along a line joining these two defects. The defect/anti-defect correlation then behaves at large separation r as $r^{-2x(M)}$ where the magnetic dimension reads

$$x(M) = \frac{gM^2}{2} = \frac{1}{6} \left(\frac{M}{a} \right)^2 \quad (5:5)$$

A first example of defect consists in having two unvisited sites at distance r from one another. This corresponds to a coloring defect characterized by $M = 3A$ with norm $\frac{1}{\sqrt{3}}a$ and with therefore $x = 3/2$. The fact that $x < 2$ shows that this is indeed a relevant perturbation and that the fully packed loop gas corresponds to an unstable phase with respect to such defects. The introduction of coloring defects is also useful to describe open lines in the loop gas. For instance, we may describe an open BC line linking two points at (an odd) distance r by introducing coloring defects at these two points, each with its three incident edges colored A, A, B . The corresponding value of M is $M = 2A + B$, with norm $\frac{1}{\sqrt{3}}a$, which gives an exponent $x_1 = 1/2$. Very generally, one finds an exponent x_ℓ associated with the large distance behavior of correlations of the form r^{-2x_ℓ} for a set of ℓ BC lines starting from the vicinity of a given point and ending at the vicinity of another at distance r , with the value [34]

$$\begin{aligned} x_{2k} &= \frac{1}{2}k^2 \\ x_{2k+1} &= \frac{1}{2}(k^2 + k + 1) \end{aligned} \quad (5:6)$$

according to the parity of ℓ .

5.2. General FPL(n) and O(n) cases

Beyond the case $n = 2$, the FPL(n) model for $2 \leq n \leq 2$ may be described by configurations of oriented self-avoiding fully packed loops, with weights $e^{+i\theta}$, resp. $e^{-i\theta}$ per right, resp. left turn of the loop. Summing over the two possible orientations of each loop results in a weight $n = 2 \cos(\theta)$ per loop. This holds only for contractible loops while loops escaping at infinity receive a weight 2 instead. To understand how to cure this problem, it is more convenient to define the model on an infinite cylinder, in which case the non-contractible loops wind once around the cylinder and receive a wrong weight 2 instead of n . This is corrected by introducing two electric operators with (two-dimensional) charges E and \bar{E} at both ends of the cylinder, which implies an additional energy term of the form $2iE :h(+1) - h(-1):$. Each non-contractible loop induces a discontinuity $h(+1) - h(-1)$ of B (or C) and it is thus sufficient to choose E such that $E \cdot B = E \cdot C = e=2$, i.e. $E = e(B - C) = 3a$. Summing over the two orientations of the non-contractible loops now yield the correct weight n while contractible loops are unaffected. The introduction of the "background" charge E modifies the dimensions of the electric and magnetic operators into

$$\Delta(G; M) = \frac{1}{2g} G \cdot (G - 2E) + \frac{g}{2} M^2 : \quad (5:7)$$

The value of g is again determined by the requirement that V be marginal. Choosing the determination $0 \leq \theta < 2\pi$ of e , one finally gets

$$g = \frac{(1 - e)}{3a^2} : \quad (5:8)$$

One then finds an exponent $x_\cdot(n)$ associated to the correlation of $\cdot BC$ lines given by

$$\begin{aligned} x_{2k}(n) &= \frac{1}{2} e k^2 - \frac{e^2}{2(1-e)} (1 - k; 0) \\ x_{2k-1}(n) &= \frac{1}{2} e (k^2 - k + 1) - \frac{e^2}{2(1-e)} \end{aligned} \quad (5:9)$$

Finally, the central charge of the model now reads $c = 2 + 12x(E; 0)$, i.e.:

$$c_{\text{fully packed}}(n) = 2 - 6 \frac{e^2}{1-e}; \quad n = 2 \cos(\theta) \quad (5:10)$$

To conclude this study, let us now see how the above formulas are modified in the case of the dense phase of the $O(n)$ model, which as we already saw for $n = 2$, consists

in allowing for the presence of unvisited nodes, in which case the heights become one-dimensional. The above analysis transcribed to this much simpler case leads naturally to a central charge

$$c_{\text{dense}}(n) = 1 - 6 \frac{e^2}{1 - e}; \quad n = 2 \cos(\pi e) \quad (5.11)$$

and to exponents

$$\chi_\nu(n) = \frac{1}{8} \frac{e^{-2\nu}}{(1 - e)^2} \quad (5.12)$$

for any ν .

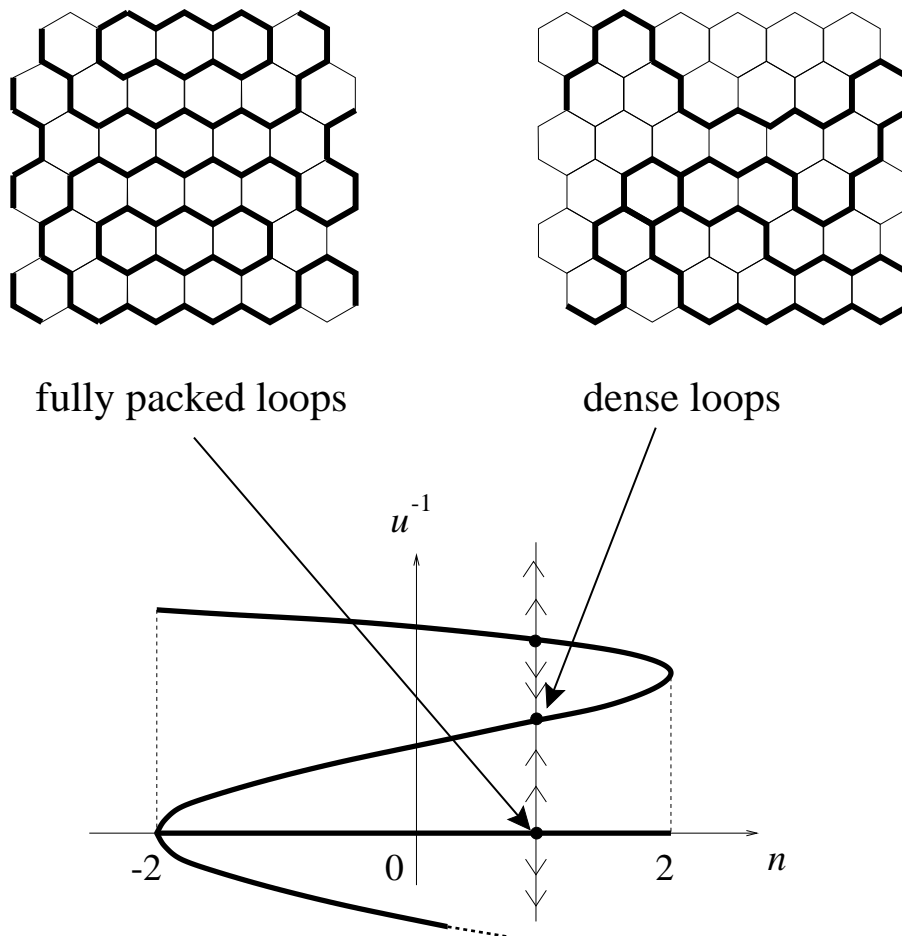


Fig.23: Renormalization flow in the $(n; u^{-1})$ plane. We have indicated an example of flow at constant n . The fully packed loop gas corresponds to an unstable fixed point at $u^{-1} = 0$. The dense loop gas corresponds to a stable fixed point. The central charge decreases by 1 between these two fixed points $c_{\text{dense}}(n) = c_{\text{fully packed}}(n) - 1$.

The lesson to draw from the above is that, at fixed weight n per loop, the fully packed loop gas has a central charge 1 more than the dense loop gas. This result is illustrated in

Fig.23 where we display a diagram of renormalization group flows in the $(n; u^{-1})$ plane, where u is the weight per visited site and $2 \leq n \leq 2$ [30]. All the flows follow lines of constant n and the problem is symmetric under $u \rightarrow 1/u$ (since the number of sites visited by loops is even). The $u^{-1} = 0$ line, which corresponds to the fully packed loop gas, is a line of unstable fixed points (see Fig.23). The presence of defects (which, as we already saw, are relevant) drives the model away from this line towards the line of stable fixed points describing the dense phase of the $O(n)$ model. One also finds another line of unstable fixed points at finite values of $u^{-1} = \frac{p}{2 + \frac{p}{2}n}$ corresponding to the transition points of the $O(n)$ model [30].

PART C : LOOP MODELS ON RANDOM LATTICES

We would like to generalize the models of 2D folding described in part A and those of fully packed loops described in part B to the case of random 2D lattices. By random 2D lattices, we mean tessellations made of 2D polygonal rigid tiles glued together so as to form discrete surfaces with possible curvature defects concentrated at the nodes. We are interested in the phantom folding configurations of statistical ensembles of 2D lattices. These form discrete models for "fluid membranes", i.e. membranes without internal elastic skeleton and whose internal metric fluctuates [2]. Beyond folding, we will also study fully packed loop models on random lattices. All these models are examples of a larger class of statistical models describing the coupling of "matter" degrees of freedom to the fluctuations of "space", used in the quantization of general relativity. More precisely, the present 2D models correspond to discrete realizations of the so-called two-dimensional quantum gravity (2D QG) [38].

In this part, we concentrate on the case of random triangulations or, dually, random trivalent graphs. Various results are presented, relying either on matrix integral techniques [19,39-41] or more general effective 2D QG descriptions [42]. Exact predictions are tested against numerical enumerations [11]. The lesson of this study is a clear distinction between ordinary 2D QG and so-called Eulerian 2D QG corresponding to a restriction of the set of dynamical lattices to Eulerian tessellations.

6. Folding of random lattices

6.1. Foldability of triangulations

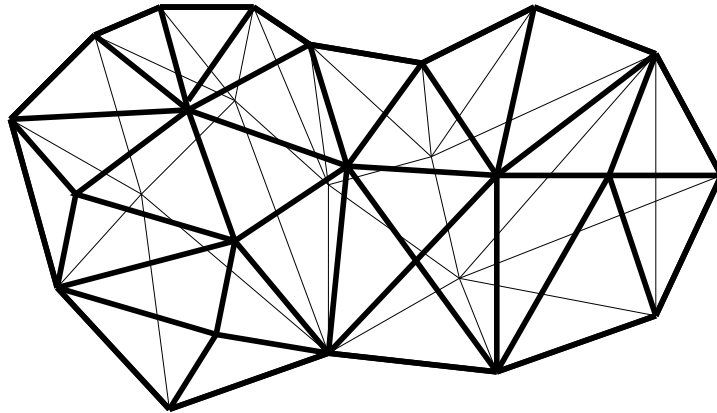


Fig 24 : Example of triangulation with spherical topology.

In this part C, we shall consider only the simplest case of triangulations, for which all the tiles are equilateral triangles with edges of unit length. We will moreover restrict ourselves to planar triangulations, i.e. tessellations of a surface with the topology of the sphere (genus 0, no handles). An example of such a triangulation is given in Fig 24.

Given such a triangulation, we define as before a folding as a map from the triangulation into \mathbb{R}^d such that its restriction to any elementary triangle is an isometry. In particular, each triangle is again mapped onto an equilateral triangle in \mathbb{R}^d .

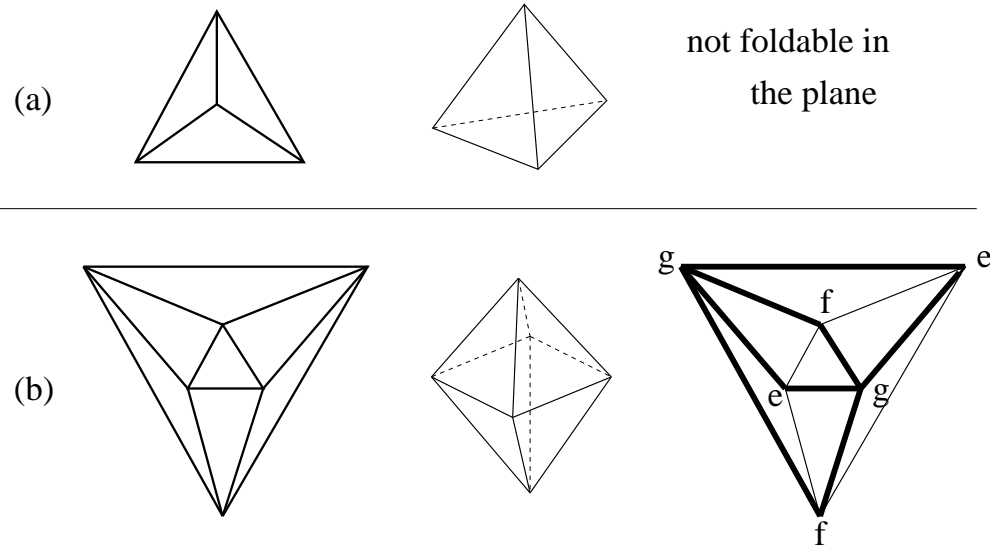


Fig 25: Two examples of planar triangulations: the planar representation (left) keeps track of the connectivity of the triangles only at the expense of deforming them. Note that the external face is also a triangle. The triangulation (a) is foldable into \mathbb{R}^3 on a tetrahedron, but it is not foldable in the plane because its nodes are not tricolorable. The triangulation (b) is foldable into \mathbb{R}^3 on an octahedron and it is foldable in the plane as it is node-tricolorable (here with three colors e, f, g). An example of folding is indicated on the right in the planar representation by thickening the folded links.

In the simplest case of planar folding ($d = 2$), a preliminary question concerns the very existence of such foldings. Indeed, not all triangulations may be folded into the plane. For instance, the triangulation on the top of Fig 25 (which may be embedded in \mathbb{R}^3 so as to form a tetrahedron) cannot be folded into the plane. On the other hand, the triangulation at the bottom of Fig 25 (which may be embedded in \mathbb{R}^3 so as to form an octahedron) can be folded into the plane.

To answer this question, we note that, whenever a folded state exists, the positions in the plane of the nodes of the triangulation necessarily belong to a regular triangular lattice

of mesh size 1 in the plane \mathbb{R}^2 . The triangular lattice is tripartite, i.e. its nodes may be colored with three colors (e,f,g) so that no two adjacent nodes be of the same color. This tricoloring is unique (up to a global permutation of the three colors). If a folded state exists, it therefore induces a tricoloring of the nodes of the triangulation we started from. This yields a necessary condition for the triangulation to be foldable in the plane, namely that it be node-tricolorable. Conversely, starting from a node-tricolorable triangulation, its tricoloring is unique (up to a global permutation of the colors). Such a triangulation may be folded on a single equilateral triangle by sending each node of a given color onto one of the three vertices of this triangle. Such folding corresponds to the complete folding of the triangulation from which other folded configurations may be obtained by partial unfolding.

We obtain finally the following equivalent characterizations:

1. The triangulation is foldable into the plane;
2. The triangulation is node-tricolorable.

In the case of a triangulation with spherical topology, we also have the following equivalent alternative characterizations [43]:

3. Its faces are bicolable (with distinct colors on adjacent triangles);
4. Its edges may be oriented so that the boundary of each triangle receives a well-defined (clockwise or counterclockwise) orientation;
5. The number of triangles around each node is even;
6. The number of edges adjacent to each node is even.

This last property justifies the denomination "Eulerian" for such triangulations as it ensures the existence on the triangulation of a closed Eulerian path (i.e. a path visiting all edges exactly once). In other words, it ensures the possibility of drawing the triangulation by a single (closed) path without lifting the pen.

To summarize, the planar foldable triangulations are the Eulerian triangulations, characterized by any of the above properties 1-6.

6.2. Enumeration of foldable triangulations

The enumeration of Eulerian triangulations was first carried out by W. Tutte [44] in its dual version under the denomination of "bicubic maps". This enumeration may be generalized so as to keep track of the three colors, e.g. with different weights p , q and z for the nodes of color e, f or g respectively [9]. In other words, we enumerate

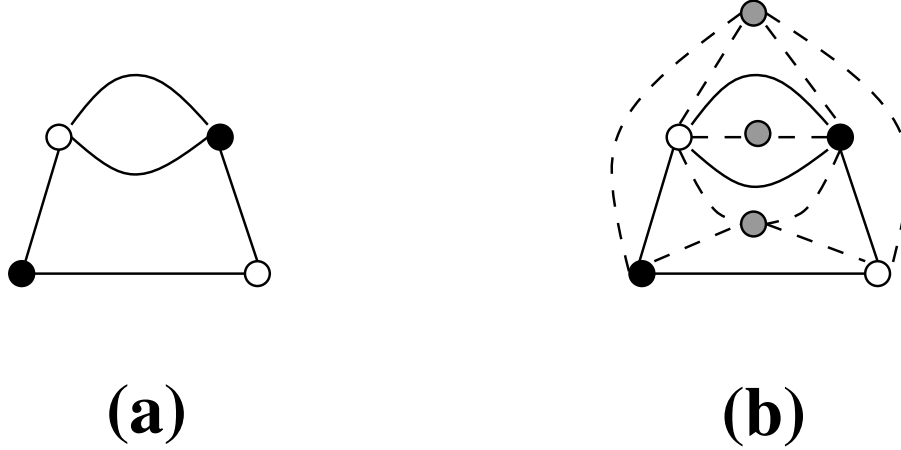


Fig.26: Equivalence between (a) a bicolored graph with arbitrary valences and (b) a tricolored triangulation. From (b) to (a), we simply erase all the nodes of the triangulation of a given color, say, g as well as all the links connected to them. Conversely, from (a) to (b), we note that the nodes around each face have alternating colors e and f . We then re-introduce at the center of each face a node of color g and connect it to all nodes around the face, thus creating triangles.

random triangulations which are completely folded on a single triangle, keeping track of the numbers of nodes sent onto each of the three vertices of the triangle.

This may be performed by use of matrix integral techniques. More precisely, we may compute the generating function $Z(p; q; z; t; N)$ for possibly disconnected vertex-tricolored triangulations of arbitrary genus, with weights p, q, z for the three colors and a weight t per edge of color $e-f$. The parameter N governs the genus via a factor $N^{\chi(T)}$ where $\chi(T)$ is the Euler characteristic of the triangulation at hand. The partition function is defined as

$$Z(p; q; z; t; N) = \sum_{\substack{\text{node tricolored} \\ \text{triangulations } T}} p^{n_e(T)} q^{n_f(T)} z^{n_g(T)} \frac{t^{\frac{A(T)}{2}} N^{\chi(T)}}{|Aut(T)|} \quad (6.1)$$

where $n_{e,f,g}(T)$ denote the total numbers of vertices of color e, f, g , where $A(T)$ denotes the total number of faces (twice the number of $e-f$ edges), and where $\chi(T)$ denotes the Euler characteristic of T . The factor $|Aut(T)|$ is the order of the symmetry group of the tricolored triangulation T .

The construction of a matrix model to represent $Z(p; q; z; t; N)$ is based on the following simple remark: in a given tricolored triangulation T if we remove say all the vertices of color g and all edges connected to them, we end up with a bicolored graph, with unconstrained vertex valencies (see Fig.26). The problem is therefore reduced to the enumeration

of bicolored graphs with a weight p (resp. q) per node of color e (resp. f), a weight z per face and a weight t per link. Such bicolored graphs are easily built out of the Feynman graphs of a two Hermitian matrix model, say M_e and M_f , the index standing for the color. The colored m -valent vertices of the Feynman diagrams read

$$\begin{aligned} \text{Tr}(M_e^m) &= \text{Diagram with } m \text{ solid lines meeting at a central vertex, with a dashed loop on the left.} \\ \text{Tr}(M_f^m) &= \text{Diagram with } m \text{ dashed lines meeting at a central vertex, with a dashed loop on the left.} \end{aligned} \quad (6.2)$$

for all m , and are to be connected via propagator edges with weight t/N while ensuring the alternation of colors e - f

$$h(M_a)_{ij} (M_b)_{kl} = (1 - \delta_{ab}) \delta_{jk} \delta_{il} \frac{t}{N} = \text{Diagram: two vertices connected by two edges (one solid, one dashed).} \quad (6.3)$$

where $a, b = e$ or f . Let us introduce the corresponding matrix integral, but keep N fixed while the matrices are taken of size $n \times n$, n possibly different from N . This gives the partition function

$$\begin{aligned} Z_n(p; q; t; N) &= \frac{1}{Z_n(t; N)} \int dM_e dM_f e^{N \text{Tr} V(M_e, M_f; p; q; t)} \\ V(M_e; M_f; p; q; t) &= p \text{Log}(1 - M_e) + q \text{Log}(1 - M_f) + \frac{1}{t} M_e M_f \end{aligned} \quad (6.4)$$

where the normalization factor $Z_n(t; N)$ ensures that $Z_n(0; 0; t; N) = 1$.

The Feynman graph expansion of the free energy reads

$$\begin{aligned} F_n(p; q; t; N) &= \text{Log} Z_n(p; q; t; N) \\ &= \sum_{\text{bicolored connected graphs}} \frac{1}{\text{Aut}(\gamma)} p^{n_e(\gamma)} q^{n_f(\gamma)} t^{E(\gamma)} N^{(V(\gamma) - E(\gamma))} n^{F(\gamma)} \end{aligned} \quad (6.5)$$

where we have denoted by $n_a(\gamma)$ the number of vertices of color a , $V(\gamma) = n_e(\gamma) + n_f(\gamma)$, $E(\gamma)$ the number of edges, $F(\gamma)$ the number of faces, and $|\text{Aut}(\gamma)|$ the order of the symmetry group of the bicolored graph γ . Adding a central vertex of color g in the middle of each face of γ , and connecting it to all the vertices around the face with edges will result

in a vertex-tricolored triangulation T . The number of such added vertices is nothing but $n_g(T) = F(\cdot)$. Introducing

$$z = \frac{n}{N} \quad (6:6)$$

we may rewrite

$$F_n(p; q; t; N) = F(p; q; z; t; N) \quad (6:7)$$

by use of the Euler relation $2 - 2h(\cdot) = 2 - 2h(T) = V(\cdot) - E(\cdot) + F(\cdot)$ and the fact that $A(T) = 2E(\cdot)$, as each edge of \mathcal{G} gives rise to two triangles of T , one in each of the two faces adjacent to the edge. It is also a simple exercise to show that $|\text{Aut}(T)| = |\text{Aut}(\cdot)|$. Hence computing $F_n(p; q; t; N)$ through the integral formulation (6.4) will yield the generating function for compactly foldable triangulations. In particular, the generating function $f(p; q; z; t)$ for planar tricolored triangulations with a weight p, q, z for the nodes of the three colors and $t^{l=3}$ per edge is obtained by taking the $N \rightarrow \infty$ limit so as to select planar graphs only, and with $n=N = z$ fixed, i.e.

$$f(p; q; z; t) = \lim_{N \rightarrow \infty} \frac{1}{N^2} \text{Log} Z(p; q; t; zN; N) \quad (6:8)$$

An explicit calculation gives [9]

$$t^3 f(p; q; z; t) = \frac{U_e U_f U_g}{t^2} (1 - U_e - U_f - U_g) \quad (6:9)$$

where the functions U_e, U_f and U_g are determined as formal power series of t by the equations

$$\begin{aligned} U_e (1 - U_f - U_g) &= pt \\ U_f (1 - U_g - U_e) &= qt \\ U_g (1 - U_e - U_f) &= zt \end{aligned} \quad (6:10)$$

with the condition $U_a = O(t)$, $a = e, f, g$. This solution was alternatively recovered in Ref.[45] by solving a rectangular matrix model. Remarkably, the functions $U_a=t$ are nothing but generating functions for rooted planar trees with tricolored vertices and a root vertex colored a . For instance, the first line of (6.10) reads $U_e=t = p/(1 - t(U_f=t + U_g=t))$ which is easily seen to generate all trees with root colored e weighted by p and arbitrary many descending subtree of color f or g attached to the root by inner edges weighted by t . The reason for this apparently mysterious coincidence between generating functions for node-tricolored triangulation and node-tricolored trees may be explained in a purely combinatorial way. Indeed, a series of works [46,47] has established bijections between

various classes of planar graphs and possibly decorated trees. In the present case, such a bijection exists which consist in cutting the triangulations so as to form tricolored trees [48,49].

By eliminating U_f and U_g , we get the following 5th order equation for U_e

$$U_e^2 (1 - U_e)^2 (1 - 2U_e + 2(p - q - z)t) = t^2 (1 - U_e)^2 p^2 - U_e^2 (z - q)^2 \quad (6:11)$$

of which we should retain the unique solution with behavior $U_e \rightarrow pt$ at small t . The values of U_f and U_g are obtained from U_e by permuting the weights $p; q; z$.

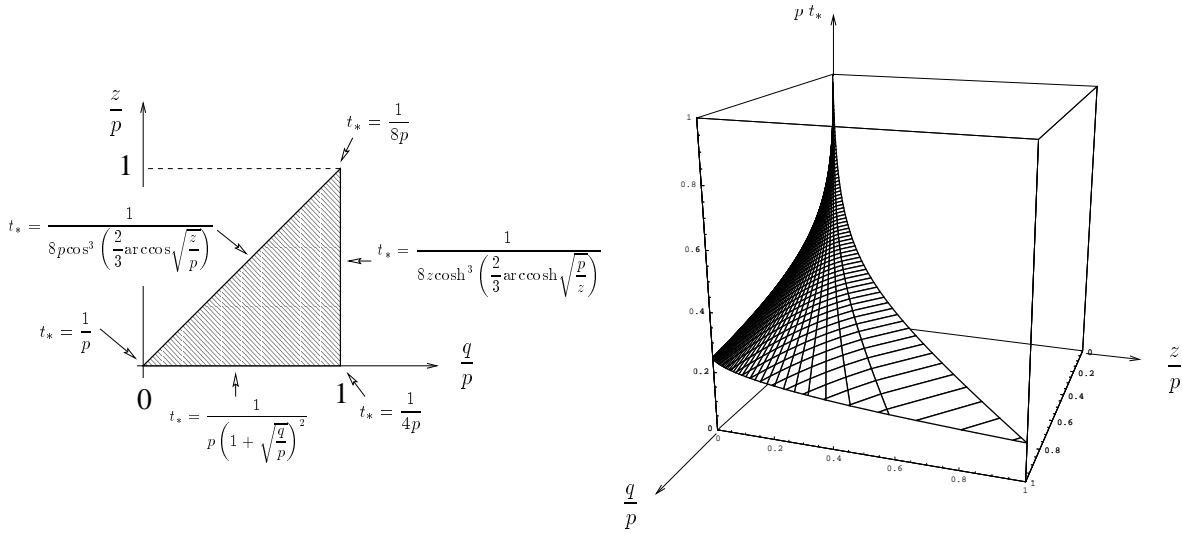


Fig.27: The value of $t_s(p; q; z)$ in the domain z, q, p .

The case $p = q = z$ is much simpler as we may write $U_e = U_f = U_g = U$, where U is the solution of the quadratic equation $U(1 - 2U) = zt$, namely

$$U = \frac{1}{4} \left(1 - \sqrt{1 - 8zt} \right) \quad (6:12)$$

The generating function $f(z; z; z; t)$ therefore reads

$$t \partial_t f(z; z; z; t) = \frac{U^3}{t^2} (1 - 3U) = \frac{z}{8t} - 2 \frac{1}{4zt} \left(1 - \sqrt{1 - 8zt} \right) + 1 - 6zt \quad (6:13)$$

from which we deduce the number N_s of Eulerian triangulations with $3s$ edges (i.e. $2s$ faces) and a marked oriented edge.

$$N_s = \frac{3}{2} 2^s \frac{(2s)!}{s!(s+2)!} - \frac{3}{2^s} = \frac{8^s}{s^{5/2}} \quad (6:14)$$

in agreement with Tutte's result [44]. This result is to be compared to the case of arbitrary rooted planar triangulations with $2s$ faces, which behaves as $(12^{\frac{p}{3}})^s = s^{5/2}$ [39,44].

We deduce from the solution (6.11) that with arbitrary positive weights p, q, z , the free energy $f_s(p; q; z)$ of tricolored triangulations with $3s$ edges behaves generically for large s as

$$f_s(p; q; z) \sim C(p; q; z) \frac{t_2(p; q; z)^s}{s^{\frac{7}{2}}} \quad (6.15)$$

where $t_2(p; q; z)$ is the value of t at which the function U_e becomes singular. By homogeneity, we have $t_2(p; q; z) = (1-p)T(z=p; q=p)$ and, by symmetry, we can restrict ourselves to the domain where, for instance, $z \leq q \leq p$. Figure 27 represents $t_2(p; q; z)$ in this domain and gives some explicit formulas on the boundary of the domain. The value $7/2$ of the exponent in formula (6.15) is a general feature of so-called "pure gravity" models that describe the universality class of fluctuating 2D-space without matter. It is a universal result, common to all planar graph enumeration problems at generic values of their parameters, i.e. without fine-tuning. This is a particular application of the so-called KPZ relations [42] described in detail in Section 7 below, for the coupling to gravity of a trivial conformal matter theory with central charge $c = 0$.

The above enumeration of Eulerian triangulations solves the problem of compact folding, i.e. enumerating configurations of random triangulations completely folded onto a single triangle. The Eulerian nature of a triangulation allows to orient all its links in a coherent way, which in turn allows for a proper definition of the link variables in the form of tangent unit vectors with a vanishing sum around each face. In order to describe the most general foldings of the triangulation, we simply have to assign colors to the links representing the orientation of the corresponding tangent vector in the folded configuration. To obtain all folded states, we have to consider all the tricolorings of these links with three colors A, B or C , distinct around each triangle. In other words, the folding of random planar triangulations is equivalent to the simultaneous tricoloring of the nodes and of the links. As opposed to the tricoloring of the nodes which is essentially unique, the tricoloring of the links is a source of entropy. While the problem of tricoloring of the links only was solved [50,51], the simultaneous tricoloring of both the links and the nodes is still an open question.

7. Statistical models coupled to 2D Quantum Gravity

The problem of folding of random triangulations studied in Section 6 above is a particular case of statistical model coupled to 2D Quantum Gravity (2D QG). This simply means that we replace the underlying regular lattice of some ordinary 2D statistical model by a somewhat arbitrary tessellation of the sphere or of some higher genus surface. The tessellation becomes therefore part of the configuration to be summed over. Such models were introduced as discrete descriptions of 2D quantum gravity, where "matter" models are coupled to the quantum fluctuations of the underlying 2D "space", represented in the discrete by the tessellations (see e.g. Ref.[40] for a review and more references). To each tessellation, we associate a statistical weight directly borrowed from the Einstein action in 2D, namely a weight $N^{(\chi)} g^A$ where χ and A are respectively the Euler characteristic and area of the tessellation (respectively measured via $\chi = \# \text{ faces} - \# \text{ edges} + \# \text{ vertices}$ and $A = \# \text{ faces}$ or vertices), and where N and g are the discrete counterparts of the Newton constant and cosmological constant. For each tessellation together with a matter configuration, realized for instance via a set of spins f on, we also have a weight $e^{-E(f,g)}$ for some energy functional E . We also make the standard choice of dividing the resulting weight by the order $|\text{Aut}(\cdot; f, g)|$ of the automorphism group of the tessellation together with its spin configuration. This leads for instance to the discretized partition function of any 2D statistical lattice model coupled to 2D quantum gravity

$$Z = \sum_{\text{tessel:}} N^{(\chi)} g^A \sum_{f, g} e^{-E(f, g)} = |\text{Aut}(\cdot; f, g)| \quad (7.1)$$

Note that the parameter N allows to isolate the contributions of tessellations of fixed genus. In the following we will be mainly interested in the genus zero contributions, obtained by letting $N \rightarrow 1$. Note also that the "free energy" $F = \text{Log } Z$ selects only the connected tessellations in the sum (7.1).

Like in the fixed lattice case, we are interested in the thermodynamic limit of the system, in which say the average area or some related quantity diverges, ensuring that the dominant contributions to Z come from large tessellations. This is guaranteed in general by the existence of a critical value g_c of the cosmological constant g at which such divergences take place. This value is a priori a function of the type of random lattices we sum over as well as of the various matter parameters. We may now attain interesting critical points by also letting the matter parameters approach critical values, a priori distinct from those on fixed lattices. The result is well described by the coupling of the corresponding CFT's with

quantum fluctuations of space, namely by letting the metric of the underlying 2D space fluctuate. Such fluctuations may be represented in the conformal gauge by yet another field theory, the Liouville field theory, which is coupled to the matter CFT. This field theoretical setting allows for a complete understanding of the various critical exponents occurring at these critical points [42]. For instance, one defines the (genus zero) string susceptibility exponent γ_{str} as the exponent associated to the cosmological constant singularity, namely by writing the singularity of the free energy as

$$F_{sing} / (g_c - g)^2 \sim \gamma_{str} \quad (7.2)$$

In the case of coupling of a matter theory with central charge c to 2D QG, one has the exact relation [42]

$$\gamma_{str} = \gamma_{str}(c) = \frac{c-1}{12} \frac{P_{(1-c)(25-c)}}{(1-c)(25-c)} \quad (7.3)$$

In the case of "pure gravity", namely when the matter is trivial and has $c = 0$, we get $\gamma_{str} = 1/2$, while for the critical Ising model with $c = 1/2$ we have $\gamma_{str} = 1/3$.

Upon coupling to gravity the spinless operators of the CFT $(h(z; z))$ get "dressed" by gravity $(h! \sim h)$ and acquire dressed dimensions, given similarly by [42]

$$= \frac{P_{\frac{1}{c+24h}}}{P_{\frac{1}{25-c}}} \frac{P_{\frac{1}{c}}}{P_{\frac{1}{c}}} \quad (7.4)$$

As opposed to the fixed lattice case, where conformal dimensions govern the fall-off of correlation functions of operators with distance, the dressed operators of quantum gravity do not involve distances, as their position is integrated over the surfaces, but rather only involve changes of area at fixed genus. More precisely the general genus zero correlators behave in the vicinity of g_c [42] as

$$h_1 \dots h_k \sim (g_c - g)^{2\gamma_{str} + \sum_{i=1}^k (h_i - 1)} \quad (7.5)$$

These results may be easily translated into the large (but fixed) area A behavior of the various thermodynamic quantities, upon performing a Laplace transform, which selects the coefficient of g^A in the various expansions. Let F_A denote the partition function for connected tessellations of genus zero and area A , we have

$$F_A \sim \frac{g_c^A}{A^{3\gamma_{str}}} \quad (7.6)$$

while if $h_{i_1 \dots i_k}$ denotes any genus zero correlator at fixed area, we have

$$h_{i_1 i_2 \dots i_k} = \frac{g_c^A}{A^{3 + \sum_{i=1}^k (i-1)}} \quad (7.7)$$

In Ref.[42], all these formulas were also generalized to higher genus as well. Note that Eqs.(7.3) and (7.4) are valid only as long as $c \leq 1$. This corresponds to the famous " $c = 1$ barrier" beyond which the gravitational system degenerates into infinitely branched structures (branched polymer phase of 2D QG).

As an illustration of Eq.(7.6), recall that the number of Eulerian triangulations of the sphere with A triangular tiles and with a marked edge reads from Eq.(6.14)

$$N_A = \frac{3}{2} 2^{A-2} \frac{(A-2)!}{(A-2)!(A-2)!} \quad \text{with } \frac{g_c^A}{A^{3+2(A-1)}} \quad (7.8)$$

with $A = 2s$ the number of triangles. Noting that the rooting simply amounts to $N_A / A F_A$, hence the asymptotics (7.8) correspond to $g_c = 1/8$ and $\gamma_{\text{str}} = 1/2$, hence $c = 0$ according to (7.3). This is one of the various examples where we attain the universality class of pure gravity, namely by summing over some bare tessellations without matter on them.

The asymptotic enumeration for most combinatorial problems involving planar (or more generally fixed genus) graphs is encoded in Eqs.(7.6) and (7.7) or their higher genus generalizations. This allows to predict the corresponding configurational exponents provided one is able to identify the central charge c of the underlying CFT. This latter step however may prove to be quite involved. In fact, a lesson of the forthcoming Section is that the naive application of these formulas may lead to wrong results for statistical models whose definition strongly relies on the structure of the underlying (whether fixed or random) lattice. This is precisely the case for the problems of folding or of fully packed loops that we are interested in.

8. One-avor fully packed loops

8.1. Fully packed loops on random trivalent graphs

We now come to the random version of the FPL(n) model, i.e. to a gas of fully packed loops on random planar trivalent graphs (dual to random triangulations). The most natural version consists in summing over all planar trivalent graphs. A typical, connected

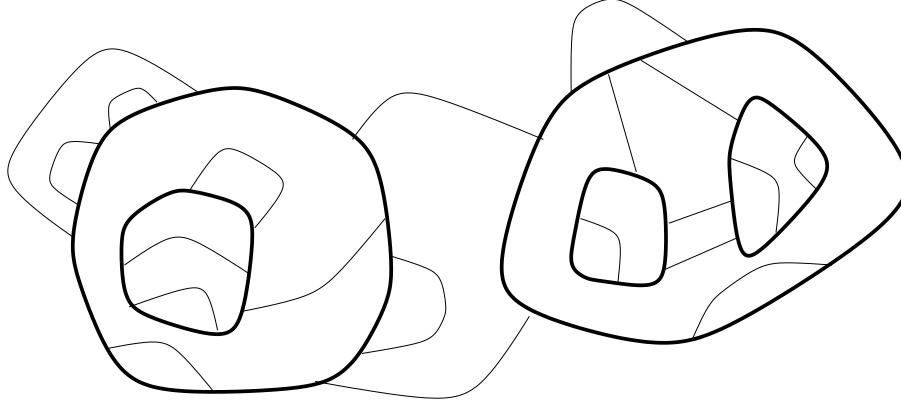


Fig. 28: An example of configuration of fully packed loops on a random planar trivalent graph.

configuration of this model is represented in Fig. 28. It is made of a set of disjoint or nested loops, each with a weight n , linked together by non-crossing arches, corresponding to the links not visited by loops.

The partition function Z_s of the model, which counts the number of configurations with $2s$ nodes behaves as

$$Z_s = C \frac{R^s}{s^3} \quad (8.1)$$

where C , R and β depend on n . The value of β was obtained exactly by matrix integral techniques (see Ref. [52]) with the result

$$\beta = \frac{e}{1-e} \quad n = 2 \cos(\beta); \quad 0 \leq \beta \leq \pi \quad (8.2)$$

We may also consider the partition sum $h_{1,1}$ counting FPL(n) configurations in the presence of two marked points connected by l open lines. The latter is characterized by a configurational exponent $\gamma_1(n)$ through $h_{1,1} \sim R^s s^{\gamma_1(n)}$, with the result [53]

$$\gamma_1(n) = 1 + \frac{1}{2} \quad (8.3)$$

independently of n .

As an illustration, a particularly interesting case is that of $n \rightarrow 0$ for which configurations have only one loop. This case therefore describes the problem of enumeration of Hamiltonian cycles, i.e. closed loops passing through all the nodes of the random trivalent graph [10]. If we open the loop at any of the $2s$ visited links and stretch it into an infinite oriented line as in Fig. 29, we simply obtain a configuration with $2s$ nodes on the line

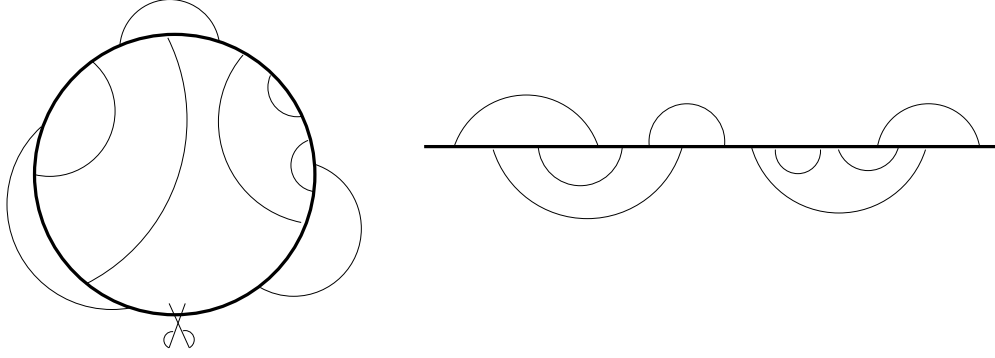


Fig.29: An example of oriented Hamiltonian cycle on a planar random trivalent graph (left). By cutting the link and stretching the loop into an oriented infinite straight line, one obtains a system of arches on top and below the line (right).

connected by pairs via a set of, say k non-intersecting arches in the upper half plane and $s - k$ in the lower half plane. We deduce that [54]

$$2sZ_s = \sum_{k=0}^{2s} \frac{X^s}{2k} C_k C_{n-k} = C_s C_{s+1} - \frac{4}{s^3} 16^s \quad (8.4)$$

where the Catalan number $C_s = (2s)! / (s!(s+1)!)$ counts the number of possible configurations of s non-intersecting arches. One thus finds an exponent $\beta = 1$, which is compatible with Eq.(8.2) for $n = 0$ ($\nu = 1/2$).

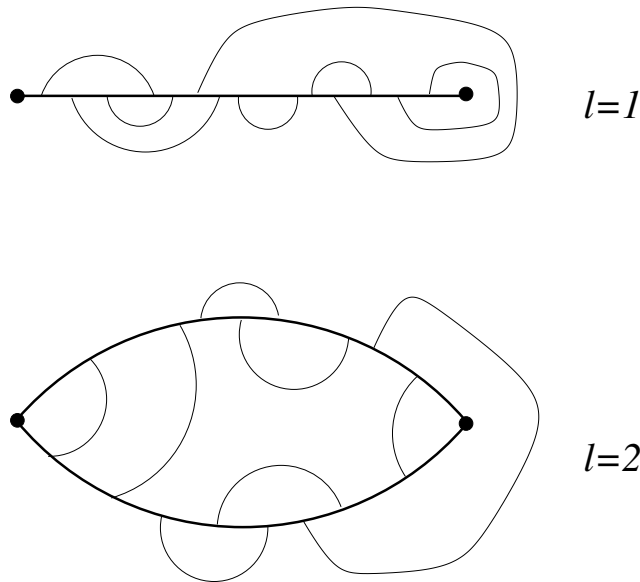


Fig.30: Examples of configurations with two marked points connected by l open lines, for $l=1$ (top) and $l=2$ (bottom)

We may similarly count configurations with two marked points connected by l open lines. For instance, the case $l = 1$ corresponds to having a segment dressed by arches (see Fig.30). The number of such configurations with $2s$ trivalent nodes is clearly given by $2^{2s} C_s = 16^s s^{3-2}$, in agreement with Eq.(8.3) for $l = 1$. Similarly, for $l = 2$, one describes configurations of a Hamiltonian cycle with two marked links (see Fig.30), in number $4s^2 Z_s = 16^s s^2$, in agreement with Eq.(8.3) for $l = 2$.

By inverting the relation (7.3), we see that the value (8.2) of γ is compatible with a central charge $c = c_{\text{dense}}(n) = 1 - 6e^2 = (1 - e)$. Similarly, by using Eq.(7.7) with $k = 2$, i.e. $\gamma_1(n) = 1 + 2\gamma_1$, and by inverting the relation (7.4), one finds that the result (8.3) for $\gamma_1(n)$ is compatible with a conformal dimension $2h = x_1(n)$ as given by Eq.(5.12). To conclude, the model FPL(n) defined on arbitrary random trivalent graphs corresponds to the coupling to gravity of a conformal theory of central charge $c_{\text{dense}}(n)$ as if the loops were not fully packed, a result further confirmed by the identification of the spectrum of dimensions $x_1(n)$. Naively, we would have expected a central charge equal to that, $c_{\text{fully packed}}(n)$, of the FPL(n) model on a regular lattice. In other words, we do not observe here the phenomenon $c \neq c + 1$ which we found for the regular lattice when passing from dense loops to fully packed loops.

The explanation for this clearly comes from the strong coupling of the matter model to the symmetries of its underlying space. For instance, fully packed loops on the regular lattice all have even length, a necessary condition for viewing them as the BC loops of some ABC tricoloring. We can therefore consider a slightly constrained model in which we impose that loops be of even length on the random lattice. It was shown however [50] that the $O(n)$ model with loops of even length on random graphs is in the universality class of the $O(n=2)$ model. This does not lead to the desired $c \neq c + 1$ phenomenon. As we shall see just below, we need to apply a much more drastic constraint by reducing the class of random graphs itself in order to recover the desired central charge $c_{\text{fully packed}}(n)$ of the regular case.

8.2. Fully packed loops on random trivalent bipartite graphs

On the regular lattice, the central charge $c = 2$ of the FPL(2) model as opposed to $c = 1$ for the $O(2)$ model had a simple geometrical interpretation, as describing the 2 degrees of freedom of the 2d positions of nodes for the equivalent 2d folding problem of the triangular lattice. On the other hand, we also observed that this 2d folding picture could be extended to the case of random triangulations provided we restricted their class

to the Eulerian ones. Indeed the latter are precisely the triangulations foldable onto the plane. In the dual language of trivalent graphs, this condition amounts to requiring that the graph be bipartite, i.e. may be node bicolored. Beside the folding interpretation, we also noticed in the Coulomb gas approach of Section 5.1 that the rules for defining a two-dimensional height use explicitly the bipartite nature of the hexagonal lattice (see Fig.20). We therefore expect this bipartite nature to be also crucial in the random case.

In this Section, we concentrate on the two cases $n = 0$ and $n = 1$ for which we show that the FPL(n) model, when defined on trivalent node-bicolored graphs, does indeed have the "increased" central charge $c_{\text{fully packed}}(n) = c_{\text{dense}}(n) + 1$ as given by Eq.(5.10). In the case $n = 0$, this translates into a remarkable irrational critical exponent for a very simple apparently harmless combinatorial problem.

For $n = 0$, the FPL(0) model describes the configurations of a Hamiltonian cycle, i.e. a single loop visiting all the nodes of the random bicolored trivalent graph (or equivalently visiting all faces of the Eulerian triangulation). We would like to compute the number Z_s^E of such configurations with $2s$ trivalent nodes.

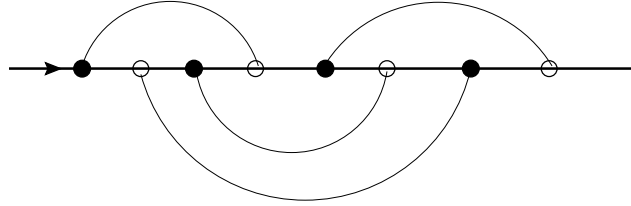


Fig.31: An example of configuration of arches around a line obtained by cutting the Hamiltonian cycle. The white and black nodes alternate along the line. Each arch connects a white node to a black one.

Once again we may open the Hamiltonian cycle at any of its $2s$ links so as to build an oriented line containing all the original nodes, together with a system of arches connected them by pairs either in the upper- or lower-half plane delimited by the line (see Fig.31). Comparing this situation with that of previous Section, we now have two additional constraints:

- (i) the colors of the nodes along the line alternate between black and white;
- (ii) each arch connects nodes of opposite colors.

This combinatorial problem, although extremely simply stated, is still open. We can however estimate the configuration exponent of the problem with reasonable accuracy by direct enumeration for small enough sizes s . A first approach, explained in Ref.[11],

consists in first building the two systems of arches on top and below the line and to count the number of ways to interlock them so that the black and white nodes alternate. A second approach consists in using a transfer matrix to generate the systems of arches from left to right. A similar technique will be discussed in detail in part D devoted to meanders.

The first values of sZ_s^E for $s = 1; 2; \dots; 22$ are given in the table below :

1	2
2	8
3	40
4	228
5	1424
6	9520
7	67064
8	492292
9	3735112
10	29114128
11	232077344
12	1885195276
13	15562235264
14	130263211680
15	1103650297320
16	9450760284100
17	81696139565864
18	712188311673280
19	6255662512111248
20	55324571848957688
21	492328039660580784
22	4406003100524940624

We may easily extract from these data an estimate for the exponent γ (see Fig.32), namely $\gamma = 0.77(1)$. This value differs clearly from the value $\gamma = 1$ obtained in previous Section for non-Eulerian triangulations. Moreover, this new value is now compatible with a central charge $c = c_{\text{fully packed}}(0) = 1$, for which, according to (7.3), γ reads

$$\gamma = \frac{1 + \sqrt[13]{13}}{6} \approx 0.76759 \quad (8.5)$$

More precisely, by inverting the relation (7.3), our estimate for γ yields a central charge $c = 1 - 0.05$. This leaves not much doubt on the fact that $c = c_{\text{fully packed}}(0) = 1$ as expected. As a consequence, we predict that our simple combinatorial problem displays a quite remarkable irrational configuration exponent, given by Eq.(8.5).

We now turn to the case of the FPL(1) model on node-bicolored trivalent random graphs, discussed in Ref.[12]. For $n = 1$, and only at this value, the connectivity of the loops plays no role and allows for local transformations. Let us orient all the links toward their adjacent black node. By contracting into a single tetravalent node each pair

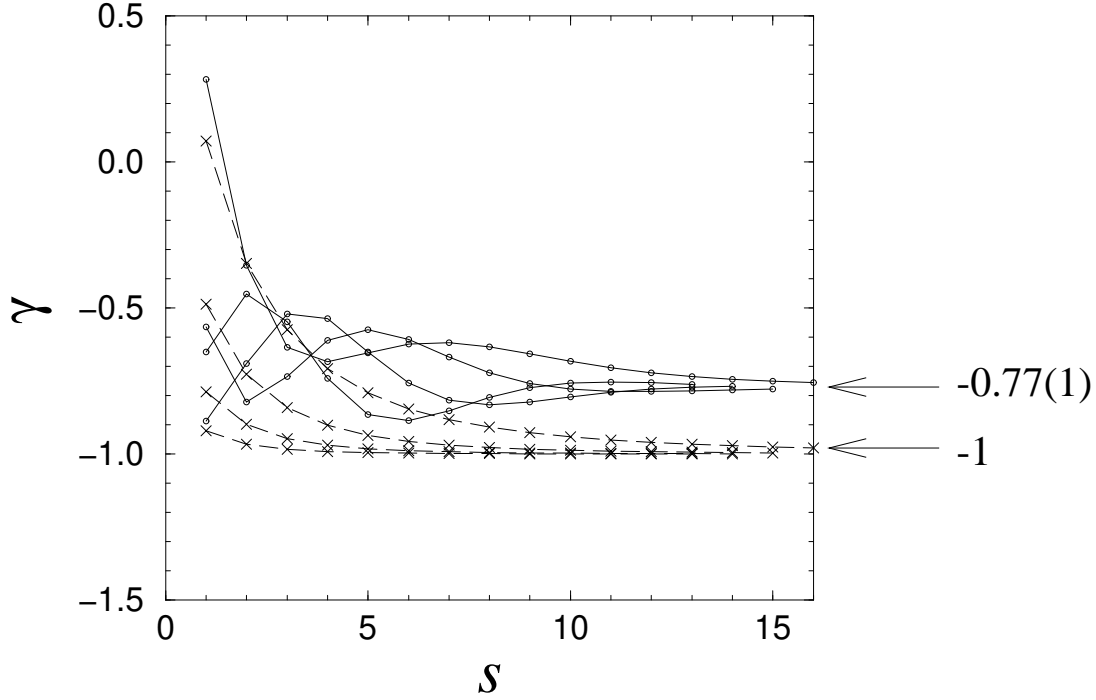


Fig.32: Estimates of γ extracted from the exact enumeration for sZ_s^E (see table) in the Eulerian (o) case and from $2sZ_s = c_s c_{s+1}$ in the non Eulerian case (x). The x-axis coordinate corresponds to the minimal value of s used in the determination. The different curves correspond to successive iterations of the convergence algorithm used (see Ref.[11]). The value of γ , equal to -1 in the non Eulerian case, is equal to -0.77(1) in the Eulerian case.

of trivalent nodes separated by an unvisited link, we end up with a tetravalent graph with oriented links. Moreover the orientations obey the so-called ice-rule of the six-vertex model, namely that each node have exactly two ingoing and two outgoing arrows (see Fig.33). More precisely, the two ingoing arrows must be consecutive around the node, which corresponds to the particular point of the six-vertex model where one of the weights (w_3) is zero (see Fig.33). The six-vertex model was solved by use of matrix integrals in Ref.[55], where it was shown on one hand that the $w_3 = 0$ point corresponds to a critical point, and on the other hand that the latter is described by the coupling to gravity of a particular CFT with central charge $c = 1$. This corresponds precisely to the expected result $c = c_{\text{fully packed}}(n = 1) = 1$.

To conclude this part, the above analysis of the cases $n = 0$ and $n = 1$ suggests that the specific universality class of fully packed loops observed on the regular lattice is preserved provided we impose the bicolability of the underlying trivalent graph, i.e. the Eulerian nature of the dual random triangulation. Summing over such triangulations will be called

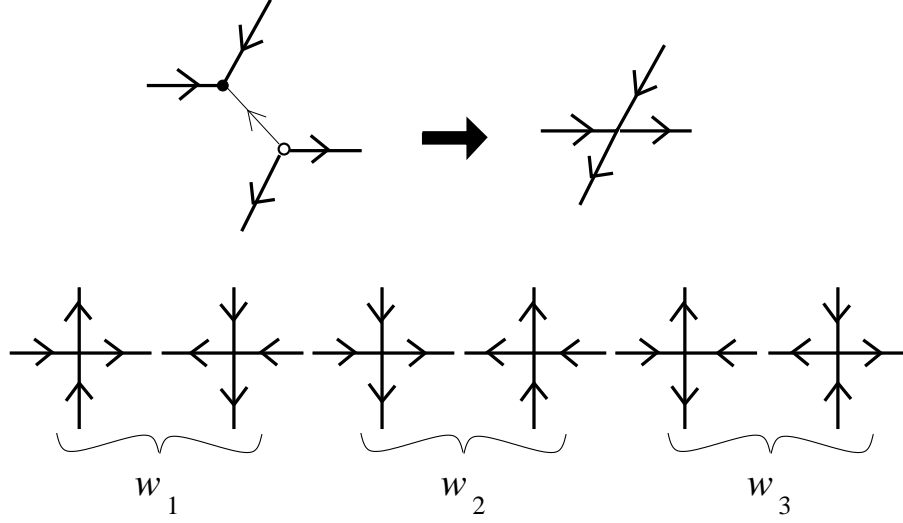


Fig.33: Mapping of the FPL(1) model on node-bicolored trivalent graphs onto a particular point of the gravitational six-vertex model on random tetraivalent graphs. Top: orienting all links toward black nodes and contracting unvisited links, we obtain tetraivalent nodes with two consecutive ingoing and two consecutive outgoing arrows. Bottom : the six local environments of the "six-vertex model" and their respective weights on the regular square lattice. Once defined on a random tetraivalent graph, the first two pairs of environments are indistinguishable, hence we must set $w_1 = w_2$. The constraint of having two consecutive ingoing arrows imposes $w_3 = 0$.

Eulerian gravity for obvious reasons. Now we may define two possible "gravitational" models of fully packed loops on random trivalent graphs.

We may sum over arbitrary trivalent graphs. As the dual triangulation will in general not be Eulerian, it will not be foldable, and the extra degree of freedom will be lost. The string susceptibility of the corresponding gravitational model will be computed using Eq.(7.3) with the dense central charge

$$\text{ordinary gravity : } c = 1 - 6 \frac{e^2}{1 - e}; \quad n = 2 \cos e \quad (8:6)$$

We may sum over bipartite trivalent graphs, whose dual triangulation is automatically foldable, thus preserving the height variable in \mathbb{R}^2 . The string susceptibility must be computed using Eq.(7.3) with the fully packed central charge

$$\text{Eulerian gravity : } c = 2 - 6 \frac{e^2}{1 - e}; \quad n = 2 \cos e \quad (8:7)$$

In the case $n = 2$ describing the 2d folding of (foldable) random triangulations, we expect a CFT with central charge $c_{\text{fully packed}}(2) = 2$ whose coupling to gravity would lead us

beyond the above-mentioned $c = 1$ barrier above which the relation (7.3) no longer applies. On heuristic grounds, we expect that the statistics of folding should be dominated by configurations where the folded surface degenerates into a highly branched one-dimensional structure. A confirmation of this image would require solving the simultaneous tricoloring of both nodes and links of random triangulations, an open question.

PART D : MEANDERS

This part is devoted to the study of meanders, also equivalent to self-avoiding folding configurations of a one-dimensional lattice. Beyond exact results for meander-related problems, we present a random-lattice fully packed loop description of the problem leading to precise predictions for the asymptotics of various meandric numbers. These predictions are tested numerically with remarkable agreement. A lesson of this study is the equivalence between the 1D self-avoiding folding and the 2D phantom folding of random foldable but non-unfoldable quadrangulations.

9. 1D self-avoiding folding: Meanders

The study of previous Sections was limited to phantom folding problems, with lattices made of interpenetrable cells. In particular, we concentrated on statistical models of folded states without any reference to an actual folding process in a possibly higher dimension. The question of self-avoidance, where we now prevent cells from interpenetrating one-another is extremely difficult. As we shall see now, even in the simplest 1D case, the problem is highly non-trivial and turns out to belong to the same class as the so-called meander problem, a notoriously difficult subject.

9.1. The meander problem

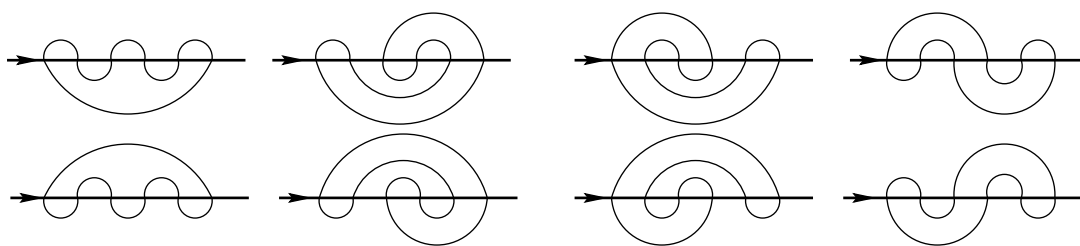


Fig.34: The $M_3 = 8$ configurations of meanders for $2n = 6$ bridges.

The problem of meanders is one of the combinatorial problems which, although very simply stated, still resist any attempt to an exact enumeration, would it be only for the asymptotics. The meander problem may be stated as follows: find the number M_n of topologically inequivalent configurations of a closed non-intersecting circuit crossing a river through $2n$ bridges. In this formulation, the river is assumed to be an infinite oriented

line. Note that, by closing the river into a loop and by opening and deforming the circuit into a line, the circuit and the river play symmetric roles. The denomination " m eanders" refers rather to the dual picture where the river meanders around the circuit but, for historical reasons, we shall work within the first formulation. For illustration, the figure 34 represents the $M_3 = 8$ configurations of m eanders with 6 bridges. In the following, we shall be mainly interested in the asymptotics of M_n for large numbers of bridges, as well as various generalizations.

9.2. M eanders as a 1D self-avoiding folding problem

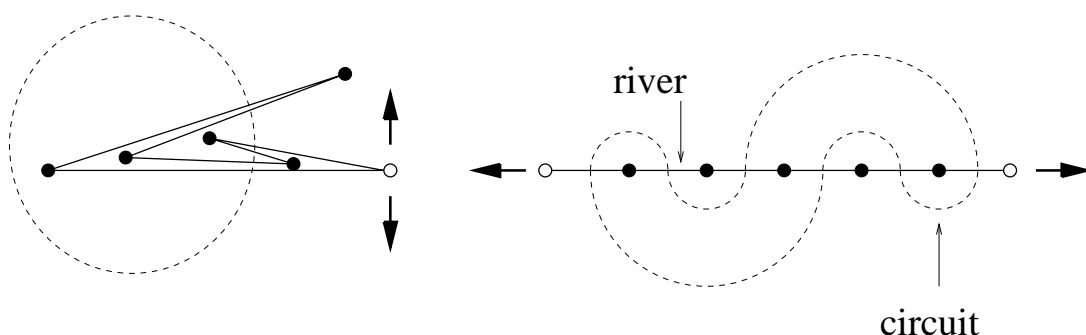


Fig.35: Correspondence between (left) the folding of a closed strip of $2n$ stamps and (right) a meander with $2n$ bridges. For clarity, the stamps are represented with different lengths and the folding is slightly undone.

The problem of m eanders is related to that of the self-avoiding folding of a closed chain of segments of unit length. Imagine for instance a strip of $2n$ post-stamps attached so as to form a loop. We want to count the distinct ways of maximally folding this strip on top of a single distinguished stamp. The main difficulty of the problem comes from the avoidance of the stamps which cannot interpenetrate one-another. Such a folding is represented on the left in Fig.35. We may now imagine piercing the stamps with a needle and a piece of thread and then knotting the thread into a loop (see Fig.35). Let us then open the strip at the level of the marked stamp and unfold it into a straight line (river), while the thread (circuit) meanders around it (see Fig.35). This transformation is clearly a one-to-one mapping between the 1D self-avoiding foldings of a closed chain of length $2n$ on top of one of its segments and m eanders with $2n$ bridges.

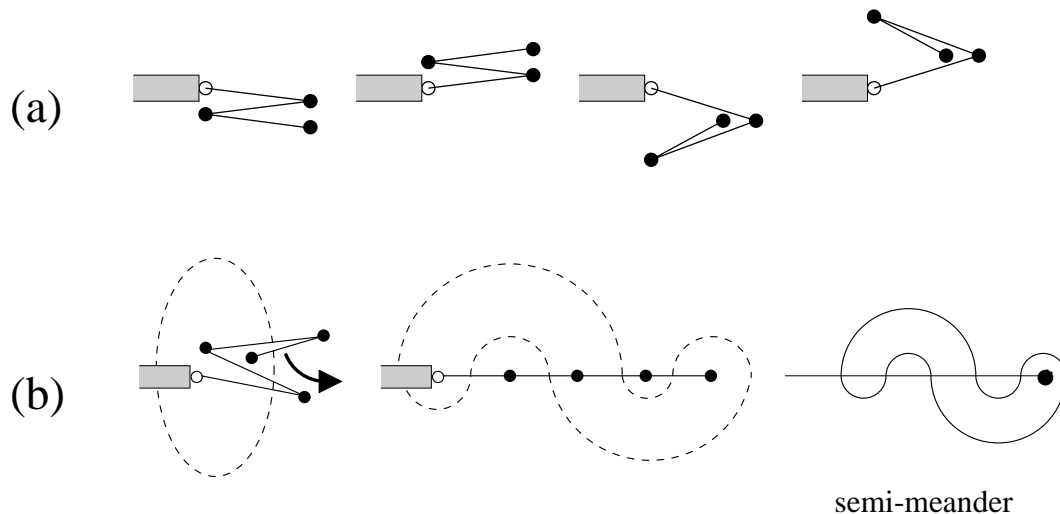


Fig.36: The four ways (a) of folding a strip of 3 stamps (here viewed from the side) on a single stamp. The transformation (b) of a compact folding of a strip of $n-1$ stamps (onto a single stamp) into a semi-meander with n bridges. The semi-meanders correspond to the case of a semi-infinite river with a source () around which the circuit may wind.

The same correspondence applies to the folding of an open chain of, say $n-1$ segments attached to a fixed support (see Fig.36-(a)). In this case, the transformation leads to what is called a semi-meander with n bridges (in correspondence with the $n-1$ segments and the support), i.e. a configuration of a closed non-intersecting circuit crossing a semi-infinite river (with a source) through n bridges. Note that in this case, the circuit may wind freely around the source. Both meanders and semi-meanders will be studied below in a unified framework.

9.3. A brief history of meanders

The meander problem is quite old. It is mentioned as early as 1891 under the name of "problème des timbres-poste" (post-stamp problem) by E. Lucas [56]. Later on, Sainte-Lague devotes a chapter of his book "Avec des nombres et des lignes: recreations mathematiques" (with numbers and lines: mathematical entertainments, 1937) [57]. Several combinatorial approaches of this problem are discussed in Refs.[58-60]. More recently, the problem re-appeared with the work of Arnold [61] in connection with the 16th Hilbert problem (the enumeration of ovals of algebraic planar curves). The modern formulation of

the problem, as just presented above, is due to Lando and Zvonkin [62], who also introduced the name "m eander". Let us finally mention that the m eander problem has many facets in relation with: mathematical problems such as the classification of 3-surfaces [63], computer science problems such as the study of planar permutations [64], or even artistic questions such as the description of mazes in Roman mosaics [65].

Despite a number of attempts, the problem is still unsolved to this day. The most important result of this part D is the prediction of a number of configurational exponents, all irrational, for m eanders and such.

10. Solvable cases

A number of exact results are known for variants of the m eander problem. These results rely on various descriptions using either direct combinatorics via arch statistics [13], explicit evaluations via matrix models [66] or algebraic formulations via the Temperley-Lieb algebra [14].

10.1. Generalization: multi-circuit m eanders

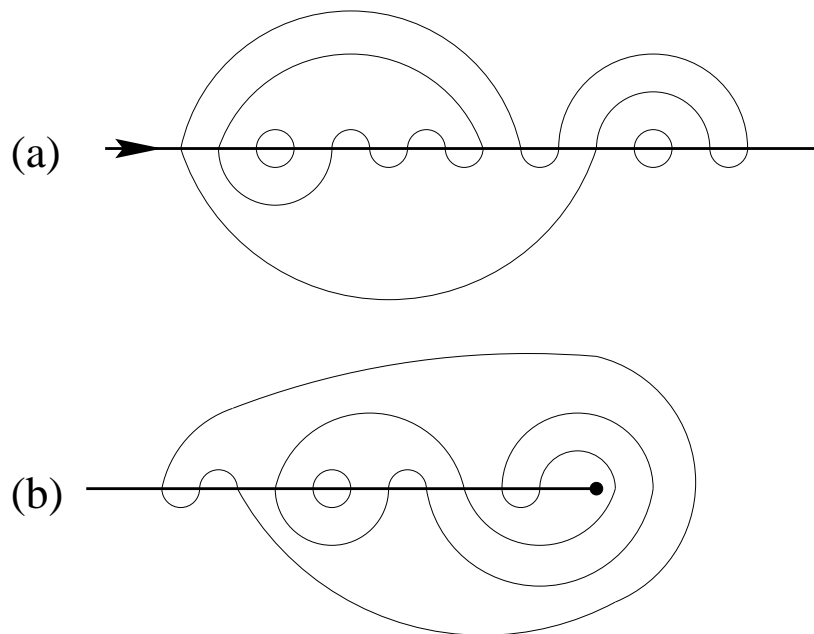


Fig.37: A typical m eander (a) with $2n = 16$ bridges and $k = 4$ circuits. A typical semi-m eander (b) with $n = 11$ bridges, $k = 3$ circuits and winding $w = 3$.

In the following, we consider the generalized case of meanders with k circuits still made of a single river but with a number k of non-intersecting, possibly interlocking, circuits. We shall denote by $M_n^{(k)}$ the number of topologically inequivalent configurations of k non-intersecting circuits which cross a river through a total number of $2n$ bridges, with clearly $k \leq n$ (we require that each circuit crosses the river). More simply, we shall refer to these configurations as meanders with $2n$ bridges and k circuits (see Fig.37). Similarly, we shall denote by $SM_n^{(k)}$ the number of semi-meanders with n bridges and k circuits corresponding to the case where the river is a semi-infinite line with a source around which the k circuits may wind (see Fig.37). Here again, one necessarily has $k \leq n$. With these definitions, the original problems of meanders and semi-meanders correspond to $k = 1$.

Instead of working at constant k , it is easier to let k vary and to introduce a weight q per circuit. One then defines the partition functions

$$\begin{aligned} M_n(q) &= \sum_{k=0}^n q^k M_n^{(k)} \\ SM_n(q) &= \sum_{k=0}^n q^k SM_n^{(k)} \end{aligned} \quad (10.1)$$

The original cases of meanders and semi-meanders can be recovered by considering the limit $q \rightarrow 0$ of $M_n(q) = q$ (resp. $SM_n(q) = q$).

For large n , we expect asymptotic behaviors of the form :

$$\begin{aligned} M_n(q) &\sim C(q) \frac{R(q)^{2n}}{n^{\gamma(q)}} \\ SM_n(q) &\sim C(q) \frac{R(q)^n}{n^{\gamma(q)}} \end{aligned} \quad (10.2)$$

where $\gamma(q)$ and $\gamma(q)$ are the configurational exponents. In the case of semi-meanders, we can also define the winding w as the depth of the source, namely the minimal number of circuit crossings in a path from the source to infinity (see Fig.37). We may then consider the average value of w for configurations with n bridges and a weight q per circuit. We expect the following behavior at large n :

$$\langle w \rangle_n(q) \sim n^{\gamma(q)} \quad (10.3)$$

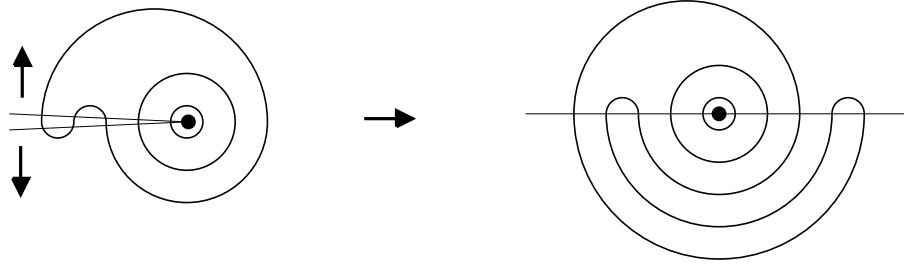


Fig.38: By opening the river, we transform any semi-meander with n bridges into a meander with $2n$ bridges. The opened circuits are completed by connecting diametrically opposite bridges via nested arches forming a rainbow, thus keeping track of their connectivity. The winding (here $w = 3$) corresponds to the number of arches above the middle point ().

with a winding exponent $0 \leq q \leq 1$. It is clear that n and w have the same parity and that meanders correspond to semi-meanders with $2n$ bridges and with a winding $w = 0$.

Note conversely that a semi-meander with n bridges may be viewed as a particular meander with $2n$ bridges by "opening" the river (see Fig.38), hence splitting each bridge in two. The connectivity of the loop is preserved by connecting the newly formed pairs of bridges via a "rainbow" of nested arches.

Two situations are a priori possible:

- (i) $q < 1$ and $R(q) = R(q)$. This case corresponds to a situation where the winding becomes negligible for large n and the entropy per bridge for meanders and semi-meanders is thus the same;

or:

- (ii) $q = 1$ and $R(q) < R(q)$. This case corresponds to a situation where the possibility of winding generates an extra configurational thermodynamic entropy per bridge.

We shall see in next Section that both situations (i) and (ii) actually occur, depending on the value of q .

10.2. Combinatorial solutions at $q = 1$, 1 and 1 : exact enumeration via arch statistics

The list of exactly known enumerations of multi-circuit meanders reduces to the three cases $q \neq 1$, $q = 1$ and $q = 1$. In all cases, the problem is reduced to that of arch statistics. A multi-circuit meander with $2n$ bridges may indeed be seen as the juxtaposition of two arbitrary systems of n arches, one on each side of the river, and connected at the bridges. Similarly, by opening the river (see Fig.38), any multi-circuit semi-meander is the juxtaposition of a system of n arches on one side and the particular system made of a rainbow of n nested arches on the other side.

The number of possible configurations of n non-intersecting arches is given by the celebrated Catalan numbers:

$$C_n = \frac{(2n)!}{n!(n+1)!} \quad (10:4)$$

In the case $q = 1$ where we ignore the number of circuits, we deduce that:

$$\begin{aligned} M_n(q=1) &= (C_n)^2 = \frac{1}{n^3} 4^{2n} \\ SM_n(q=1) &= C_n = \frac{1}{n^{\frac{3}{2}}} 4^n \end{aligned} \quad (10:5)$$

from which we get $R(1) = R(1) = 4$, $(1) = 3$ and $(1) = 3=2$. The winding number w corresponds to the number of arches passing above the source of the river (middle-point in Fig.38). Its average value is easily evaluated, with the asymptotic behavior:

$$\overline{w}_{1n}(q=1) = \frac{2}{n^{\frac{1}{2}}} \quad (10:6)$$

i.e. $(q=1) = 1=2$. This is a particular instance of the situation (i) of previous Section, in which the winding is negligible.

In the case $q \neq 1$, we have to maximize the number k of circuits for fixed n , i.e. take $k = n$. In the case of meanders, this amounts to requiring that the systems of arches above and below the river be identical up to reflection. Similarly, in the case of semi-meanders, the system of arches above the (opened) river must be made of n nested arches. By re-closing the river, this selects a unique configuration made of n nested circles winding around the source. This gives:

$$\begin{aligned} M_n(q) &\stackrel{q \neq 1}{=} C_n q^n = \frac{1}{n^{3=2}} (2^p \overline{q})^{2n} \\ SM_n(q) &\stackrel{q \neq 1}{=} q^n \end{aligned} \quad (10:7)$$

and thus $R(q) = 2^p \overline{q}$, $R(q) = q$, $(q) = 3=2$, $(q) = 0$. One has clearly $\overline{w}_{1n}(q) = n$ as the unique semi-meander with n circuits has winding n , and thus $(q) = 1$. This now corresponds to the situation (ii) described in previous Section. We shall see later how this $q \neq 1$ result may be taken as the starting point of a systematic $1=q$ expansion.

Finally, a last solvable situation concerns the case $q = 1$ for which one shows that

$$\begin{aligned} M_n(q=1) &= \begin{cases} 0 & n \text{ even} \\ (C_p)^2 & n = 2p+1 \end{cases} \\ SM_n(q=1) &= \begin{cases} 0 & n \text{ even} \\ C_p & n = 2p+1 \end{cases} \end{aligned} \quad (10:8)$$

This result may be proved by use of a simple involution for arches [13], or by a more technical supersymmetric matrix model approach [67].

We now address a generalization of the meander problem in which we allow for arbitrarily many rivers forming a set of nested or disjoint loops, crossed by arbitrarily many non-intersecting circuits, each with a weight q . We shall denote by $M_n(l; q)$ the generating function of the corresponding connected configurations with one of the rivers opened into a line.

$$Z_{1:\alpha}(\mathbf{N}; \mathbf{x}) = \frac{Z}{d\mathbf{W} d\mathbf{B}_1} \prod_{a=1}^A \text{Tr} \left[\frac{\mathbf{W}_a^2}{2} + \frac{\mathbf{P}_a^2}{2} \right] \times \prod_{a=1}^A \frac{(\mathbf{B}_a \mathbf{W}_a)^2}{2} \quad (10:9)$$
$$\begin{aligned} \text{white edges : } hW_{ij}W_{kl}i &= \frac{1}{N} i_l j_k = \begin{array}{c} \bullet \text{---} \rangle \text{---} \bullet \\ \bullet \text{---} \langle \text{---} \bullet \end{array} \\ \text{black edges : } h(B_a)_{ij}(B_b)_{kl}i &= \frac{1}{N} a_b i_l j_k = \begin{array}{c} \bullet \text{---} \rangle \text{---} \bullet \\ \bullet \text{---} \langle \text{---} \bullet \end{array} \end{aligned} \quad (10.10)$$
$$\text{Tr}(W B_a W B_a) =$$

(10:11)

73

Performing the Gaussian integration over all B_a matrices, we are then left with

$$Z_{1;q}(N; x) = \frac{\int dW e^{-N \text{Tr}(W^2=2)} \det(1 - xW - W^t)^{-q=2}}{\int dW e^{-N \text{Tr}(W^2=2)}} \quad (10:12)$$

This is just a Gaussian average over one Hermitian matrix W .

The critical singularity of the genus zero free energy $f = \lim_{N \rightarrow \infty} \frac{1}{N} \text{Log}(Z_{1;q}(N; x)) = N^{-2} (x(q) - x)^2$ is found [66] to lie at a critical value $x(q)$ given by

$$x(q) = \frac{e^2}{2 \sin^2(\frac{\pi}{2})} \quad (10:13)$$

where we have set $q = 2 \cos(\pi e) (0 < e < 1)$, while the corresponding critical exponent reads

$$= \frac{e}{1 - e} \quad (10:14)$$

This exponent is precisely that expected from the KPZ formula (7.3) for the coupling to 2D QG of the dense $O(q)$ model with central charge $c_{\text{dense}}(q) = 1 - 6e^2 = (1 - e)$ as given by Eq.(5.11). This shows that meander problems may be viewed as the coupling to gravity of particular critical loop models, and that the universality class of the present case coincides with that of the dense $O(q)$ loop gas.

The above results translate into the multi-river meander asymptotics

$$M_n(l; q) \sim \frac{R(l; q)^{2n}}{n^{-(l; q)}} \quad (10:15)$$

with

$$\begin{aligned} R(l; q) &= \frac{1}{x(q)} = 2 \frac{\sin^2(\frac{\pi}{2})}{e^2} \\ (l; q) &= \frac{2 - e}{1 - e} \end{aligned} \quad (10:16)$$

In particular, we recover from these values the case of meanders with arbitrarily many rivers and one single circuit by taking $q = 0, e = 1/2$, and $R(l; 0) = 4, (l; 0) = 3$. These values coincide with those of previous Section for one river and arbitrarily many circuits, as it should by river-circuit duality. We list a few of the values $R(l; q)$ and $(l; q)$ for various fractions e in the table below.

q	e	$R(1;q)$	$(1;q)$
0	$\frac{1}{2}$	4	3
1	$\frac{1}{3}$	$\frac{9}{2}$	$\frac{5}{2}$
$p\frac{1}{2}$	$\frac{1}{4}$	$16 \quad 8 \quad p\frac{1}{2} = 4:68:::$	$\frac{7}{3}$
$p\frac{1}{3}$	$\frac{1}{6}$	$36 \quad 18 \quad p\frac{1}{3} = 4:82:::$	$\frac{11}{5}$
2	0	$\frac{2}{2} = 4:93:::$	2

10.4. Meander determinant

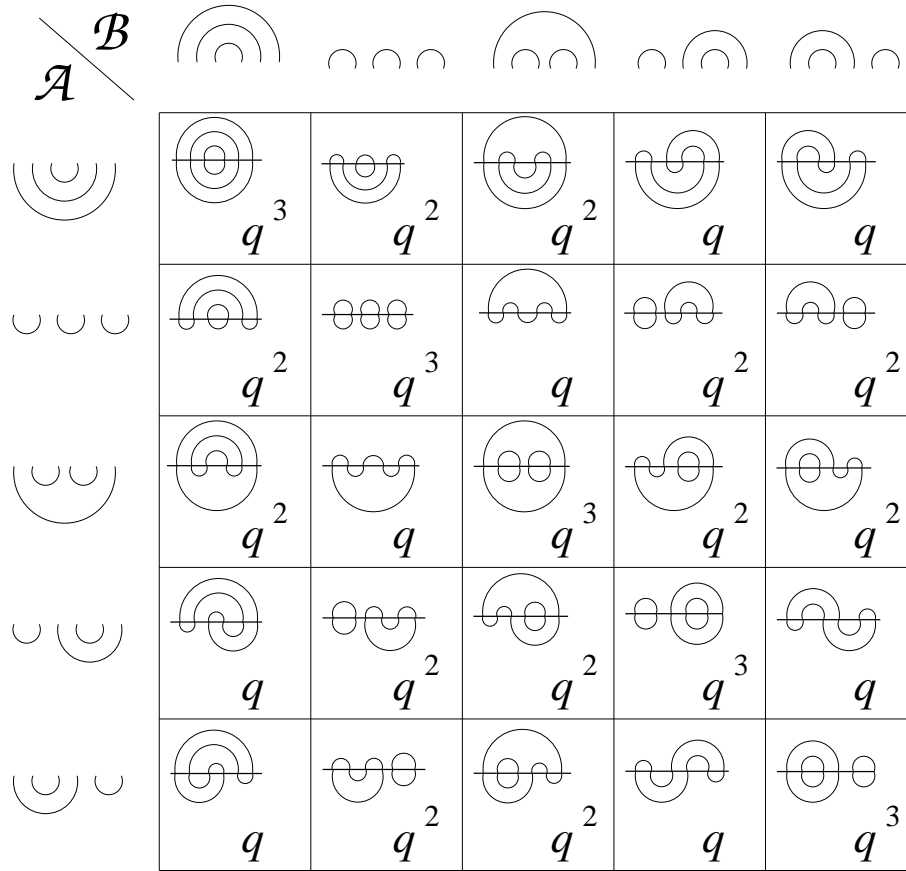


Fig.39: The $G_n(q)$ matrix (here for $n = 3, c_3 = 5$) obtained by juxtaposing all pairs $(A;B)$ of systems of n arches. The matrix element $G_n(q)_{A,B} = q^{c(A;B)}$ encodes the number of circuits $c(A;B)$ of the obtained meander.

Beyond the particular enumerations above, another exact result concerns the computation for any q of the meander determinant defined as follows. We have seen that any

m eander w ith $2n$ bridges (and w ith an arbitrary num ber of circuits) m ay be viewed as the juxtaposition of two system s of n arches, say A and B . By taking all pairs of system s of n arches, we de ne a sym m etric square m atrix $G_n(q)$ of size $c_n \times c_n$ whose elem ent $G_n(q)_{A;B}$, indexed by the pair $(A;B)$, is equal to

$$G_n(q)_{A;B} = q^{c(A;B)} \quad (10:17)$$

where $c(A;B)$ denotes the num ber of circuits of the m eander obtained by juxtaposing the arch system s A and B (see Fig.39). W e shall call "m eander determ inant" the determ inant of the m atrix $G_n(q)$. It is rem arkable that this determ inant m ay be com puted exactly, w ith the result [14]:

$$\det(G_n(q)) = \prod_{i=1}^n U_i(q)^{a_{n,i}} \quad (10:18)$$

$$a_{n,i} = \binom{2n}{n-i}^2 + \binom{2n}{n-i-1}^2 + \binom{2n}{n-i-2}^2$$

where the U_i 's are Chebyshev polynom ials de ned recursively as $U_{j+1}(q) = qU_j(q)U_{j-1}(q)$, $U_0(q) = 1$, $U_1(q) = q$. Equivalently, we have $U_j(2 \cos(\theta)) = \sin((j+1)\theta) = \sin(\theta)$, which leads to the equivalent form ula for the determ inant

$$\det(G_n(q)) = \prod_{i=1}^n q^{2 \cos \frac{1}{i+1}}^{a_{n,i}} \quad (10:19)$$

For instance, for $n = 3$, the determ inant of the m atrix $G_3(q)$ represented in Fig.39 is equal to $q^5 (q^2 - 1)^4 (q^2 - 2)$. The proof of the above form ulas in Ref.[14] m akes use of the intim ate link between the m eander problem and the Tem perley-Lieb algebra [68]. The equivalence between arch con gurations and reduced elem ents of the Tem perley-Lieb algebra $TL_n(q)$ goes as follow s. The Tem perley-Lieb algebra is expressed in its pictorial form , as acting on a "com b" of n strings, w ith the n generators $1, e_1, e_2, \dots, e_{n-1}$ de ned as

$$1 = \begin{array}{|c|} \hline \\ \hline \vdots \\ \hline \\ \hline \vdots \\ \hline \\ \hline \\ \hline \end{array} \begin{array}{l} 1 \\ i \\ i+1 \\ n \end{array} \quad e_i = \begin{array}{|c|} \hline \\ \hline \vdots \\ \hline \end{array} \begin{array}{l} i \\ i+1 \end{array} \quad (10:20)$$

The m ost general elem ent of $TL_n(q)$ is obtained by com posing the generators (10.20) like dominoes. The algebra is de ned through the follow ing relations between the generators

$$\begin{aligned} (i) \quad e_i^2 &= q e_i \quad i = 1; 2; \dots; n-1 \\ (ii) \quad [e_i; e_j] &= 0 \quad \text{if } |i-j| > 1 \\ (iii) \quad e_i e_{i-1} e_i &= e_i \quad i = 1; 2; \dots; n-1 \end{aligned} \quad (10:21)$$

The relation (ii) expresses the locality of the e 's, namely that the e 's commute whenever they involve distant strings. The relations (i) and (iii) read respectively

$$\begin{aligned}
 \text{(i)} \quad e_i^2 &= \text{diagram of a box with a central circle and two horizontal lines passing through it, with a vertical ellipsis above and below the circle, and a label 'i' to the right} \\
 \text{(iii)} \quad e_i e_{i+1} e_i &= \text{diagram of a box with a central crossing and two horizontal lines passing through it, with a vertical ellipsis above and below the crossing, and labels 'i' and 'i+1' to the right}
 \end{aligned}
 \tag{10.22}$$

In (i), we have replaced a closed loop by a factor q . Therefore we can think of q as being a weight per circuit of string. In (iii), we have simply "pulled the string" number $i+2$.

An element $e \in TL_n(q)$ is said to be reduced if all its strings have been pulled and all its loops removed, and if it is further normalized so as to read $\sum_{i \in I} e_i$ for some minimal finite set of indices I . A reduced element is formed of exactly n strings.

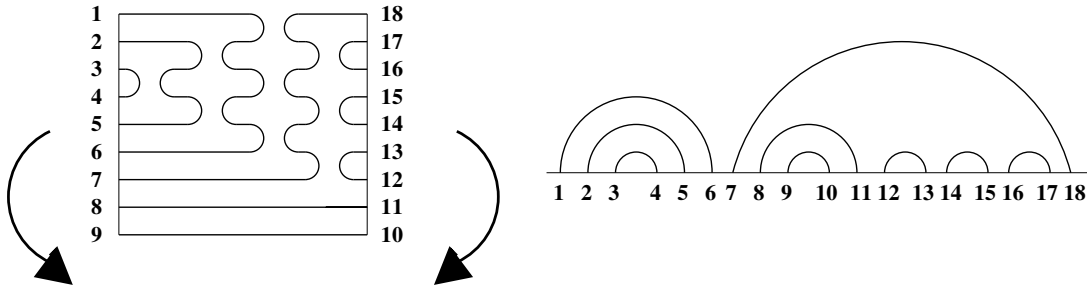


Fig.40: The transformation of a reduced element of $TL_9(q)$ into an arch configuration A of 9 arches. The reduced element reads $e_A = e_3 e_4 e_2 e_5 e_3 e_1 e_6 e_4 e_2$.

There is a bijection between the reduced elements of the Temperley-Lieb algebra $TL_n(q)$ and the arch configurations with n arches. Starting from a reduced element of $TL_n(q)$, we index the left ends of the n strings by $1; 2; \dots; n$, and the right ends of the strings $2n; 2n-1; \dots; n+1$ from top to bottom (see Fig.40 for an illustration). Interpreting these ends as bridges, and placing them on a line, we obtain a planar pairing of bridges by means of non-intersecting strings, equivalent to a configuration of n arches. Conversely, we can deform the arches of any arch configuration so as to form a reduced element of $TL_n(q)$. As a consequence, we have $\dim(TL_n(q)) = c_n$, as vector space with a basis formed by all the reduced elements.

In the language of the Temperley-Lieb algebra, the meander matrix $G_n(q)$ is precisely interpreted as the Gram matrix of the basis of reduced elements of $TL_n(q)$ (labeled by the corresponding arch configuration) with respect to the bilinear form $(e_A; e_B) = G_n(q)_{AB}$ of Eq.(10.17). The determinant of $G_n(q)$ is obtained as a by-product of the Gram-Schmidt orthogonalization of this matrix, readily performed by use of the representation theory of the Temperley-Lieb algebra [14].

The formula (10.18) may be extended to the more general case of meanders with open arches [69] or meanders based on the Hecke algebra [70].

11. Two-avor fully packed loops: exponents of the meander problem

11.1. Generalized meanders as random lattice loop models

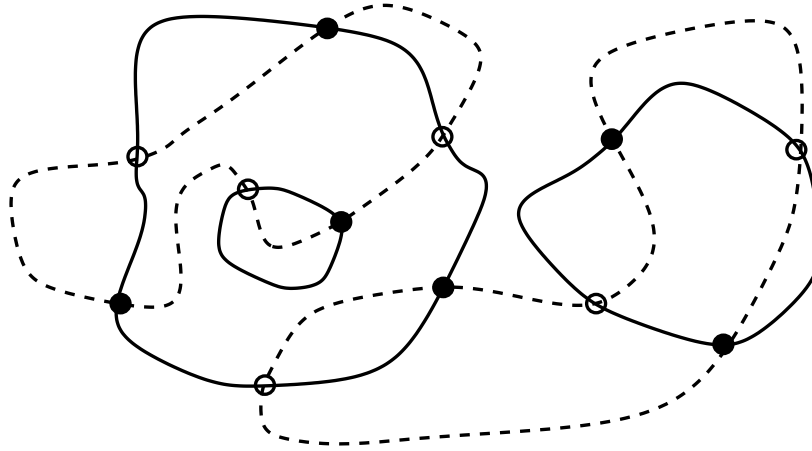


Fig.41: An example of generalized meander with three loops of river (solid lines) and two circuits (dashed lines). The obtained graph is automatically bipartite.

The most elaborate description of the meander problem consists in viewing it as the "gravitational" version (i.e. defined on random lattices) of a fully packed loop model. As in Section 10.3, we consider the general case of multi-river multi-circuit meanders (see Fig.41). We moreover attach a weight n_1 per loop of river and n_2 per circuit. The case of multi-circuit meanders with a single river of Section 10.1 corresponds to taking $n_1 \neq 0$, $n_2 = q$, while that of multi-river multi-circuit meanders of Section 10.3 amounts to taking $n_1 = 1$ and $n_2 = q$.

We may therefore rephrase the problem as that of enumerating the configurations of planar graphs made of a set of river loops and circuits with the constraints that:

- (a) The rivers are self- and mutually-avoiding;
- (b) The circuits are self- and mutually-avoiding;
- (c) A river and a circuit may cross at a "bridge" node;
- (d) The resulting graph is connected.

To avoid problems of symmetry factors, it is as usual convenient to consider configurations with a marked and oriented edge (say corresponding to a portion of river). The above model is therefore a model of fully packed loops on random tetravalent graphs whose nodes correspond to the bridges, with two types of loops (the rivers and the circuits) weighted by n_1 and n_2 respectively. We will denote this model by $\text{GFPL}^2(n_1; n_2)$ (for gravitational fully packed loops).

It is interesting to note that, as all nodes correspond to crossings of river loops and circuits, the corresponding tetravalent graphs are automatically bipartite, i.e. may have their nodes bicolored (see Fig.41).

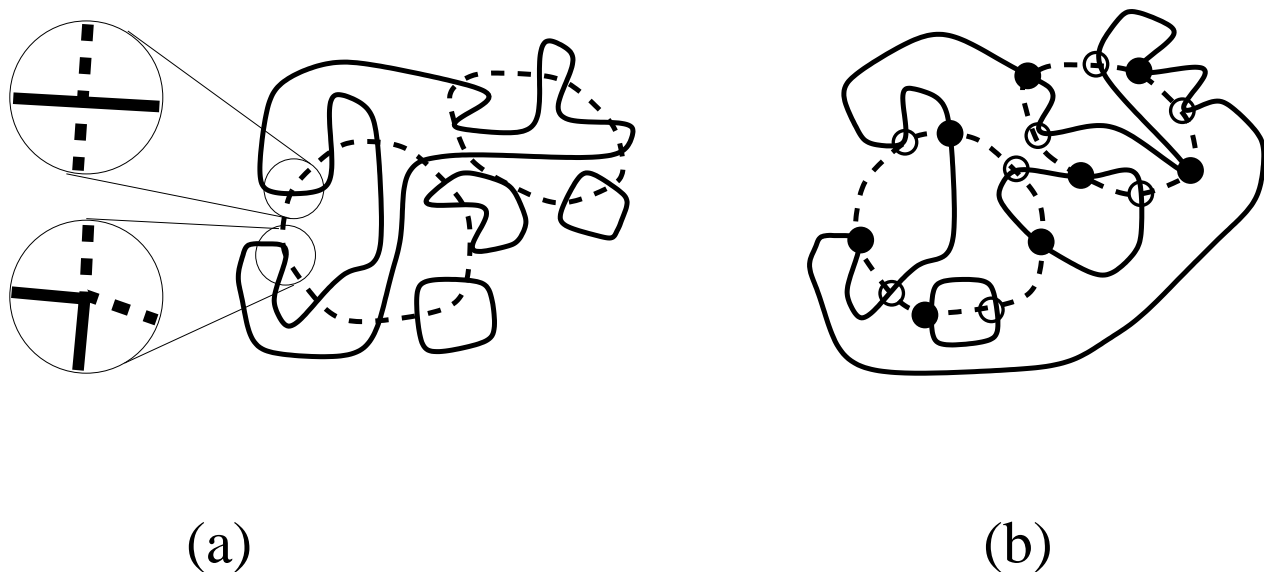


Fig.42: Examples of configurations of tangent meanders with two possible vertices, either the crossing of two loops, or a tangency point (contact without crossing). The underlying tetravalent graph may be arbitrary (a) or constrained to be bipartite (b).

By anticipating the coming discussion, we may introduce two other versions of the problem, which consist in allowing for the presence, in addition to the crossings, of tangency points at which a circuit and a river come in contact but do not cross (see Fig.42). We shall refer to this case as tangent meanders. The bicolability of the underlying graph is no longer ensured and, by analogy with the one-avor loop case of Section 8, we may

consider two different versions of the problem : the ordinary gravity version where we sum over all tetravalent graphs or the Eulerian gravity version where we restrict the summation to node-bicolored tetravalent graphs only.

11.2. The FPL^2 model on the square lattice

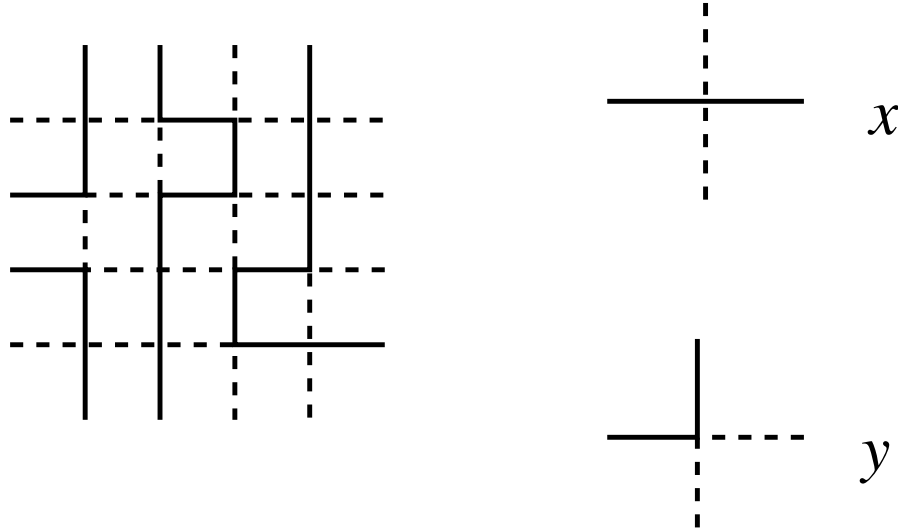


Fig.43: Example of configuration of the FPL^2 model. The black and white (here represented as dashed) loops may either cross or avoid each other. The two allowed vertices (up to rotations and symmetries) are represented on the right.

We now would like to interpret the $GFP L^2(n_1; n_2)$ model or its generalizations with tangency points as gravitational versions of models defined on the regular lattice. In the case of tetravalent graphs, the regular lattice to be considered is the square lattice. A natural candidate is the $FPL^2(n_1; n_2)$ model, introduced in Ref.[71], which consists of a gas involving two types of loops, say black and white, with respective weights n_1 and n_2 and the constraints that:

1. The loops are fully packed, i.e. each of the two systems of loops is self-avoiding and visits all the nodes of the lattice;
2. Each link is occupied by one type of loop only, the loops being in contact only at the nodes.

The $FPL^2(n_1; n_2)$ model allows for two types of vertices (up to rotations and symmetries), represented in Fig.43 and corresponding respectively to a crossing of the two types of loops (crossing vertex) or to a contact with mutual avoidance (tangent vertex). Very

generally, we may introduce different weights, say x and y respectively for the two types of vertices. The $\text{FPL}^2(n_1; n_2)$ model of Ref.[71] concerns the particular case where $x = y$.

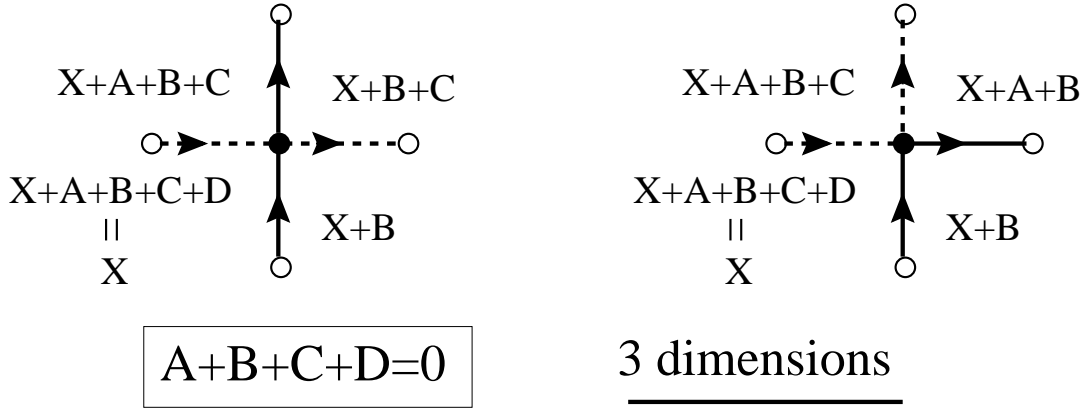
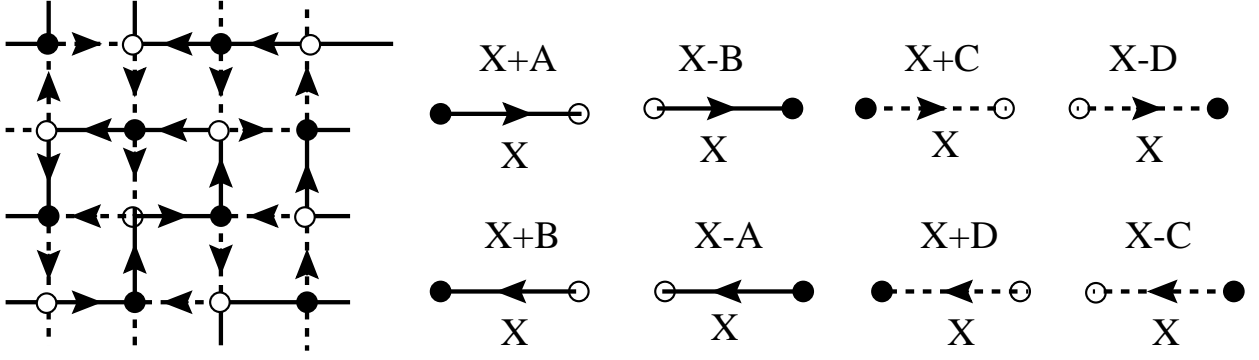
Before we study this model, let us note that the suppression of the tangent vertex ($y = 0$) leads to a quite trivial model on the square lattice since the only allowed loop configuration is that where the black "loops" occupy the horizontal links of the lattice and the white loops the vertical links (or conversely). Still, by taking $n_1 = n_2 = 2$, which amounts to orienting independently upwards or downwards each vertical (white) line and to the left or to the right each horizontal (black) line, the configurations that we obtain are in one-to-one correspondence with the foldings of the (dual) square lattice in $d = 2$, as studied in Section 1.1. The correspondence is simply that a vertical (resp. horizontal) line of the (dual) square lattice is folded if and only if the orientations of the two vertical (resp. horizontal) lines on each side are opposite. This remark, although elementary, prefigures the link between the $\text{GFPL}^2(2; 2)$ model and the folding of random quadrangulations. We will discuss this link more precisely in Section 13 below.

Let us now consider the $\text{FPL}^2(n_1; n_2)$ model with $x = y = 1$. This model was studied in Ref.[71] by Coulomb gas techniques similar to those presented in Section 5. Some properties could also be derived exactly by Bethe Ansatz [72,73], in the same spirit as in Section 4.

We start from the case $n_1 = n_2 = 2$, which amounts to considering oriented loops with no extra weight. The model is then equivalent to a four-color model with colors, say A, B, C and D on the links of the square lattice and the constraint that the four colors are present around each node. The links of color A or B (resp. C or D) form the black (resp. white) loops and alternate along these loops. The two possible choices for the alternation of colors correspond to the two orientations of the loop.

As in Section 3.3, we may transform the model into a model of heights X on the faces of the square lattice with the transition rules represented in Fig.44. We need a priori four height differences A, B (black loops) and C, D (white loops), with the constraint that $A + B + C + D = 0$ to ensure a well defined height on each face. The obtained height variable X is therefore three-dimensional and corresponds to a three-component scalar field theory with central charge 3 [71].

As in Section 5.2, the introduction of the weights n_1 and n_2 is performed by introducing vertex weights $\exp(-\epsilon_1/4)$ (resp. $\exp(-\epsilon_2/4)$) per left or right turn of the black



3 dimensions

Fig.44 : Definition of the heights X in the FPL^2 model. The definition uses the bipartite nature of the lattice. The consistency after one turn imposes the constraint $A + B + C + D = 0$. The height is therefore three-dimensional.

(resp. white) loops, with $n_1 = 2 \cos(\epsilon_1)$ and $n_2 = 2 \cos(\epsilon_2)$. For $0 < n_1, n_2 < 2$ ($0 < \epsilon_1, \epsilon_2 < \pi/2$), the theory is conformal with central charge [71]:

$$c_{FPL}(n_1; n_2) = 3 - 6 \frac{\epsilon_1^2}{1 - \epsilon_1} - 6 \frac{\epsilon_2^2}{1 - \epsilon_2} = 1 + c_{\text{dense}}(n_1) + c_{\text{dense}}(n_2) \quad (11.1)$$

with c_{dense} given by Eq.(5.11). One can also compute the exponents $x_{l,m}$ associated with the long distance behavior $r^{-2x_{l,m}}$ for the correlation of a set of l black lines and m white lines connecting two points at distance r , with the value [71]

$$\begin{aligned} x_{l,m}(n_1; n_2) = & \frac{1 - \epsilon_1}{8} l^2 - \frac{\epsilon_1^2}{2(1 - \epsilon_1)} (1 - l; 0) \\ & + \frac{1 - \epsilon_2}{8} m^2 - \frac{\epsilon_2^2}{2(1 - \epsilon_2)} (1 - m; 0) \\ & + \frac{1}{16} (l+m; \text{odd} + l; \text{odd} - m; \text{odd}) \frac{(1 - \epsilon_1)(1 - \epsilon_2)}{(1 - \epsilon_1) + (1 - \epsilon_2)} \end{aligned} \quad (11.2)$$

We may finally consider a "dense" version of the problem, denoted by $\text{DFPL}^2(n_1; n_2)$ (for densely packed loops) by allowing for the presence of sites not visited by black loops or white loops [74]. In terms of height, this requires to impose the additional constraint $A + B = 0 = C + D$, which leads to two-dimensional heights and reduces the central charge to a value

$$c_{\text{DFPL}}(n_1; n_2) = 2 - 6 \frac{e_1^2}{1 - e_1} - 6 \frac{e_2^2}{1 - e_2} = c_{\text{dense}}(n_1) + c_{\text{dense}}(n_2) \quad (11.3)$$

In this case, the exponents $x_{l,m}$ reduce to

$$\begin{aligned} x_{l,m}(n_1; n_2) &= \frac{1 - e_1}{8} l^2 - \frac{e_1^2}{2(1 - e_1)} (l - l_0) \\ &\quad + \frac{1 - e_2}{8} m^2 - \frac{e_2^2}{2(1 - e_2)} (m - m_0) \\ &= x_l(n_1) + x_m(n_2) \end{aligned} \quad (11.4)$$

with x_l given by Eq.(5.12).

11.3. Coupling $\text{DFPL}^2(n_1; n_2)$ to gravity: Effective field theory of meanders

The coupling of the $\text{DFPL}^2(n_1; n_2)$ model to gravity corresponds *stricto sensu* to the case of multi-river multi-circuit tangent meanders with the two types of vertices, namely crossings and tangencies. For Eulerian gravity, realized by summing only over node-bicolored tetravalent graphs, the three-dimensional degrees of freedom of the regular lattice model are preserved and the critical behavior of the model corresponds to the coupling to gravity of a CFT of central charge $c_{\text{DFPL}}(n_1; n_2)$, as given by Eq.(11.1). We may in particular use Eq.(7.3) to derive the configuration exponent governing the large n behavior $n^{-2n} = n^{-2n}$ of the number n of tangent meanders with one river line and one circuit meandering around it with $2n$ contact (crossing or tangency) points of alternating color along both circuit and river. This corresponds to taking $n_1; n_2 \rightarrow 0$, in which case $c_{\text{DFPL}}(0; 0) = -3$, leading to

$$= \frac{7 + \frac{p}{7}}{3} \quad (11.5)$$

This is not however the original meander problem we started with. To get the $\text{GFPL}^2(n_1; n_2)$ model, we have indeed to forbid tangency points. We shall now argue

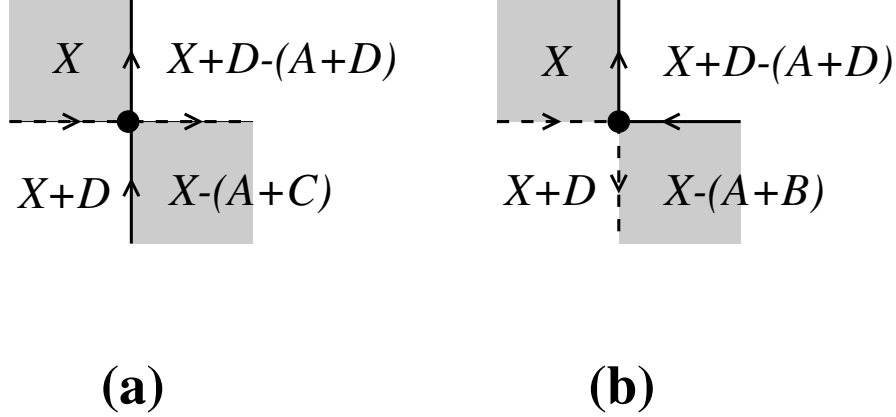


Fig.45: Typical height configurations around (a) a crossing vertex and (b) a tangency vertex. When going diagonally say from the NW to the SE face (shaded), the height increases by an amount restricted to $(A + C)$ or $(A + D)$ in the case (a) and only to $(A + B)$ in the case (b). Forbidding (b) will therefore amount to a reduction of the height variable range from 3 to 2 dimensions.

that tangency points are relevant and that their suppression reduces the value of the central charge. Assuming indeed that only crossing vertices are allowed, in which case the bicolorability of the nodes of the graph is automatic, we can still build a three-dimensional height as before. Note that the graph is also automatically face bicolorable (as is any tetravalent graph) and we may thus define a sub-lattice W of white faces and a sub-lattice B of black faces. It is then easy to see that the heights on two neighboring faces on the sub-lattice B , i.e. faces diametrically opposite around a node, may differ only by $(A + C)$ or $(A + D)$ (see Fig.45-(a)) but that the third direction $(A + B)$ never occurs (as opposed to what happens with the tangency vertex – see Fig.45-(b)). The heights of the sub-lattice B are de facto two-dimensional in the $(A + C; A + D)$ plane and the same is true for those of the sub-lattice W . It is therefore harmless to set $A + B = C + D = 0$, which takes us back to the $DP L^2$ model. This leads to the prediction [16] that the multi-river multi-circuit meander problem lies in the universality class of the $DP L^2(n_1; n_2)$ model, therefore a CFT with central charge

$$c_{\text{meander}}(n_1; n_2) = c_{DP L^2}(n_1; n_2) = c_{\text{dense}}(n_1) + c_{\text{dense}}(n_2) \quad (11:6)$$

The same conclusion may be reached by a different reasoning. Considering now tangent meanders on arbitrary tetravalent graphs (ordinary gravity version), we may still use the height transition rules of Fig.44 but we can no longer distinguish between A and B (resp. C and D), which equivalently amounts to imposing $A + B = 0 = C + D$ too.

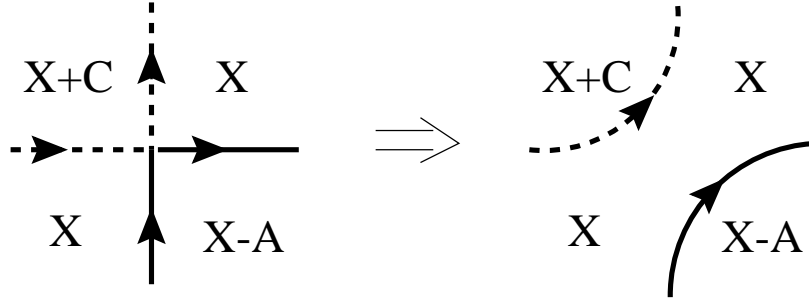


Fig.46: In the case of tangent meanders on arbitrary tetravalent graphs, the tangent vertices may be untied without affecting the heights.

This also leads to a two-dimensional height and we again have to use the reduced central charge c_{DPL} of Eq.(11.6). To interpret this central charge as that for meanders, we still have to show that tangency points are irrelevant for ordinary gravity as opposed to the case of Eulerian gravity. We may understand this phenomenon heuristically by noticing that, in the effective height language, any tangent vertex may be safely "untied" as shown in Fig.46 without modifying the heights.

To conclude, we have predicted in two different ways that meanders correspond to the coupling to gravity of a CFT with central charge given by Eq.(11.6). For the original problem of meanders with one river line and one circuit, this gives $c = 4$ and leads to a configuration exponent [16]

$$\langle 0 \rangle = 2 \quad \text{str} (4) = \frac{29 + \sqrt{145}}{12} \quad (11:7)$$

by use of Eq.(7.3).

11.4. More meander exponents

We have now identified the CFT underlying meanders, as the dense two-avor loop model with $n_1 = n_2 = 0$ coupled to ordinary gravity. The complete knowledge of the conformal operator content of this CFT via the Coulomb gas picture gives access to a host of meandric numbers which we describe now.

The important operators for our present purpose are those identified as creating oriented river vertices, namely the operators ϕ_k (resp. ψ_k), $k = 1; 2; \dots$ which correspond to the insertion of a k -valent source (resp. sink) vertex at which k oriented river edges

originate (resp. terminate). In the Coulomb gas picture, these operators create "magnetic" defect lines along which the height variable has discontinuities. The operator ϕ_k has conformal dimension [71]

$$h_k = \frac{x_{k;0}(0;0)}{2} = \frac{k^2 - 4}{32} \quad (11:8)$$

$k = 1; 2; \dots$, with x as in Eq.(11.4). When coupled to gravity, these operators get dressed (into ϕ_k) and acquire, according to Eq.(7.4), the dimension:

$$h_k = \frac{\frac{1}{2} \frac{p}{8+3k^2} \frac{p}{5}}{\frac{p}{29} \frac{p}{5}} \quad (11:9)$$

As a preliminary remark, we note that $h_2 = \frac{1}{2} = 0$. The operators ϕ_2 , ϕ_{-2} indeed correspond to the marking of an edge of the river in meanders, and moreover such operators must go by source/sink pairs for the orientations of the pieces of river connecting them to be compatible. Applying Eq.(7.7) to the two-point correlator $h_{-2} \phi_2 i_A$ at fixed large area $A = 2n$, we find

$$h_{-2} \phi_2 i_A = \frac{g_c^A}{A^{1-\text{str}}} \quad (11:10)$$

while the meander counterpart (with a closed river) behaves as $M_A = (2A)^{-\frac{1}{2}} g_c^A = (A^{3-\text{str}})^{-\frac{1}{2}}$. We see that the net effect of the insertion of the operators ϕ_2 is an overall factor proportional to A^{-2} / n^2 , which confirms their interpretation as marking operators.

We may now turn to the case of semi-meanders, for which the river is a semi-infinite line around the origin of which the road may freely wind. Considering the point at infinity on the river as just another point, the semi-meanders may equivalently be viewed as meanders whose river is made of a segment. Sending one of the ends of the segment to infinity just resolves the ambiguity of winding around either end. Using the above river insertion operators, we immediately identify the generating function for semi-meanders as

$$h_{-1} \phi_{-1} i = \sum_{n=1}^{\infty} SM_n g^n \quad (11:11)$$

Using again Eq.(7.7) and the explicit values of ϕ_{-1} via (11.9), we arrive at the large n asymptotics [16]

$$SM_n \frac{g_c^n}{n} = 1 + 2 \frac{1}{n} \frac{1}{\text{str}} = 1 + \frac{11}{24} \left(\frac{p}{5} + \frac{p}{29} \right) \quad (11:12)$$

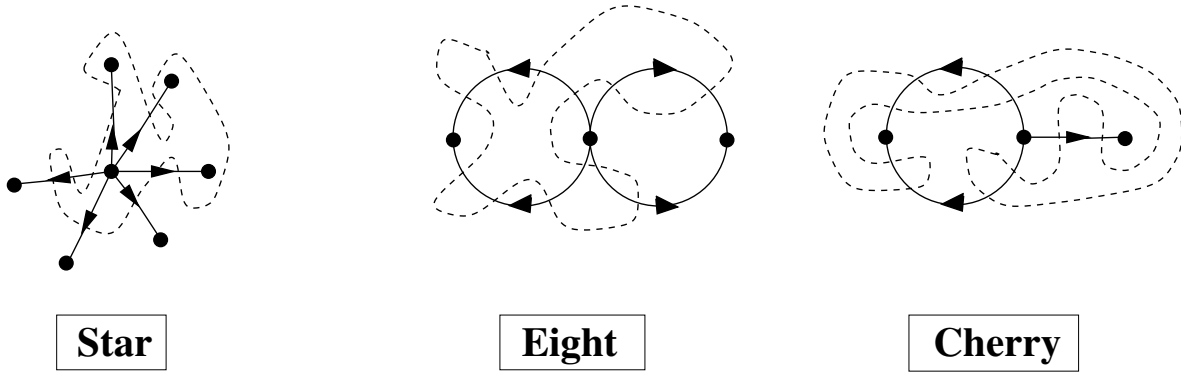


Fig.47: Three types of meandric configurations in which the river has the geometry of (a) a k -valent star (b) an "eight" (c) a "cherry". The vertices corresponding to river sinks or sources are represented by filled circles (\bullet). The edges of river in-between them are oriented accordingly. The road (dashed line) may freely wind around univalent vertices.

Note that we expect the value of g_c to be the same for meanders and semi-meanders, as both objects occur as thermodynamic quantities in the same effective field theory. In the language of Section 10.1, this means that we are in regime (i).

We may now generate many more meandric numbers by considering more general correlators. To name a few (all depicted in Fig.47), we may generate rivers with the geometry of a star with one k -valent source vertex and k univalent sink vertices generated by $h_k(\frac{1}{2})^k i$, rivers with the geometry of an "eight" with one tetravalent source vertex and two loops, each containing a bivalent sink vertex generated by $h_4(\frac{1}{2})^2 i$, or rivers with the geometry of a "cherry" with one trivalent source vertex, one univalent sink, and one loop, marked by a bivalent sink vertex generated by $h_3(\frac{1}{2})^2 i$, etc ... For each of these situations, we get the corresponding configuration exponent $\mathcal{P} = 3 + \sum_i (i-1)$ by applying Eq.(7.7) with the dimensions of Eq.(11.9). We get respectively [16]

$$\begin{aligned}
 \mathcal{P}_{\text{star}} &= \frac{1}{48} \left(\frac{1}{5} + \frac{1}{29} \right) \left(\frac{1}{3k^2 + 8} + k \left(\frac{1}{11} - 2 \frac{1}{29} \right) + 4 \frac{1}{29} - 2 \frac{1}{5} \right) \\
 \mathcal{P}_{\text{eight}} &= \frac{1}{24} \left(\frac{1}{5} + \frac{1}{29} \right) \left(\frac{1}{14} + \frac{1}{5} \right) \\
 \mathcal{P}_{\text{cherry}} &= \frac{1}{48} \left(\frac{1}{5} + \frac{1}{29} \right) \left(\frac{1}{11} + \frac{1}{35} \right)
 \end{aligned} \tag{11.13}$$

11.5. Multi-circuit meander exponents

More generally, we may consider the one-river multi-circuit case of Section 10.1 by taking $n_1 \neq 0$ and $n_2 = q$. Our predictions require moreover $0 \leq q \leq 2$ for the field

theoretical description to hold. Using similar argument as in previous Section, we predict a critical exponent $\gamma(q) = 2 - \gamma_{\text{str}}(c)$ with the central charge

$$C = C_{\text{meander}}(0; q) = 1 + 6 \frac{e^2}{1 - e}; \quad q = 2 \cos(e); \quad 0 \leq e \leq \frac{1}{2} \quad (11:14)$$

We arrive at

$$\gamma(q) = 2 + \frac{1 - e + 3e^2 + \frac{P}{(1 - e + 3e^2)(13 - 13e + 3e^2)}}{6(1 - e)} \quad q = 2 \cos(e) \quad (11:15)$$

Similarly, we can compute the exponent $\gamma(q)$ by inserting two defects corresponding to the two extremities of an open segment. This leads to the prediction $\gamma(q) = \gamma(q) - 1 + 2 - \gamma_1(q)$ with $\gamma_1(q)$ related to $h_1(q) = x_{1,0}(0; q) = 2$ of (11.4) through (7.4). We finally get [16]

$$\gamma(q) = 1 + \frac{\frac{P}{2(24e^2 + e - 1)} \left(\frac{P}{1 - e + 3e^2} + \frac{P}{13 - 13e + 3e^2} \right)}{24(1 - e)} \quad q = 2 \cos(e) \quad (11:16)$$

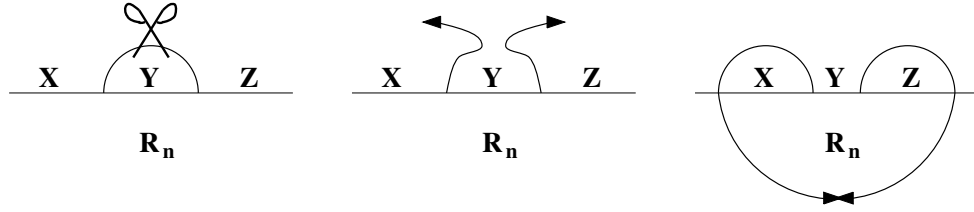
The prediction for $\gamma(q)$ requires that q be less than a critical value given by $q_c = 2 \cos(e_c)$ where e_c is the positive root of $24e_c^2 + e_c - 1 = 0$, namely [16]

$$q_c = 2 \cos \frac{P}{97} \frac{1}{48} = 1.6738 \quad (11:17)$$

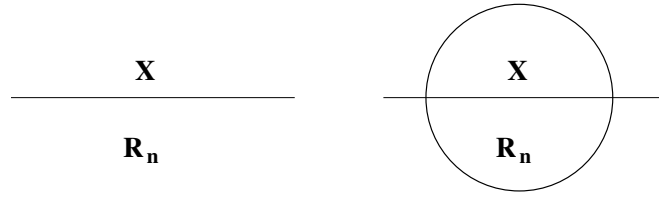
At this value, we have $\gamma = 1$. A heuristic argument shows that the entropically favored semimeanders are then those with a "Russian doll" structure, i.e. those made of a first finite semimeander using only the, say s_1 first bridges closest to the source, of a second semimeander using only the s_2 next bridges (and possibly winding around the set source/ first semimeander), etc... with the s_i 's all finite. We thus expect at q_c a transition to a regime where the winding becomes extensive. The critical value q_c is thus a good candidate for a transition point between the regimes (i) and (ii) of Section 10.1.

12. Numerical checks

The above predictions may be tested numerically by performing a direct enumeration of meanders, semimeanders and other related configurations. Several algorithms have been used, the best ones producing results up to about 50 bridges. We shall present here two particular algorithms, one based on arch growth [15], well adapted to the case of semimeanders, and the other based on a transfer matrix formalism [75,76,17]. Beside exact enumerations, other statistical approaches such as Monte Carlo algorithms were also used in Ref.[77] to investigate large meander statistics.



transformation (I)



transformation (II)

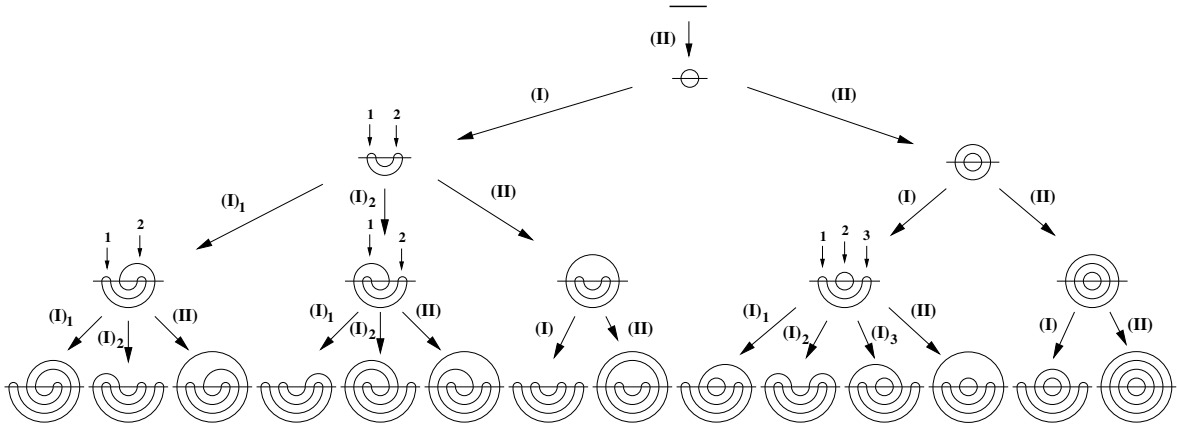


Fig.48 : The arch growth algorithm : the two transformations (I) and (II) are described in the text. X , Y et Z denote arbitrary systems of arches and R_n a rainbow made of n nested arches. Repeated application of (I) and (II) on the empty configuration generates all semimeanders, represented here up to $n = 4$.

12.1. Arch growth algorithm

This algorithm generates configurations of semimeanders. The meanders are then recovered as a particular case of semimeanders with vanishing winding. We use the "open" representation of semimeanders obtained by opening the river as in Fig.38. A semimeander with n bridges is therefore represented by a system of n arches above the (opened) river closed by a rainbow R_n made of n nested arches below the (opened) river. The algorithm generates all semimeanders with $n + 1$ bridges from those with n bridges by

applying to the arch system one of the following two transformations, as illustrated in Fig.48:

- (I) we select one of the outermost upper arches, cut it and re-close it below the river by encircling the original semicircular arch, thus creating two arches above the river, two new crossings with the river and one new arch of rainbow below the river. In the original semicircular arch picture, this transformation corresponds to the creation of one new bridge and does not modify the number of circuits.
- (II) we surround the existing semicircular arch by a big circle, thus creating an outer arch above the river, two new crossings with the river and one new arch of rainbow below the river. In the original semicircular arch picture, this transformation corresponds to the creation of one new bridge and increases by 1 the number of circuits.

It is easy to see that the above algorithm generates all the semicircular arches with $n + 1$ bridges once and only once from the set of semicircular arches with n bridges. Indeed, the transformation is easily inverted by cutting the external arch of the rainbow below the river and gluing it above. Each semicircular arch is thus obtained from the empty configuration in a unique way by the application of a succession of transformations (I) and (II) (see Fig.48). An immediate consequence of this property is that the average number $\text{hout}_n(q)$ of outermost arches above the river for semicircular arches with n bridges weighted by a factor q per connected component is equal to

$$\text{hout}_n(q) = \frac{SM_{n+1}(q)}{SM_n(q)} = q^{n+1} R(q) - q \quad (12:1)$$

The arch growth algorithm was used in Ref.[15] to enumerate semicircular arches up to 27 bridges.

Beyond mere enumeration, this algorithm has the advantage of allowing for a step by step tracking of the number of circuits, thus giving access to the analytic structure of the $SM_n^{(k)}$. More precisely, the number of circuits corresponds to the number of times the transformation (II) was used. For large n and $k = n - l$ with l finite, we deduce for instance that

$$SM_n^{(n-l)} \sim n! \cdot \frac{n^l}{l!} \quad (12:2)$$

corresponding to the $\frac{n!}{1!} = n!$ choices of the transformation (I). More precisely, we have [15]

$$\begin{aligned}
 SM_n^{(n)} &= 1 \\
 SM_n^{(n-1)} &= n-1 \\
 SM_n^{(n-2)} &= \frac{1}{2}(n^2 + n - 8) \\
 SM_n^{(n-3)} &= \frac{1}{6}(n^3 + 6n^2 - 31n - 24) \\
 SM_n^{(n-4)} &= \frac{1}{24}(n^4 + 14n^3 - 49n^2 - 254n)
 \end{aligned} \tag{12.3}$$

obtained by analyzing all possible shapes of meanders with only 1;2;3;4 applications of (I).

12.2. Transfer matrix algorithm

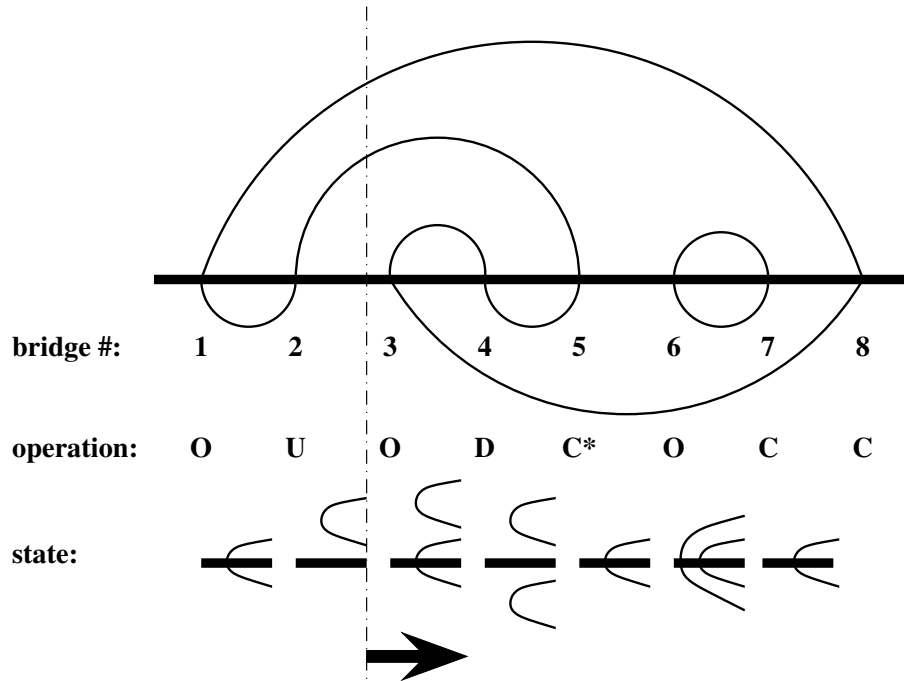


Fig.49: Transfer matrix algorithm. The operators O, C, U and D are described in the text.

This particularly efficient algorithm was first used by Jensen in Ref.[75], where meanders were enumerated up to $2n = 48$ bridges. The idea consists in generating the meanders from left to right one bridge after the other by means of a transfer matrix. The state of

the system between the m -th and the $(m + 1)$ -th bridge is characterized by the connectivity of those arches above and below the river which have been opened but not yet closed (see Fig.49). These arches are indeed connected by pairs in the left part of the meander. These connections form themselves a transverse system of arches, which, together with the relative position of the river, entirely characterize the state of the system. The application of the transfer matrix corresponds to the crossing of a bridge where one of the following four operations takes place (see Fig.49):

O : Opening of a new transverse arch with extremities immediately on both sides of the river.

C : Connection of the two extremities of transverse arches which are immediately on both sides of the river. If these two extremities belong to the same transverse arch, a new circuit of meander has been created on the left of that bridge. Otherwise, the number of circuits remains unchanged (operation denoted by C in Fig.49).

U : Upward migration (with respect to the river) of the system of transverse arches.

D : Downward migration (with respect to the river) of the system of transverse arches.

Starting from the empty state, the repeated application of the transfer matrix allows to generate meanders or semimeanders according to the final state reached after $2n$ or n iterations.

12.3. Numerical results

The above algorithms lead to the following exact enumerations. The table below gives the numbers $SM_n^{(k)}$ of semimeanders with n bridges and k connected components for n up to 27:

Semi-meanders with n bridges and k connected components

n\k	1	2	3	4	5	6	7	8	9	10	11	12	13
1	1												
2	1	1											
3	2	2	1										
4	4	6	3										
5	10	16	11	1									
6	24	48	37	17	1								
7	66	140	126	66	24	6							
8	174	428	430	254	104	32	7						
9	504	1308	1454	956	438	152	41	1					
10	1406	4072	4976	3584	1796	690	211	51	9				
11	4210	12796	16880	13256	7238	3028	1023	282	62	10			
12	12198	40432	57824	49052	28848	12996	4759	1451	366	74	11		
13	37378	129432	197010	179552	113518	54812	21533	7112	1989	464	87	12	
14	111278	413900	675428	658560	444278	226284	95419	33721	10227	2653	577	101	13
15	346846	1342580	2310268	2394504	1720384	939148	415956	155994	50606	14262	3460	706	116
16	1053874	4335288	7927778	8724464	6643492	3833076	1790038	708018	243392	73428	19394	4428	852
17	3328188	14201804	27205180	31575096	25421620	15487428	7613504	3164400	1145250	366100	103642	25820	5576
18	10274466	46226896	93448486	114451388	97136712	62244564	32094902	13965780	5295316	1780690	534494	142940	33758
19	32786630	152594276	321537086	412811544	368280210	247973928	134013518	60951384	24133016	8492044	2681612	761120	193274
20	102511418	500016036	1105589516	1490190544	1395104236	984221764	555915344	263582744	108659880	39849468	13162018	3932262	1061000
21	329903058	1650630740	3812424912	5360943684	5250325378	3876113404	2286993326	1129603888	484054494	184478424	63454876	19831956	5636950
22	1042277722	5472190206	13121988240	19288139802	19746342212	15223550024	9361284260	4806762528	2136797694	844196480	301374534	98069830	29174206
23	3377919260	18264517264	45330375774	69245171564	73863421894	59379645924	38033821330	20294654048	9351763592	3823988336	1413224292	477060460	147790618
24	10765024432	60475691308	156172996170	248463024330	276113486146	231124139318	153915109102	85198977660	40632714144	17168256704	6554314890	2288540120	735416776
25	35095839848	202684618564	540314673678	890477645192	1027609657470	894157177372	618666292694	355164255600	175243060328	76446485224	30103132270	10847350988	3604466262
26	112670468128	673892675030	1863197292582	3188033497580	3821478801772	3453279084296	2478777647126	1473618143854	751285460888	337955598100	137072634698	50877605328	17437690722
27	369192702554	2266436498400	6454265995454	11409453277272	14161346139966	13266154255196	9870806627980	6074897248976	3199508682588	1483533803900	619231827340	236416286832	83407238044

n\k	14	15	16	17	18	19	20	21	22	23	24	25	26	27
14	1													
15	14	1												
16	132	15	1											
17	1016	149	16	1										
18	6924	1199	167	17	1									
19	43448	8493	1402	186	18	1								
20	256880	55153	10305	1626	206	19	1							
21	1451964	3363160	69160	12383	1872	207	20	1						
22	7923526	1955009	434423	85781	14751	2141	249	21	1					
23	42037340	10947269	2594686	554482	105354	17434	2434	272	22	1				
24	217928136	59481467	14895219	3399516	700112	128244	20458	2752	296	23	1			
25	1108184612	315291663	82818768	19909083	4402436	875364	154844	23850	3096	321	24	1		
26	5543795384	1637050027	448523733	113659789	26500047	5641276	1084738	185576	27638	3467	347	25	1	
27	27346198448	83262021621	2376167414	628492938	153966062	37356527	7159268	1333214	220892	31851	3866	374	26	1

Similarly, the table below gives the numbers $M_n^{(k)}$ of meanders with $2n$ bridges and k connected components for n up to 20:

Meanders with $2n$ bridges and k connected components

n\k	1	2	3	4	5	6	7	8	9	10
1	1									
2	2	2								
3	8	12	5							
4	42	84	56	14						
5	262	640	580	240	42					
6	1828	5236	5894	3344	990	132				
7	13820	45164	60312	42840	17472	4004	429			
8	110954	406012	624240	529104	271240	85904	16016	1430		
9	933458	3772008	6540510	6413784	3935238	1569984	405552	4862	4862	
10	8152860	35994184	69323910	76980880	54787208	26200468	8536890	1860480	251940	16796
11	73424650	351173328	742518832	919032664	742366152	412348728	161172704	44346456	8356656	994840
12	678390116	3490681428	8028001566	10941339452	9871243896	6230748192	2830421952	934582000	222516030	3693698
13	6405031050	35253449296	87526544560	130091632424	129477703190	91385152248	47201994762	18117824400	5177642470	1086685600
14	61606881612	360946635312	961412790002	1546164900644	1681013854212	1310296996120	757218876394	330541081704	109808112960	27665650740
15	602189541928	3739935635756	1063094761766	18379165280940	21653861838390	18456675484196	11786257964504	5757601848920	2175182186120	637007339280
16	5969806669034	39193000589780	118257400015312	218576190891816	277215342450784	2563015422007920	1790810462155568	96693197936632	40879675203224	1361237527632
17	59923200729046	413836299216608	1322564193689320	2601195918964184	3531450469030880	3517938623873672	266782286408272	1576533680321408	736731216104224	27449145159648
18	608188709574124	4409705753032648	14863191405246888	30980323101952368	44806855312849362	47820811912386732	39096415694808648	25083534947894304	1283002060659746	5283147737822600
19	62342778351806	47327525317450816	167771227744292160	369289948556000856	566527894954179026	644758338073769464	565064355359024840	390970503448090488	217139225832110534	97860442915614704
20	64477712119584064	511356350415103008	190134532956422790	4405839231880790648	7145814923879522986	8632737343310196256	807705247685170684	5988061883039308848	3587066907601934530	1755310029771295216

n\k	11	12	13	14	15	16	17	18	19	20
11	58786									
12	3922512	208012								
13	161226780	1545320	742900							
14	15193298110	696717840	60843510	2674440						
15	143558599080	24384586200	2986292400	239519700	9694845					
16	3565368581568	727159530240	112831907760	12713873760	942871200	35357670				
17	81730331363736	19370390667040	3609536084152	515709552000	5382308800	3711935040	129644790			
18	1759714658172372	474000318895104	10263016254240	17612853736464	2332549535400	226765486080	14615744220	477638700		
19	36017597277612496	10850034322572432	2669370671766112	532249661425760	846884474003968	10455495457248	951484123440	5756228670	1767263190	
20	706958959835806990	23526564762448572	64713641205591820	14658557362753320	2709804590263396	402058856155712	4650088566990	3976168316200	226760523600	6564120420

These data may be analyzed in two different ways, either numerical, or analytic. The first approach, purely numerical, consists in building $M_n(q)$ and $SM_n(q)$ for the values of n accessible from the data and to directly estimate $R(q)$ (resp. $\bar{R}(q)$) by taking for instance the ratio of two consecutive values of $M_n(q)$ (resp. $SM_n(q)$) and by using appropriate convergence algorithms to extract a limiting value at large n .

The figure 50 shows the obtained estimates of $R(q)$ and $\bar{R}(q)$ for values of q between 0 and 6. One clearly distinguishes two regimes, a large q regime where $R(q) > \bar{R}(q)$ and a low q regime where $R(q) = \bar{R}(q)$ up to numerical errors (recall that at $q = 1$, we already

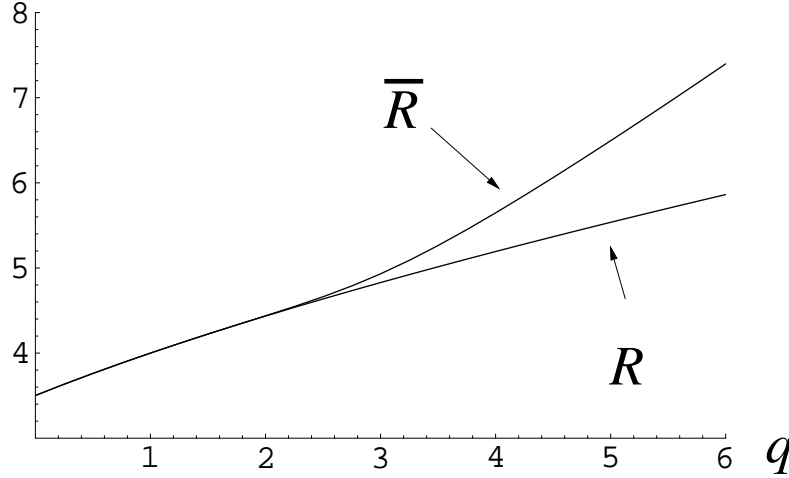


Fig.50: Estimates of $R(q)$ and $\bar{R}(q)$ for q between 0 and 6. The numerical errors are smaller than the thickness of the curves.

know that the two are indeed equal). This confirms the existence of a transition point q_c between a low q phase corresponding to the situation (i) of Section 10.1 of negligible winding, and a large q phase corresponding to the situation (ii) of extensive winding. The precise value of q_c is difficult to estimate as the approach of the two curves is tangential. Still, the graph of Fig.50 is compatible with the analytic prediction of Eq.(11.17).

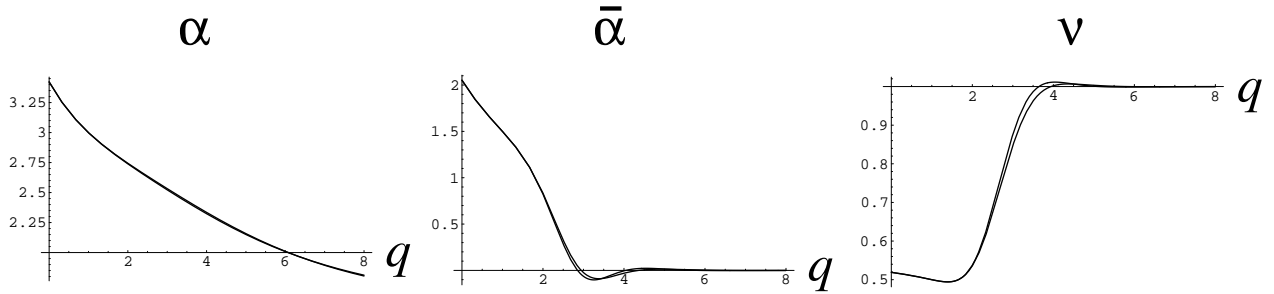


Fig.51: Estimates of the exponents $\alpha(q)$, $\bar{\alpha}(q)$ and $\nu(q)$ for q between 0 and 8. The different curves correspond to different numbers of iterations of the convergence algorithm.

We may similarly estimate the exponents $\alpha(q)$, $\bar{\alpha}(q)$ and even $\nu(q)$ by taking appropriate combinations of (semi-)møander polynomials which converge to these exponents at large n . These estimates are represented in Fig.51 for q between 0 and 8. The estimated value of $\nu(q)$ has a large variation around $q = q_c$, which suggests a discontinuity of ν at the transition point. We therefore expect that $\alpha(q)$ varies continuously for $q < q_c$ (regime (i)) and has a jump discontinuity beyond which $\alpha(q) = 1$ (regime (ii)). The exponent $\bar{\alpha}(q)$

follows the same scenario with a continuous variation for $q < q_c$ and a jump discontinuity to a constant value $c(q) = 0$ (we already know that $c(q)^{q \rightarrow 1} = 0$). Finally, the exponent $c(q)$ seems to decrease without discontinuity toward its limiting value $c(q)^{q \rightarrow 1} = 3/2$.

As far as the original problem of meanders and semi-meanders is concerned ($q \neq 0$), a refined analysis of the numerical data is presented in Refs.[75,76] and leads to the precise estimates

$$R(q=0) = R(q=0) = 3.501837(3) \quad (12.4)$$

$$c(q=0) = 3.4208(6) \quad c(q=0) = 2.0537(2) \quad (12.5)$$

These exponents agree remarkably with the predicted values $c(0) = 3.420132 \dots$ of Eq.(11.7) and $c = 2.053198 \dots$ of Eq.(11.12).

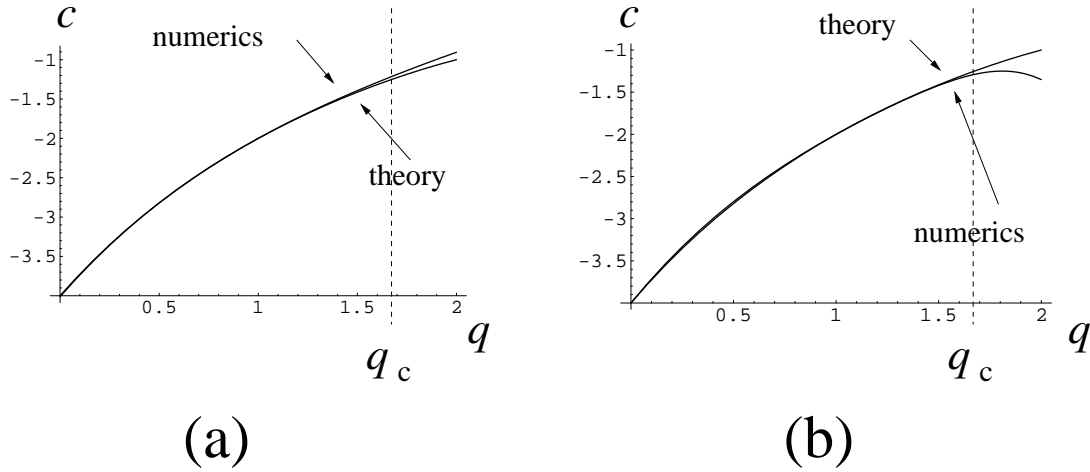


Fig.52: Comparison between the theoretical value $c_{\text{meander}}(0;q)$ of the central charge and its estimated value from the numerical data of meanders (a) and semi-meanders (b).

For generic q , we have represented in Fig.52 the comparison between the theoretical central charge $c_{\text{meander}}(0;q)$ of Eq.(11.14) and its two numerical estimates: (a) that obtained by inverting the relation (11.15) from the measured value of $c(q)$ and (b) that obtained by inverting the relation (11.16) from the measured value of $c(q)$. For $q = 0$, the estimates (12.5) lead respectively in the cases (a) and (b) to $c = 3.4003(3)$ and $c = 3.4002(1)$.

Note finally that the above transfer matrix method was also adapted to estimate configurational exponents for other meandric numbers such as those with "eight" or "cherry" river configurations (see Fig.47). The agreement with the predictions (11.13) is excellent

[17]. Using the same method, it was also checked that the presence of the tangency vertex does not affect the exponents for the ordinary gravity version of meanders, hence it corresponds to an irrelevant perturbation, as we argued.

A second way of exploiting the data consists in using them to obtain a large q expansion of various quantities. At large q , the expansion of $R(q)$ up to order p in $1=q$ is governed by $SM_n^{(n-1)}$ for $l = p+1$. We have seen that for finite and n large enough, $SM_n^{(n-1)}$ is a polynomial of n of degree l . This property is a direct consequence of the arch growth algorithm. The existence of a thermodynamic limit for $SM_n(q)^{1/n}$ then guarantees that $R(q) = 0$ as long as the $1=q$ expansion remains valid. Moreover, imposing that the above polynomials actually reproduce the numerical data leads to their complete determination up to $l = 19$. The net result is finally a large q expansion of $R(q)$, given by [15]

$$R(q) = q + 1 + \frac{2}{q} + \frac{2}{q^2} + \frac{2}{q^3} - \frac{4}{q^5} - \frac{8}{q^6} - \frac{12}{q^7} - \frac{10}{q^8} - \frac{4}{q^9} + \frac{12}{q^{10}} + \frac{46}{q^{11}} + \frac{98}{q^{12}} + \frac{154}{q^{13}} + \frac{124}{q^{14}} + \frac{10}{q^{15}} - \frac{102}{q^{16}} + \frac{20}{q^{17}} - \frac{64}{q^{18}} + O\left(\frac{1}{q^{19}}\right) \quad (12:6)$$

A similar analysis for meanders allows to determine the analytic structure of the $M_n^{(n-1)}$ for large n and finite l . Instead of polynomials, one obtains rational fractions in this case. This results in [15]

$$R(q) = 2^p \bar{q} + 1 + \frac{1}{q} + \frac{3}{2q^2} - \frac{3}{2q^3} - \frac{29}{8q^4} - \frac{81}{8q^5} - \frac{89}{16q^6} + O\left(\frac{1}{q^7}\right) \quad (12:7)$$

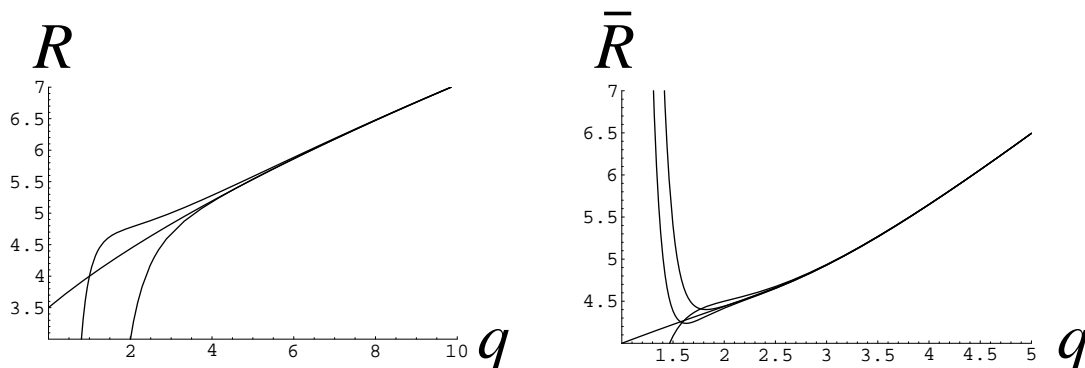


Fig.53: Comparison between the numerical estimates and the large q expansions for $R(q)$ (a) and $\bar{R}(q)$ (b). For $R(q)$, we have drawn the expansions truncated at order q^{-3} and q^{-6} . For $\bar{R}(q)$, we have drawn the expansions truncated at order q^{-6} , q^{-12} and q^{-18} .

The figure 53 shows the comparison between the values of $R(q)$ and $R(q)$ as estimated numerically and the expansions (12.7) and (12.6) above.

The analysis of the corrections to the polynomial behavior for the numbers $SM_n^{(n-1)}$ displays corrections of the form $R(q)^n$ with $R(q)$ given by Eq.(12.7). It is thus natural to think that the expansions above are valid as long as $R(q) > R(q)$, i.e. in the whole regime (ii), and in particular that $\phi(q) = 0$, $\phi(q) = 1$ for all $q > q_c$. For $q < q_c$, these expansions are no longer valid and therefore do not allow to describe the regime (i). Fortunately, this regime (i) is precisely that for which we have obtained predictions from the KPZ formula.

13. Meanders as folding of random quadrangulations

In this paper, we started in part A by a study of the planar folding of the triangular lattice and extended it in part C to the case of random triangulations. We saw that this latter problem has a fully packed loop formulation on trivalent graphs. The above formulation of the meander problem as a fully packed loop gas on random tetravalent graphs suggests a link between this problem and the folding of quadrangulations. In this Section we will "close the loop" by showing that the meander problem is indeed the same problem as that of planar folding of random quadrangulations. This may be seen as the non-trivial gravitational version of the trivial correspondence between the $FP L^2(2;2)$ model with only the crossing vertex and the planar folding of the regular square lattice. This allows alternatively to view the folding of a self-avoiding one-dimensional chain as the phantom folding of a two-dimensional random quadrangulation, a somewhat surprising result.

Let us start by considering the set of planar random quadrangulations, namely tessellations for which all the tiles are unit squares. By planar folding of such a quadrangulation, we again mean any map of the quadrangulation onto the plane whose restriction to each square tile is an isometry. The nodes of the quadrangulation then necessarily have their image on the nodes of a regular square lattice in the plane.

Foldability of random quadrangulations

As in the case of triangulations, we first address the question of foldability in the plane. By use of the four-coloring of the nodes of the regular square lattice (see figure 54), we immediately see that, if a folding exists, it naturally induces a four-coloring of the nodes of the quadrangulation. In this coloring, the four colors 1, 2, 3, 4 must appear in

4	3	4	3	4
1	2	1	2	1
4	3	4	3	4
1	2	1	2	1

Fig.54 : Four-coloring of the nodes of the regular square lattice

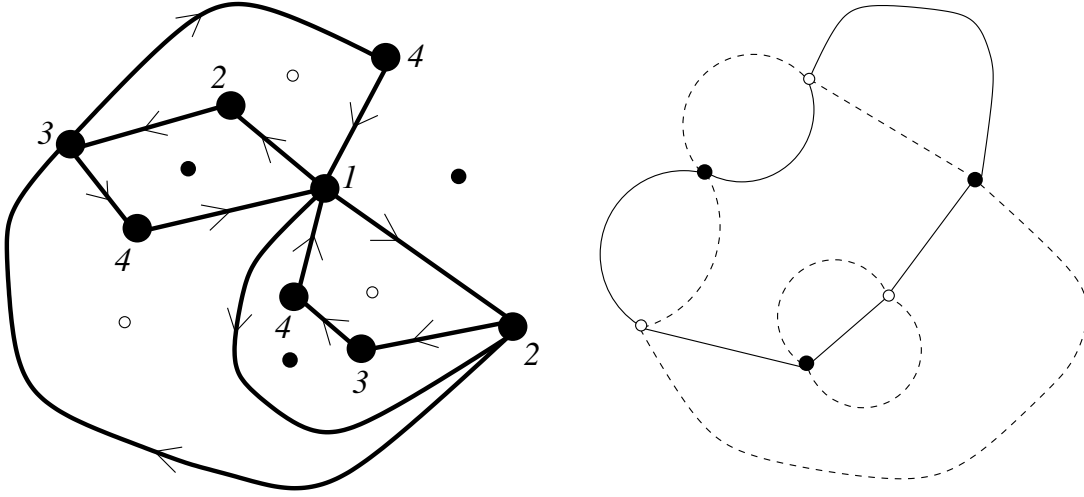


Fig.55 : Example of a foldable quadrangulation (left), i.e. a quadrangulation whose nodes may be colored by four colors 1, 2, 3 and 4 in such a way that the nodes around each face are in cyclic order 1,2,3,4 or 4,3,2,1, also corresponding to an orientation of the links. The squares have been deformed in the planar representation. The equivalent dual tetravalent graph (right) is node-bicolored. The links dual to the 1{2 or 3{4 links form black lines which cross white lines formed by the links dual to the 2{3 and 4{1 ones.

cyclic order 1,2,3,4 or 4,3,2,1 around each face. Conversely, a quadrangulation with such a four-coloring (which is unique up to a cyclic permutation of the colors) is clearly foldable onto a single square whose four vertices would have been labeled 1,2,3,4. We thus have the following equivalent characterizations for genus zero quadrangulations:

1. The quadrangulation is foldable in the plane
2. Its nodes may be colored by four colors 1, 2, 3 and 4 appearing in cyclic order 1,2,3,4 or 4,3,2,1 around each face
3. Its faces are bicolored by two colors which must be distinct on two neighboring faces
4. Its edges may be oriented in such a way that each face has a well-defined orientation
5. The number of faces around each node is even

6. The number of edges adjacent to each node is even

This last property 6 justifies that we call such quadrangulations Eulerian.

The planar foldable quadrangulations are therefore the Eulerian quadrangulations, characterized by any of the above equivalent properties.

The number of such quadrangulations with $4s$ edges (and rooted, i.e. with a distinguished oriented link) is given by [78]

$$N_s = 8 \frac{3^{s-1} (3s)!}{(2s+2)! s!} = \frac{1}{6} \frac{\frac{9}{2}^{2s}}{s^2} \quad (13.1)$$

to be compared with Eq.(6.14).

Planar folding of random quadrangulations

The four-coloring of the nodes allows to classify all the links of the quadrangulation into the "horizontal" links $1\{2$ and $3\{4$ and the "vertical" links $2\{3$ and $4\{1$. These links are moreover naturally oriented in the direction $1 \rightarrow 2 \rightarrow 3 \rightarrow 4 \rightarrow 1$ (see figure 55). The dual graph is a tetravalent node-bicolored graph, on which the dual of horizontal links form a gas of, say black, fully packed loops, and the dual of vertical links a complementary gas of white fully packed loops. The two systems of loops are further constrained to cross each other at the nodes of the tetravalent graph.

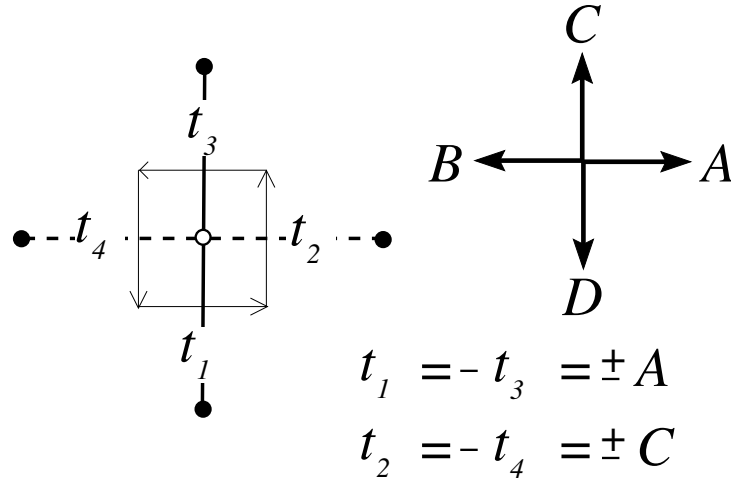


Fig.56: Folding constraints for quadrangulations. In order for the folded image of a face to be a square of side unity, we must have $t_1 = t_3 = A$ and $t_2 = t_4 = C$ where A and C are two orthogonal unit vectors. These constraints propagate to the neighboring squares so that each square has its two horizontal links equal to A and $B = -A$, and its two vertical links equal to C and $D = -C$.

It is then clear that, in a folded configuration of the quadrangulation, the faces are mapped on unit squares of the square lattice, hence the link variables (defined on the oriented links) may take only two values, say A and $B = -A$ on the horizontal links, while those on the vertical links may take two values C and $D = -C$, where A and C are orthogonal unit vectors (see figure 56). Moreover, the two horizontal (resp. vertical) links around a given face have opposite values.

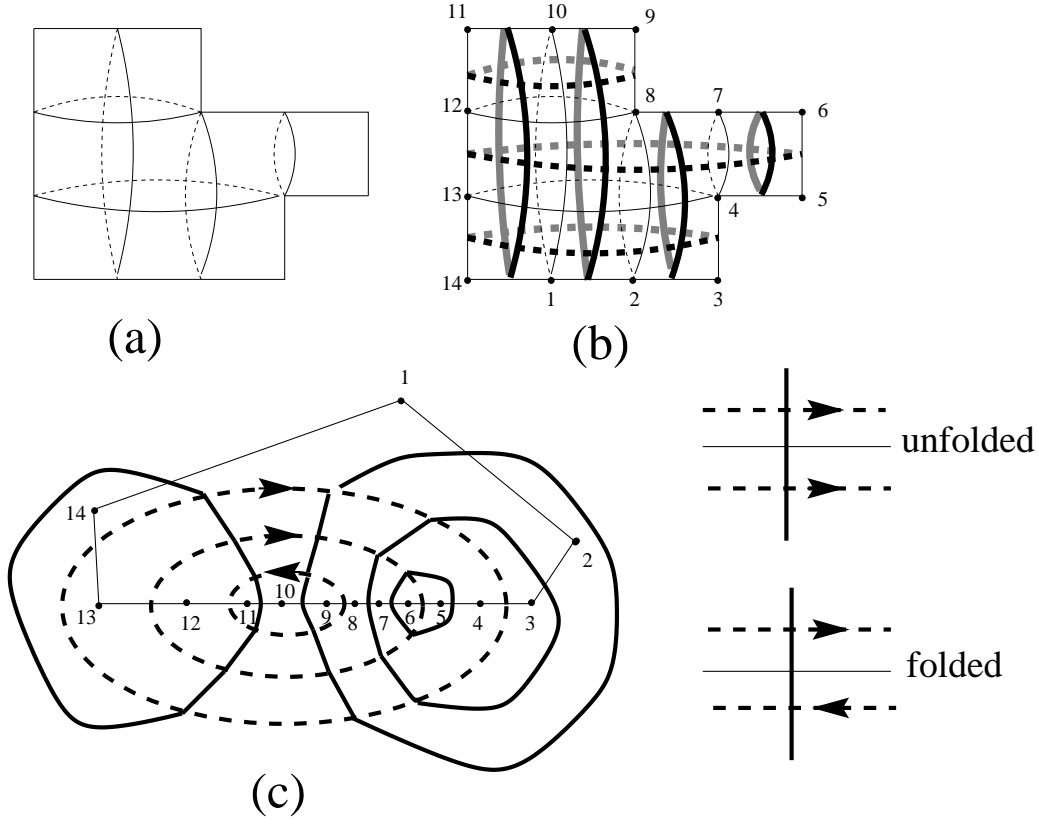


Fig. 57: Example of planar foldable quadrangulation (a) in a spherical representation. The corresponding black and white fully packed loops (b) are entirely fixed. Only their orientation remains arbitrary. The same loops in a planar representation (c) form a configuration of the $GFPL^2(2;2)$ model. The orientation of the white loops determines which horizontal links are folded, according to the rule displayed on the right. A similar rule determines which vertical links which are folded according to the orientation of the black loops (not represented here). For the particular configuration of loops drawn here, the links of the "perimeter" joining the nodes labeled 1 to 14 are necessarily folded irrespectively of the orientation of the black and white loops. The other links may be folded or not. For instance, the particular choice of orientation of the white loops represented here in (c) corresponds to having a horizontal fold between the nodes 12 and 8 in the representation (b), with thus four folded links.

In a dual representation, we can transfer the \color" A , B , C or D of the link variable to the dual link, in which case the colors alternate between A and B along the black loops, and between C and D along the white ones. Orienting each link of color A (resp. C) from the adjacent black node, and each link of color B (resp. D) from the adjacent white node, assigns a well-defined orientation to each loop. The orientations are independent on each loop, which precisely defines the $\text{GFPL}^2(2;2)$ model. The orientation of the loops corresponds to the folding degree of freedom, with the correspondence that a horizontal (resp. vertical) link is folded if and only if the two white (resp. black) loops immediately on each side of the dual link have opposite orientations (see figure 57). Conversely, the height variable associated to a configuration of the $\text{GFPL}^2(2;2)$ model (which by definition allows only for crossing vertices) with the rules of figure 44 and the choice $B = A$ and $D = C$ is nothing but the position of the nodes in the corresponding folded configuration. To summarize, the $\text{GFPL}^2(2;2)$ model describes the planar folding of random quadrangulations.

Complete folding, partial folding and non-unfoldable quadrangulations

The situation is simpler than that of triangulations for the following reason. Given any foldable quadrangulation, or rather its dual tetravalent node-bicolored graph, there exists clearly a unique configuration of fully packed loops (up to a global interchange of black and white loops) compatible with the rule that loops have to cross each other at each vertex. For a given graph, there is no entropy associated with the positioning of the loops. The folding entropy is therefore entirely encoded in the choice of orientations for the loops.

A first consequence is that the complete folding of quadrangulations, i.e. their folding onto a single square is simply described by the $\text{GFPL}^2(1;1)$ model. Indeed, the folding onto a single square always exists and is unique for each foldable quadrangulation. On the tetravalent graph, it is obtained by the unique orientation of the loops defined as follows:

1. We orient the outermost black loops counterclockwise;
2. Inside each of these loops, we orient clockwise the outermost black loops;
3. We continue iteratively for deeper loops by alternating the counterclockwise and clockwise orientations;
4. We repeat the procedure 1-3 for white loops.

One clearly sees (see figure 58) that all the loops of a given color on neighboring nodes have opposite orientations, hence all links are folded.

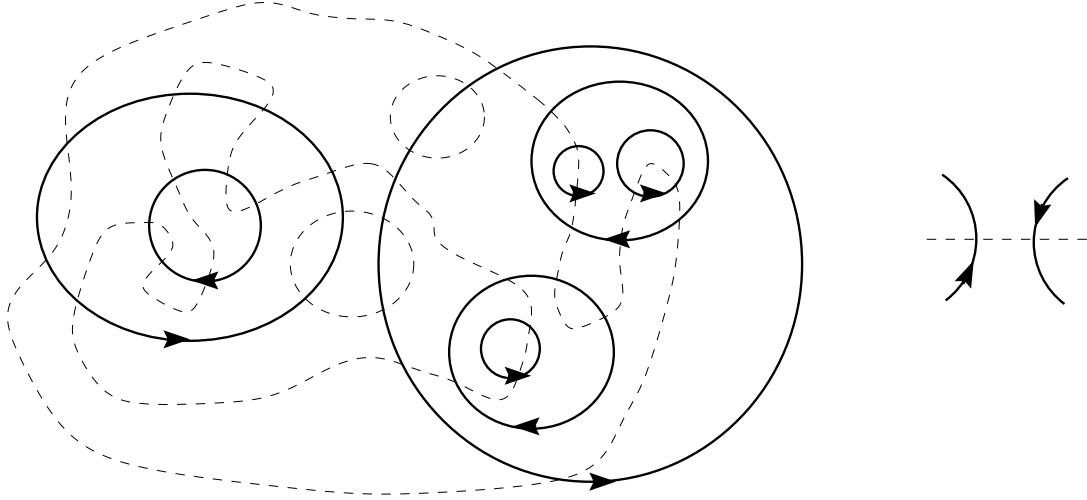


Fig.58: Orientation of the loops leading to the complete folding. The black loops are oriented alternatively in the counterclockwise and clockwise direction as we go deeper in the graph from the outermost loops. In this way, black loops on both sides of any white link always have opposite orientations, hence all vertical links are folded. The complete folding is obtained by orienting the white loops accordingly so that all horizontal links are folded as well.

The foldable quadrangulations being in one-to-one correspondence with their complete foldings, we deduce that the $\text{GFPL}^2(1;1)$ model also counts Eulerian quadrangulations, whose number is given by Eq.(13.1).

Similarly, the $\text{GFPL}^2(1;2)$ model describes the partial folding of quadrangulation, i.e. the complete folding in one direction only, with all vertical links folded, while the horizontal ones may be folded or not. The above interpretations are compatible with the values of the central charge $c_{\text{meander}}(2;2) = 2$ for the planar folding, $c_{\text{meander}}(1;1) = 0$ for the complete folding, and $c_{\text{meander}}(1;2) = 1$ for the partial folding in one direction.

The $\text{GFPL}^2(1;q)$ model was discussed in Section 10.3 with in particular the prediction (10.15)–(10.16) for the asymptotics of the number of folded configurations. In particular for $q = 1$, one recovers $R(1;1) = 9=2$ as apparent on formula (13.1). For $q = 2$, the number of configurations of partial folding in one direction grows like $(9=2)^{2s}$ which, divided by the $(9=2)^{2s}$ foldable quadrangulations gives an average number of foldings varying as $(9=2)^{2s}$, i.e. $(9=2)$ per horizontal link.

Finally, the original meander problem with $n_1 = n_2 = 0$ may be interpreted as describing the foldable but "non-unfoldable" quadrangulations, i.e. the quadrangulations for which the complete folding is the only possible one. Indeed, requiring that no unfolding is possible amounts to requiring that all the relative orientations of the loops are fixed, which is true if and only if there is a unique loop of either species.

The mixed situation where $n_1 = 0$ only amounts to selecting the quadrangulations which are non-unfoldable on vertical links, but possibly unfoldable on the horizontal links. For $n_2 = q = 1$, one imposes a complete folding of these horizontal links (although some of them could a priori be unfolded) while for $n_2 = q = 2$, one allows for unfolding the horizontal unfoldable links.

To conclude, the passage via the meander picture has allowed to prove that the enumeration of foldings on a single stamp of a closed, one-dimensional and self-avoiding strip of $2n$ stamps is equivalent to the enumeration of planar, two-dimensional phantom random quadrangulations with $2n$ faces, which are both foldable and "non-unfoldable", a quite amazing result.

CONCLUSION

In this paper, we tried to give a unified presentation of a number of problems arising from the statistical physics of folding. We explained the intimate links between foldings of lattices or graphs, colorings of their links and/or nodes, as well as fully packed loop gases. Beside phantom folding, the introduction of self-avoidance in one dimension led us to the meander problem, itself related to phantom folding of random quadrangulations. We have introduced various formulations of these problems: constrained spin variables, height models, Coulomb gas description, all giving different angles of approach.

In the case of regular lattices, the foldings in the presence of bending energy give rise to rich phase diagrams with conformational transitions intimately linked to the underlying geometry. In the case of random lattices, a similar sensitivity to the underlying graph was observed. It leads in particular to different universality classes according to the nature of the underlying lattice, distinguishing between ordinary and Eulerian gravity. More precisely, a shift of the central charge $c \rightarrow c + 1$ of the associated field theory is observed when going from dense loops to fully packed loops provided the latter are defined on bipartite lattices.

This phenomenon seems to contradict the more familiar notion of universality in statistical physics. Note however that a similar breakdown of universality occurs in other systems for which the symmetry of the problem is linked to the ambient geometry. A particular example is that of "hard objects", say particles occupying the nodes of a lattice so that no two adjacent nodes be simultaneously occupied [79,80]. On the regular lattice, these include the famous "hard square" problem on the square lattice [81], and the "hard hexagon" problem on the triangular lattice [82] (see also [83]). These two problems display a crystallization transition between an ordered phase at high density of particles and a disordered phase of low density. The universality class of the transition point differs however for these two problems. This is easily understood by observing that the symmetry of the high density groundstates (corresponding to having particles on one sub-lattice made of next-nearest neighbors on the original lattice) differs. The square lattice is bipartite and has two such sub-lattices, leading to an Ising-like transition point, while the triangular lattice is tripartite with three such sub-lattices, leading to a transition point in the universality class of the critical 3-state Potts model. When going to random lattices, a similar sensitivity was observed in the following sense: it was shown [84] that hard particles on random tetravalent graphs display no crystallization transition when defined on arbitrary

graphs (ordinary gravity) while the transition is restored for bipartite graphs (Eulerian gravity). A simple heuristic explanation for this is that ordered groundstates exist only when the graph is bipartite. Remarkably, the ordinary or Eulerian nature of the graph is again what matters.

Another surprise of our study is the appearance of irrational critical exponents for a priori simple combinatorial problems. Here again, other examples have been found. For instance, it was recently conjectured [85] that the enumeration of closed planar curves with n intersections (a problem related to the enumeration of alternating knots) corresponds to the coupling to gravity of a conformal theory with central charge $c = -1$, and that the asymptotic large n behavior is characterized by the same irrational exponent (8.5) as in Section 8.

In these notes, we have limited ourselves to the simplest examples of folding. As we mentioned already, our description may be extended to the case of all compactly 2D foldable lattices of Fig 5, or higher D -dimensional simplices, all with their own (multicolored) fully packed loop gas formulation and with their own symmetry. Similarly, meanders may be generalized in various ways:

- meanders drawn on surfaces with higher genus [13], accessible via topological expansion of the black and white matrix model of Section 10.3;
- colored meanders, based on multicolor generalizations of the Temperley-Lieb algebra [18,86];
- $SU(N)$ meanders, based on higher quotients of the Hecke algebra generalizing the Temperley-Lieb algebra ($N = 2$) [70].

Finally, a very natural question is that of a proper description of self-avoidance for lattices of dimension $D \geq 2$. At this time, only enumerations for rectangular domains of the square lattice with very small sizes are known [87] and no systematic approach has been devised yet.

The most advanced results presented here all rely on field-theoretical effective descriptions. It would be desirable to obtain the same results via a more traditional combinatorial approach. A first step in this direction was performed recently [46,47,91] by solving various planar graph enumeration problems with combinatorics of trees. This approach is based on a proper cutting of the graphs into trees with local characterizations. Alternatively, it relates large graph statistics to properties of the so-called Integrated SuperBrownian Excursion (ISE), a probabilistic description of tree embeddings [88]. In view of these developments, we may expect similar technique to apply to loop gas systems on random

graphs. Another probabilistic direction concerns stochastic Loewner evolution (SLE) in the context of which various exponents, predicted in Ref.[89] by use of the equation (7.3), were derived rigorously with the help of Brownian motion [90].

As a challenge for the reader, the simple combinatorial problem displayed in Fig.31 has a simple transfer matrix formulation and we may hope for an exact analytic solution to be within reach.

References

- [1] Protein Folding Handbook, J. Buchner and T. Kiefhaber Eds., J. Wiley & Sons (2005).
- [2] Statistical mechanics of membranes and surfaces (2nd edition), D. Nelson, T. Piran and S. Weinberg Eds., World Scientific Publishing, June 2004.
- [3] A. Lobkovsky, S. Gentges, H. Li, D. Morse and T. Witten, Scaling properties of stretching ridges in a crumpled elastic sheet, *Science* 270 (1995) 1482-1485.
- [4] P. Di Francesco and E. Guitter, Entropy of folding of the triangular lattice, *Europhys. Lett.* 26 (1994) 455-460, [arXiv:cond-mat/9402058](#).
- [5] P. Di Francesco and E. Guitter, Folding transition of the triangular lattice, *Phys. Rev. E* 50 (1994) 4418-4426, [arXiv:cond-mat/9406041](#).
- [6] M. Bowick, P. Di Francesco, O. Golinelli and E. Guitter, Three-dimensional folding of the triangular lattice, *Nucl. Phys. B* 450 [FS] (1995) 463-494, [arXiv:cond-mat/9502063](#).
- [7] P. Di Francesco, E. Guitter and S. Mori, Folding of the triangular lattice with quenched random bending rigidity, *Phys. Rev. E* 55 (1997) 237-251, [arXiv:cond-mat/9607077](#).
- [8] M. Bowick, O. Golinelli, E. Guitter and S. Mori, Geometrical folding transitions of the triangular lattice in the face-centered cubic lattice, *Nucl. Phys. B* 495 [FS] (1997) 583-607, [arXiv:cond-mat/9611105](#).
- [9] P. Di Francesco, B. Eynard and E. Guitter, Coloring random triangulations, *Nucl. Phys. B* 516 [FS] (1998) 543-587, [arXiv:cond-mat/9711050](#).
- [10] B. Eynard, E. Guitter, C. Kristjansen, Hamiltonian cycles on a random three-coordinate lattice, *Nucl. Phys. B* 528 (1998) 523-532, [arXiv:cond-mat/9801281](#).
- [11] E. Guitter, C. Kristjansen, and J. Nielsen, Hamiltonian cycles on random Eulerian triangulations, *Nucl. Phys. B* 546 (1999) 731-750, [arXiv:cond-mat/9811289](#).
- [12] P. Di Francesco, E. Guitter and C. Kristjansen, Fully packed $O(n=1)$ model on random Eulerian triangulations, *Nucl. Phys. B* 549 (1999) 657-667, [arXiv:cond-mat/9902082](#).
- [13] P. Di Francesco, O. Golinelli and E. Guitter, Meander, folding and arch statistics, *Math. Comput. Modelling* 26 (1997) 97-147, [arXiv:hep-th/9506030](#).
- [14] P. Di Francesco, O. Golinelli and E. Guitter, Meanders and the Temperley-Lieb algebra, *Commun. Math. Phys.* 186 (1997), 1-59, [arXiv:hep-th/9602025](#).
- [15] P. Di Francesco, O. Golinelli and E. Guitter, Meanders: a direct enumeration approach, *Nucl. Phys. B* 482 [FS] (1996) 497-535, [arXiv:hep-th/9607039](#).
- [16] P. Di Francesco, O. Golinelli and E. Guitter, Meanders: exact asymptotics, *Nucl. Phys. B* 570 (2000) 699-712, [arXiv:cond-mat/9910453](#).
- [17] P. Di Francesco, E. Guitter and J. Jacobsen, Exact meander asymptotics: a numerical check, *Nucl. Phys. B* 580 (2000) 757-795, [arXiv:cond-mat/0003008](#).
- [18] P. Di Francesco, Folding and coloring problems in mathematics and physics, *Bulletin of the AMS*, Vol. 37, No. 3 (2000) 251-307.

- [19] P. Di Francesco, Matrix model combinatorics: applications to folding and coloring, in Random matrices and their applications, P. Bleher, A. Its eds. (Cambridge University Press), MSRI Publications 40 (2001), 111-170, [arXiv:math-ph/9911002](#).
- [20] P. Di Francesco, Geometrically constrained statistical models on fixed and random lattices: from hard squares to meanders, [arXiv:cond-mat/0211591](#).
- [21] D.R. Nelson and L. Peliti, Fluctuations in membranes with crystalline and hexatic order, *J. Physique* 48 (1987) 1085-1092.
- [22] Y. Kantor and D.R. Nelson, Crumpling transition in polymerized membranes, *Phys. Rev. Lett.* 58 (1987) 2774-2777 and Phase transitions in flexible polymeric surfaces, *Phys. Rev. A* 36 (1987) 4020-4032.
- [23] M. Paczuski, M. Kardar and D.R. Nelson, Landau theory of the crumpling transition, *Phys. Rev. Lett.* 60 (1988) 2638-2640.
- [24] F. David and E. Guitter, Crumpling transition in elastic membranes: renormalization group treatment, *Europhys. Lett.* 5 (1988) 709-713.
- [25] P. Di Francesco, Folding the square-diagonal lattice, *Nucl. Phys. B* 525 (1998) 507-548, [arXiv:cond-mat/9803051](#); Folding transitions of the square-diagonal lattice, *Nucl. Phys. B* 528 (1998) 609-634, [arXiv:cond-mat/9804073](#).
- [26] Y. Kantor and M.V. Jaric, Triangular lattice foldings: a transfer matrix study, *Europhys. Lett.* 11 (1990) 157-161.
- [27] R.J. Baxter, Colorings of a hexagonal lattice, *J. Math. Phys.* 11 (1970) 784-789.
- [28] E.N.M. Cirillo, G. Gonnella and A. Pelizzola, Folding transitions of the triangular lattice with defects, *Phys. Rev. E* 53 (1996) 1479-1484, [arXiv:hep-th/9507161](#).
- [29] E.N.M. Cirillo, G. Gonnella and A. Pelizzola, Folding transition of the triangular lattice in a discrete three-dimensional space, *Phys. Rev. E* 53 (1996) 3253-3256, [arXiv:hep-th/9512069](#).
- [30] H.W.J. Blöte and B.Nienhuis, Fully packed loop model on the honeycomb lattice, *Phys. Rev. Lett.* 72 (1994) 1372-1375.
- [31] R.J. Baxter, Exactly solved models in statistical mechanics, Academic Press, London (1984).
- [32] For an introduction to the Coulomb gas formalism, see B.Nienhuis, Phase transitions and critical phenomena, Vol. 11, eds. C. Domb and J.L. Lebowitz, Academic Press (1987).
- [33] E.F. Shender, V.B. Cherepanov, P.C.W. Holdsworth, and A.J. Berlinsky, Kagome antiferromagnet with defects: Satisfaction, frustration, and spin folding in a random spin system, *Phys. Rev. Lett.* 70 (1993), 3812-3815, [arXiv:cond-mat/9303031](#).
- [34] J. Kondev, J. de Gier and B.Nienhuis, Operator spectrum and exact exponents of the fully packed loop model, *J. Phys. A* 29: Math. Gen. (1996) 6489-6504, [arXiv:cond-mat/9603170](#).

- [35] for a general introduction to conformal field theory, see P. Di Francesco, P. Mathieu and D. Senechal, *Conformal field theory*, Graduate Texts in Contemporary Physics, Springer (1996) 1-890 (1st ed.) and Springer (1999) 1-890 (2nd ed.).
- [36] P. A. MacMahon, *Combinatory analysis*, Vol. 2, Cambridge University Press (1916), reprinted by Chelsea, New York (1960).
- [37] M. T. Batchelor, J. Suzuki and C. M. Yung, Exact results for Hamiltonian walks from the solution of the fully packed loop model on the honeycomb lattice, *Phys. Rev. Lett.* 73 (1994) 2646-2649, [arXiv:cond-mat/9308083](#).
- [38] V. Kazakov, Bifocal regularization of models of random surfaces, *Phys. Lett. B* 150 (1985) 282-284; F. David, Planar diagrams, two-dimensional lattice gravity and surface models, *Nucl. Phys. B* 257 (1985) 45-58; J. Ambjørn, B. Durhuus and J. Fröhlich, Diseases of triangulated random surface models and possible cures, *Nucl. Phys. B* 257 (1985) 433-449; V. Kazakov, I. Kostov and A. Migdal Critical properties of randomly triangulated planar random surfaces, *Phys. Lett. B* 157 (1985) 295-300.
- [39] E. Brezin, C. Itzykson, G. Parisi and J.-B. Zuber, Planar diagrams, *Comm. Math. Phys.* 59 (1978) 35-51.
- [40] P. Di Francesco, P. Ginsparg and J. Zinn-Justin, 2D gravity and random matrices, *Physics Reports* 254 (1995) 1-131, [arXiv:hep-th/9306153](#).
- [41] B. Eynard, *Random matrices*, Saclay Lecture Notes (2000), <http://www-spt.cea.fr/lectures/notes.shtml>.
- [42] V. G. Knizhnik, A. M. Polyakov and A. B. Zamolodchikov, Fractal structure of 2D quantum gravity, *Mod. Phys. Lett. A* 3 (1988) 819-826; F. David, Conformal field theories coupled to 2D gravity in the conformal gauge, *Mod. Phys. Lett. A* 3 (1988) 1651-1656; J. Distler and H. Kawai, Conformal field theory and 2D quantum gravity, *Nucl. Phys. B* 321 (1989) 509-527.
- [43] This problem is discussed in the mathematical entertainments section, edited by A. Shen, of the *Mathematical Intelligence* Volume 19 number 4 (1997) 48.
- [44] W. Tutte, A census of planar maps, *Canad. Jour. of Math.* 15 (1963) 249-271.
- [45] P. Di Francesco, Rectangular matrix models and combinatorics of colored graphs, *Nucl. Phys. B* 648 (2003) 461-496, [arXiv:cond-mat/0208037](#).
- [46] G. Schaefer, Bijective census and random generation of Eulerian planar maps, *Electronic Journal of Combinatorics*, vol. 4 (1997) R20; *Conjugaison d'arbres et cartes combinatoires aléatoires*, PhD Thesis, Université Bordeaux I (1998).
- [47] J. Bouttier, P. Di Francesco and E. Guitter, Census of planar maps: From the one-matrix model solution to a combinatorial proof, *Nucl. Phys. B* 645 (2002) 477-499, [arXiv:cond-mat/0207682](#).
- [48] J. Bouttier, P. Di Francesco and E. Guitter, Counting colored random triangulations, *Nucl. Phys. B* 641 [FS] (2002) 519-532, [arXiv:cond-mat/0206452](#).

- [49] M .Bousquet-Mélou and G .Schaeffer, Enumeration of planar constellations, *Adv. in Applied Math.*, 24 (2000) 337–368.
- [50] B .Eynard and C .Kristjansen, An iterative solution of the three-color problem on a random lattice, *Nucl.Phys.B* 516 (1998) 529–542, [arXiv:cond-mat/9710199](#).
- [51] I.Kostov, Exact solution of the three-color problem on a random lattice, *Phys.Lett. B* 549 (2002) 245–252, [arXiv:hep-th/0005190](#).
- [52] I.Kostov, $O(n)$ vector model on a planar random lattice: spectrum of anomalous dimensions, *Mod.Phys.Lett.A* 4 (1989) 217–226; B .Eynard and C .Kristjansen, More on the exact solution of the $O(n)$ model on a random lattice and an investigation of the case $n > 2$, *Nucl.Phys.B* 466 (1996) 463–487, [arXiv:hep-th/9512052](#).
- [53] B .Duplantier and I.Kostov, Conformal spectra of polymers on a random surface, *Phys.Rev.Lett.* 61 (1988) 1433–1437.
- [54] for a combinatorial interpretation of this formula, see R .Cori, S .Dulucq and G .Viennot, Shule of parenthesis systems and Baxter permutations, *J.Combin.Theory A* 43 (1986) 1–22.
- [55] V .Kazakov and P .Zinn-Justin, Two-matrix model with ABA B interaction, *Nucl.Phys.B* 546 (1999) 647–668, [arXiv:hep-th/9808043](#).
- [56] E .Lucas *Theorie des nombres I*, Gauthier-Villars, Paris (1891); reedited by Blanchard, Paris, (1961).
- [57] A .Sainte Lague *Avec des nombres et des lignes: recreations mathematiques*, p 147, Vuibert, Paris (1937).
- [58] J.Touchard, Contributions a l’etude du probleme des timbres poste, *Canad.J.Math.* 2 (1950) 385–398.
- [59] J.Koehler, Folding a strip of stamps, *J.Combin.Theory* 5 (1968) 135–152.
- [60] W .Lunnon, A map{folding problem, *Math.of Computation* 22 (1968) 193–199.
- [61] V .Arnold, The branched covering of $CP_2 \setminus S_4$, hyperbolicity and projective topology, *Siberian Math.Jour.* 29 (1988) 717–726.
- [62] S.Lando and A .Zvonkin, Plane and projective meanders, *Theor.Comp.Science* 117 (1993) 227–241, and Meanders, *Selecta Math.Sov.* 11 (1992) 117–144.
- [63] K.H.Ko, L.Smolinsky, A combinatorial matrix in 3-manifold theory, *Pacific.J.Math* 149 (1991) 319–336.
- [64] K.Homan, K.Mehlhorn, P.Rosenstiehl and R.Tarjan, Sorting Jordan sequences in linear time using level-linked search trees, *Information and Control* 68 (1986) 170–184.
- [65] A .Phillips, *The visual mind: Art and mathematics*, p 65, MIT Press (1993); see also <http://www.math.sunysb.edu/~tony/mazes/>.
- [66] L.Chekhov and C .Kristjansen, Hermitian matrix model with plaquette interaction, *Nucl.Phys.B* 479 [FS] (1996) 683–696, [arXiv:hep-th/9605013](#).

- [67] Y .M akeenko, Strings, matrix models, and meanders, Nucl.Phys.Proc.Suppl. 49 (1996) 226-237, arXiv:hep-th/9512211; G .S eneno and R .S zabo, Fermionic matrix models, Int. J. Mod. Phys. A 12 (1997) 2135-2292, arXiv:hep-th/9605140.
- [68] H .T emperley and E .L ieb, Relations between the percolation and coloring problems and other graph-theoretical problems associated with regular planar lattices: Some exact results for the percolation problem , Proc. Roy. Soc. A 322 (1971) 251-280; see also the book by P .M artin, Potts models and related problems in statistical mechanics, World Scientific, Singapore (1991) for a review .
- [69] P .D iFrancesco, Meander determinants, Commun. Math. Phys. 191 (1998) 543-583, arXiv:hep-th/9612026.
- [70] P .D iFrancesco, SU(N) meander determinants, Jour. Math. Phys. 38 (1997) 5905-5943, arXiv:hep-th/9702181.
- [71] J .J acobsen and J .K ondev, Field theory of compact polymers on the square lattice, Nucl. Phys. B 532 [FS], (1998) 635-688, arXiv:cond-mat/9804048.
- [72] D .D eiCont and B .N ienhuis, The packing of two species of polygons on the square lattice, J. Phys. A : Math. Gen. 37 (2004) 3085-3100, arXiv:cond-mat/0311244; Critical exponents for the FPL² model, arXiv:cond-mat/0412018.
- [73] J.L .J acobsen and P .Z inn-Justin, Algebraic Bethe Ansatz for the FPL² model, J. Phys. A : Math. Gen. 37 (2004) 7213-7225, arXiv:math-ph/0402008.
- [74] J.L .J acobsen and J .K ondev, Transition from the compact to the dense phase of two-dimensional polymers, J. Stat. Phys. 96, (1999) 21-48, arXiv:cond-mat/9811085.
- [75] I .J ensen, Enumerations of plane meanders, arXiv:cond-mat/9910313 (1999).
- [76] I .J ensen and A .G uttmann, Critical exponents of plane meanders, J. Phys. A 33 (2000) L187-L192, arXiv:cond-mat/0004321; I .J ensen, A transfer matrix approach to the enumeration of plane meanders, J. Phys. A 33 (2000) 5953-5963, arXiv:cond-mat/0008178.
- [77] O .G olinelli, A Monte-Carlo study of meanders, Eur. Phys. J. B 14 (2000) 145-155, arXiv:cond-mat/9906329.
- [78] see for instance: D .Poulalhon and G .S chaefer, A note on bipartite Eulerian planar maps, <http://www.loria.fr/~schaefer/>
- [79] D .G aunt and M .F isher, Hard-Sphere lattice gases. I. Plane-square lattice, J. Chem . Phys. 43 (1965) 2840-2863.
- [80] L .R unnels, L .C ombs and J .S alvant, Exact finite methods of lattice statistics. II. Honeycomb-lattice gas of hard molecules, J. Chem . Phys. 47 (1967) 4015-4020.
- [81] R .J .B axter, I .G .E nting and S .K .T sang, Hard square lattice gas, J. Stat. Phys. 22 (1980) 465-489.
- [82] R .J .B axter, Hard hexagons: Exact solution, J. Phys. A 13 (1980) L61-L70; R .J .B axter and S .K .T sang, Entropy of hard hexagons, J. Phys. A 13 (1980) 1023-1030; see also [31].

- [83] R. J. Baxter, Planar lattice gases with nearest-neighbour exclusion, *Annals of Combin.* No. 3 (1999) 191–203, [arXiv:cond-mat/9811264](#).
- [84] J. Bouttier, P. Di Francesco and E. Guitter, Critical and tricritical hard objects on bicolourable random lattices: exact solutions, *J. Phys. A* 35:Math. Gen. (2002) 3821–3854, [arXiv:cond-mat/0201213](#).
- [85] G. Schaefer and P. ZinnJustin, On the asymptotic number of plane curves and alternating knots, *Experimental Mathematics* 13 (4) (2005), 483–494, [arXiv:math-ph/0304034](#).
- [86] D. Bisch and V. Jones, Algebras associated to intermediate subfactors, *Inv. Math.* 128 (1997) 89–157.
- [87] W. Lunnon, Multi-dimensional strip folding, *Computer J.* 14 (1971) 75–79.
- [88] P. Chassaing and G. Schaefer, Random planar lattices and integrated superBrownian excursion, *Probability Theory and Related Fields* 128 (2) (2004) 161–212, [arXiv:math.CO/0205226](#).
- [89] B. Duplantier, Random walks and quantum gravity in two dimensions, *Phys. Rev. Lett.* 81 (1998) 5489–5492; Harmonic measure exponents for two-dimensional percolation, *Phys. Rev. Lett.* 82 (1999) 3940–3943, [arXiv:cond-mat/9901008](#).
- [90] G. Lawler, O. Schramm and W. Werner, Values of Brownian intersection exponents I: half-plane exponents, II: Plane exponents, III: two-sided exponents, *Acta Math* 187 (2001) 237–273, 275–308, *Ann. Inst. Henri Poincaré PR* 38 (2002) 109–123, [arXiv:math.PR/9911084](#), 0003156, 0005294.
- [91] J. Bouttier, P. Di Francesco and E. Guitter, Planar maps as labeled mobiles, *Elec. Jour. of Combinatorics* 11 (1) (2004) R 69, [arXiv:math.CO/0405099](#).